

**UNIVERSITÉ DU QUÉBEC**

**THÈSE PRÉSENTÉE À  
L'UNIVERSITÉ DU QUÉBEC À CHICOUTIMI  
COMME EXIGENCE PARTIELLE  
DU DOCTORAT EN INGÉNIERIE**

**PAR  
PING FU**

**MODELLING AND SIMULATION OF THE ICE ACCRETION  
PROCESS ON FIXED OR ROTATING CYLINDRICAL OBJECTS BY  
THE BOUNDARY ELEMENT METHOD**

**MODÉLISATION ET SIMULATION DES ACCRÉTIONS DE GLACE  
ATMOSPHERIQUE SUR DES OBJETS CYLINDRIQUES FIXES ET  
TOURNANTS PAR LA MÉTHODE DES ÉLÉMENTS FINIS DE  
FRONTIÈRE.**

**AOÛT 2004**



### **Mise en garde/Advice**

Afin de rendre accessible au plus grand nombre le résultat des travaux de recherche menés par ses étudiants gradués et dans l'esprit des règles qui régissent le dépôt et la diffusion des mémoires et thèses produits dans cette Institution, **l'Université du Québec à Chicoutimi (UQAC)** est fière de rendre accessible une version complète et gratuite de cette œuvre.

Motivated by a desire to make the results of its graduate students' research accessible to all, and in accordance with the rules governing the acceptance and diffusion of dissertations and theses in this Institution, the **Université du Québec à Chicoutimi (UQAC)** is proud to make a complete version of this work available at no cost to the reader.

L'auteur conserve néanmoins la propriété du droit d'auteur qui protège ce mémoire ou cette thèse. Ni le mémoire ou la thèse ni des extraits substantiels de ceux-ci ne peuvent être imprimés ou autrement reproduits sans son autorisation.

The author retains ownership of the copyright of this dissertation or thesis. Neither the dissertation or thesis, nor substantial extracts from it, may be printed or otherwise reproduced without the author's permission.

# ABSTRACT

The main objective of the thesis proposed herein is to develop a new 2-D ice model which is intended primarily for simulating the ice accretion process on transmission line cables. In an attempt to validate this new model, a number of experimental tests were carried out in the CIGELE icing wind tunnel, and the results obtained from these tests were then compared with those of numerical simulation.

The theoretical work is composed of two phases. In the first phase, the ice accretion process on a fixed cable was modelled, and model parameters, such as the Local Collision Efficiency(LCE) and the local Heat Transfer Coefficient(HTC), were evaluated based on time-dependent airflow and water droplet trajectory computations. For wet accumulations, the movement of a surface water film was tracked for each time step so as to obtain its direction of motion and thickness.

In the second phase, the ice accretion process on a rotating cable was specifically studied as an extension of the newly-developed ice code or model, while both gravitational and aerodynamic torques were considered in the rotation process. The aerodynamic forces were derived by integrating air pressure and air shear along the airflow boundary and were updated according to real-time airflow computations. Subsequently, this new model was applied to analyze two types of overhead transmission line cables under icing conditions, namely, the Bersimis cable and an overhead ground wire, and thereby a number of observations were made.

The conditions applied in the experimental tests in the icing wind tunnel are such that the effects of wind speed, size of test cylinder, air temperature and droplet Median Volume Diameter (MVD) may be revealed by the ice shapes, and that, furthermore, these ice shapes represent the range of the icing process from dry to wet accumulations. In particular, five sets of ice-shapes from both test results and model simulations were illustrated and compared within this thesis so as to validate the proposed ice model. It may be concluded from these comparisons that, in general, the ice shapes predicted by the proposed ice model are in satisfactory agreement with the shapes obtained from experimental tests. Nevertheless, this model tends to underestimate the ice-load to a great extent in the event that the air temperature is high, and the wet regime becomes dominant. In such a case, icicles form beneath the iced objects, and consequently if the weight of the icicles is disregarded, a considerable underestimation of the overall ice-load will occur.

In addition, this thesis examines the effects of Joule heating and water droplet size on the icing process using the new ice model. These effects, however, proved to be difficult to investigate with the experimental set-up currently available. By means of this new model, moreover, it also becomes easy to demonstrate the ice density distribution within the ice-accretion, as discussed in the latter portion of this thesis.

# RÉSUMÉ

L'objectif principal de la thèse proposée est de développer un nouveau modèle numérique en 2D qui est destiné principalement à simuler le processus d'accumulation de la glace atmosphérique sur les câbles de transport de l'énergie électrique. Dans une tentative de valider ce nouveau modèle, un certain nombre d'essais expérimentaux ont été effectués dans la soufflerie réfrigérée de la CIGELE. Les résultats obtenus de ces essais ont été alors comparés avec ceux fournis par notre simulation numérique pour valider le modèle.

Le travail théorique est composé de deux phases. Dans la première, le processus de glaçage sur un câble fixe a été modélisé et les paramètres du modèle, tels l'Efficacité de Collision Locale (LCE) et le Coefficient de Transfert de Chaleur local (HTC), ont été évalués. Cette évaluation est basée sur les résultats du calcul du flux d'air et de la trajectoire des gouttelettes d'eau en fonction du temps. Pour des accumulations en régime humide, le mouvement d'un film d'eau de surface a été suivi pour chaque pas de temps afin d'obtenir sa direction de déplacement et son épaisseur.

Dans la deuxième phase, le processus de glaçage sur un câble tournant a été spécifiquement étudié comme une extension du modèle nouvellement développé. Dans ce cas les moments de torsion dus à la gravitation et aux forces aérodynamiques ont été considérés dans le processus de rotation. Les forces aérodynamiques ont été calculées en intégrant la pression et le cisaillement de l'air le long de la surface de glace. Les calculs sur le flux d'air ont été mis à jour en temps réel. Par la suite, ce nouveau modèle a été appliqué pour analyser deux types de câbles de ligne aériens dans des conditions de givrage, le câble Bersimis et le câble de garde. Ainsi un certain nombre d'observations ont été faites.

Les conditions appliquées dans les essais expérimentaux avec la soufflerie réfrigérée sont telles que les effets de la vitesse du vent, la taille du cylindre d'essai, le Diamètre

Volumique Médian (MVD), et la température de l'air peuvent être révélés par les formes de glace obtenues. Ces conditions appliquées permettent d'obtenir des formes de glace en régime d'accumulation sec, humide ou mixte.

Cinq types de formes de glace obtenues à partir des simulations numériques et des expériences ont été élaborés et comparés dans nos travaux afin de valider le modèle de glace proposé. De ces comparaisons on peut retenir qu'en général, les formes de glace prévues par le modèle d'accumulation proposé correspondent bien avec les formes fournies par les essais expérimentaux. Néanmoins, ce modèle a tendance à sous-estimer la charge de glace surtout dans le cas où la température ambiante devient élevée et le régime humide dominant. Dans un tel cas, en soufflerie des glaçons se forment au-dessous des objets recouverts de glace et par conséquent si leur poids est ignoré dans le modèle numérique, une sous-estimation considérable de la charge de glace arrivera.

Notre étude examine aussi l'impact de l'échauffement par effet Joule ainsi que la taille des gouttelettes d'eau sur le processus d'accumulation de glace en utilisant un nouveau modèle d'accumulation. Ces effets, bien que significatifs, se sont toutefois avérés difficiles à confirmer par le procédé expérimental traditionnel. De plus, à l'aide de ce nouveau modèle, il devient possible de montrer la distribution de la densité de glace dans la masse accumulée.

## ACKNOWLEDGEMENTS

First of all, I would like to extend my sincere appreciations and gratitude to my supervisor, Professor Masoud Farzaneh who is Chairholder of the NSERC/Hydro-Québec/UQAC Chair on Atmospheric Icing of Power Network Equipment (CIGELE), as well as the Canada Research Chair, Tier 1, on the Engineering of Power Network Atmospheric Icing (INGIVRE). He displayed considerable trust and confidence in my research potential, granting me the invaluable chance to pursue my Ph.D. study. During past four years, he gave me a lot of advice and kept me on right track during my thesis work. He also broadened my knowledge in the electrical aspect of the icing research.

I would like to thank the co-supervisor, Professor Gilles Bouchard who guided me and helped me so much. I learned many things from him and he was always very kind to me.

I would also like to thank the researchers and staff at the CIGELE, who had a lot of stimulating discussion with me and offered me technical support and suggestions. These wonderful people include Dr. Jianhui Zhang, Dr. Anatolij Karev, Jean Talbot, Pierre Camirand and Marc André Perron among many others. I would like to extend my thanks to all of my peer students in the CIGELE for the pleasant time spent together. Otherwise, my academic life would have been dull.

I am grateful to Prof. Edward Lozowski, who gave me timely advice in carrying out the research on Local Collision Efficiency, as will be introduced in Chapter 4. I am impressed with his deep insight and innovative ideas.

An acknowledgement is specifically extended to M. L. SinClair, for her patience and painstaking efforts in editing my thesis.

Lastly, my profound gratitude goes to my wife, Nan Yu, for her substantial contribution and sacrifice to our family throughout my Ph.D. study.

## TABLE OF CONTENTS

ABSTRACT.....	i
RÉSUMÉ.....	iii
ACKNOWLEDGEMENTS.....	v
LIST OF SYMBOLS.....	x
LIST OF FIGURES.....	xii
LIST OF TABLES.....	xvi
CHAPTER 1 INTRODUCTION.....	1
1.1 Background .....	2
1.2 The Problem.....	4
1.3 Research Objectives.....	5
1.4 Methodology.....	7
CHAPTER 2 REVIEW OF LITERATURE.....	10
2.1 Introduction.....	10
2.2 Fundamentals of Modelling the Ice Accretion process.....	14
2.3 Analysis of Airflow Dynamics.....	16
2.4 Droplet Trajectory Calculation and Local Collision Efficiency.....	19
2.5 Velocity and Thermal Boundary Layer.....	22
2.6 Thermodynamics of Ice Accretion.....	33
2.7 Surface Temperature of Ice Accretion.....	35
2.8 Ice Volume and Ice Density.....	35
2.9 Conclusions.....	39
CHAPTER 3 AIRFLOW COMPUTATION.....	41
3.1 Introduction.....	41



3.2 Basic Principles.....	43
3.3 Potential Flow.....	44
3.4 Airflow Boundary Layer.....	49
3.5 Feedback Effect in Airflow Calculation due to Boundary Layer Separation ...	55
3.6 Computation of Airflow Past an Object of Arbitrary Cross-Sectional Shape ...	56
3.7 Airflow Field Visualization.....	59
3.8 Conclusions.....	60

## CHAPTER 4 DROPLET TRAJECTORY AND COLLISION

EFFICIENCY.....	61
4.1 Introduction.....	61
4.2 Basic Principles.....	62
4.2.1 Equations Governing the Motion of a Water Droplet.....	62
4.2.2 Solutions.....	66
4.2.3 Initial Conditions and Time Steps.....	66
4.2.4 Surface Collision.....	67
4.2.5 Evaluating Local Collision Efficiency .....	69
4.3 Simulation and Validation of Results.....	71
4.4 Conclusions.....	78

## CHAPTER 5 THERMAL BALANCE AND SURFACE WATER

FLOW.....	79
5.1 Introduction .....	79
5.2 Solution to Thermal Boundary Layer.....	80
5.3 Thermal Balance Equation and Joule Heating.....	84
5.4 Modeling the Flow of a Water Film .....	87
5.5 Water-Film Calculations and Interpretation of Results .....	95
5.6 Conclusions.....	98

CHAPTER 6 EXPERIMENTS AND MODEL VALIDATIONS.....	99
6.1 Experimental Set-up and Instruments.....	99
6.2 Measuring the LWC and MVD .....	105
6.3 Acquiring Ice-Shape Data.....	108
6.4 Comparisons of Ice Shapes from Model Simulation and Experiments.....	108
6.5 Conclusions.....	115
 CHAPTER 7 MODEL SIMULATION.....	 116
7.1 Structure of Ice Model.....	116
7.2 Model Input Parameters.....	118
7.3 Model Output.....	121
7.4 Techniques for Implementing the Proposed Ice Model on a Computer.....	122
7.5 Model Simulations.....	126
7.6 Conclusions.....	140
 CHAPTER 8 SIMULATION OF CABLE ROTATION.....	 142
8.1 Introduction.....	142
8.2 Basic Principles.....	144
8.3 Description of the Calculation Procedure.....	146
8.3.1 Governing Equations.....	146
8.3.2 Evaluating the Centre of Mass.....	148
8.3.3 Position Change of Stagnation Point.....	149
8.3.3 Solution.....	150
8.4 Simulations and Interpretation of Results.....	151
8.5 Conclusions.....	161
 CHAPTER 9 CONCLUSIONS AND RECOMMENDATIONS.....	 163
9.1 Conclusions.....	163
9.2 Recommendations.....	167
9.2.1 Extend the 2-D Ice Model Proposed Herein to 3-D.....	167

9.2.2 Mechanical Analysis of Iced Cable Using the New Ice Model.....	169
REFERENCES.....	170
Appendix: Runge-Kutta Algorithm.....	180

## LIST OF SYMBOLS

SYMBOL	CONCEPT	DIMENSIONS
$A$	Area of a domain under study	$m^2$
$C_d$	Drag coefficient	
$C_f$	Skin-friction coefficient	
$C_p$	Specific heat at constant pressure	$m^2/(s^2 \cdot K)$
$F_b$	Buoyancy force	$N$
$F_d$	Air drag force	$N$
$F_g$	Gravity	$N$
$g$	Acceleration of gravity	$m/s^2$
$G$	Shear modulus	$N/m^2$
$H$	Shape factor	
$h$	Convective heat transfer coefficient	$W/(m^2 \cdot K)$
$I_\rho$	Polar moment of inertia	$m^4$
$k$	Thermal conductivity	$W/(m \cdot K)$
$l$	Coordinate in the surface-attached system	
$N$	Node for surface sectors	
$Nu$	Nusselt number	$hD/k$
$Pr$	Prandtl number	$\nu/\alpha$
$q$	Derivative of the stream function	$m/s$
$Q$	Heat flux	$W/m^2$
$R$	Transverse radius of curvature	$m$
$Re_\theta$	Reynolds number based on the momentum thickness	
$Re$	Reynolds number	
$St$	Stanton number	$h/Gc_p$
$T$	Torque	$N \cdot m$
$T_f$	Torque generated by distributed air shear stress	$N \cdot m$
$T_g$	Torque generated by gravity	$N \cdot m$
$T_p$	Torque generated by distributed air pressure	$N \cdot m$

$U_0$	Onset airflow speed	$m/s$
$U_x$	Free stream velocity at the outer edge of the boundary layer	$m/s$
$V$	Volume or water flow speed	$m^3$ or $m/s$
$V_a$	Free-stream velocity in the vicinity of an icing object	$m/s$
$V_e$	Droplet velocity in the vicinity of an icing object	$m/s$
$W$	Liquid water content	$G/m^3$
$x_a$	Starting point of an adverse gradient	$m$
$x_m$	Position of minimum pressure	$m$
$x_t$	Position where a transitional flow starts	$m$
$\Delta T$	Time step for one simulation	$t$
$(x,y)$	Cartesian coordinates	

### Greek Symbols

$\alpha$	Molecular thermal diffusivity	$m^2/s$
$\beta$	Collection coefficient	
$\gamma$	Water density	
$\Gamma$	Free-stream (potential flow) boundary	
$\delta$	Local impact angle	<i>degree</i>
$\Delta$	Conduction thickness of a thermal boundary layer	$m$
$\Theta$	Boundary layer momentum thickness	$m$
$\lambda$	Dimensionless pressure gradient	
$\mu$	Absolute viscosity	$N.s/m^2$
$\nu$	Kinematic viscosity	$m^2/s$
$\xi$	Homogeneous coordinate varying from $-1$ to $+1$	
$\rho$	Density	$kg/m^3$
$\rho_a$	Air density	$kg/m^3$
$\tau$	Air shear stress	$N/m^2$
$\tau_w$	Wall shear stress	$N/m^2$
$\varphi$	Stream function	$m^2/s$
$\phi$	Trial function for solving residual integral equation	

## LIST OF FIGURES

Figure 1.1	Elementary components of the ice model under discussion .....	9
Figure 2.1	Local icing fraction .....	15
Figure 2.2	Potential flow around a circular object .....	17
Figure 2.3	Definition of LCE .....	20
Figure 2.4	Velocity boundary layer .....	23
Figure 2.5	(a) Flow past a sphere with laminar boundary layer separation. (b) Flow past a sphere with turbulent boundary layer separation.....	26
Figure 2.6	Flow past a sphere with laminar boundary layer separation.....	28
Figure 2.7	Local heat transfer coefficient $Nu/Re^{1/2}$ on a rough circular cylinder at various cylinder Reynolds numbers.....	29
Figure 2.8	Nusselt number for a rough cylinder .....	32
Figure 2.9	Comparison of heat flux terms in typical freezing-rain conditions.....	34
Figure 2.10	Relationship between ice density and Maklin number .....	39
Figure 3.1	Airflow computation and its role in the ice model .....	41
Figure 3.2	The airflow field about an object.....	42
Figure 3.3	Calculation procedure for airflow computation .....	44
Figure 3.4	Input parameters and boundary conditions for BEM calculation .....	48
Figure 3.5	Evolution of angular position for boundary-layer separation points during simulation.....	56
Figure 3.6	Algorithm for surface smoothing .....	57
Figure 3.7	Airflow (a) about a plain object, and (b) about an ice-covered object...	60
Figure 4.1	Forces experienced by droplet .....	64
Figure 4.2	Collision points of water droplets .....	68
Figure 4.3	Definition of the local collision efficiency .....	69
Figure 4.4	Trajectories for water droplets of different diameters.....	71
Figure 4.5	The influence of gravity on the trajectories of water droplets.....	72
Figure 4.6	Comparisons based on both model simulations and test results.....	73

Figure 4.7	Time evolution of the Ice shape and LCE for an icing object.....	74
Figure 4.8	Langmuir volume distribution .....	75
Figure 4.9	Droplet size and volume for bimodal case.....	76
Figure 4.10	Cumulative volume distribution for both cases.....	77
Figure 4.11	LCE distributions for three cases of different DSDs.....	77
Figure 5.1	Comparison of local HTC's obtained from present simulation and those of earlier studies .....	83
Figure 5.2	Magnitude analysis for heat fluxes in the heat balance equation .....	87
Figure 5.3	Diagram for water-flow direction .....	88
Figure 5.4	Diagram of the mechanical analysis of a water film.....	89
Figure 5.5	Diagram for the mass conservation of a water film .....	90
Figure 5.6	Inclined flow between a fixed plate and moving plate .....	91
Figure 5.7	Diagram of the division of surface zones .....	93
Figure 5.8	Water-film thickness and speed on the surface of a cylinder .....	98
Figure 6.1	A top view of the CIGELE icing research wind tunnel .....	101
Figure 6.2	Test section of the CAIRWT .....	101
Figure 6.3	Relationship between air and fan speed .....	102
Figure 6.4	Spray bar fitted with three nozzles .....	103
Figure 6.5	Control panel for air and water pressures and water flow rate .....	103
Figure 6.6	( a ) Collargol coated slide ( b ) Traces of water droplets under a microscope.....	105
Figure 6.7	Relationship between MVD and air speed under experimental conditions .....	107
Figure 6.8	Relationship between LWC and air speed under experimental conditions.....	107
Figure 6.9	( a ) An iced cylinder ( b ) Cross-sectional ice shape at midpoint of same cylinder.....	108
Figure 6.10	Comparison of ice shape (Air Speed 5 m/s, Air Temperature -15°C, MVD 34 $\mu$ m, Diameter 19.05 cm) .....	110
Figure 6.11	Comparison of ice shape (Air Speed 5 m/s, Air Temperature -15°C, MVD 35 $\mu$ m, Diameter 34.9 cm).....	110

Figure 6.12	Comparison of ice shapes (Air Speed 5 m/s, Air Temperature -10°C, MVD 28 $\mu\text{m}$ , Diameter 34.9 cm).....	113
Figure 6.13	Comparison of ice shapes (Air Speed 5 m/s, Air Temperature -5°C, MVD 26 $\mu\text{m}$ , Diameter 34.9 cm).....	114
Figure 6.14	Comparison of ice shapes (Air Speed 5 m/s, Air Temperature -5°C, MVD 33 $\mu\text{m}$ , Diameter 19.05 cm).....	115
Figure 7.1	General structure of the proposed ice model.....	118
Figure 7.2	Parameter input interfaces in ice code .....	120
Figure 7.3	Visual display for ice accretion processes .....	121
Figure 7.4	Conceptual representation of the ice code under discussion .....	122
Figure 7.5	Hierarchical diagram for classes of ice code .....	125
Figure 7.6	Comparison of ice accretion shapes predicted by classical and new methods (time step: 5min) .....	127
Figure 7.7	Time evolution of ice load predicted by both methods.....	128
Figure 7.8	Comparison of ice shapes with and without current for a dry accumulation.....	130
Figure 7.9	Comparison of ice shapes with and without current for a semi-wet accumulation.....	131
Figure 7.10	Comparison of ice shapes with and without current for a wet accumulation .....	132
Figure 7.11	Local Collision Efficiency for cylinders of different diameters.....	133
Figure 7.12	Ice Shapes for cables of different diameters.....	134
Figure 7.13	Ice-density distribution .....	136
Figure 7.14	Ice accretion for droplets of 500 $\mu\text{m}$ in diameter .....	139
Figure 7.15	Ice accretion for droplets of 100 $\mu\text{m}$ in diameter.....	139
Figure 7.16	Ice accretion for droplets of 50 $\mu\text{m}$ in diameter .....	140
Figure 7.17	Time evolution of ice mass.....	140
Figure 8.1	One section of cable between two towers.....	145
Figure 8.2	Forces experienced by an iced cable .....	145
Figure 8.3	Schematic diagram of forces experienced by a rotated cable .....	146



Figure 8.4	Parameters for an arbitrary element of ice deposit .....	148
Figure 8.5	Position change of stagnation point as ice accumulates.....	150
Figure 8.6	Comparison between ice shapes obtained from experimental and theoretical studies .....	153
Figure 8.7	Time evolution of external and internal torque.....	156
Figure 8.8	Time evolution of cable rotation angle.....	157
Figure 8.9	Time evolution of weight center angle.....	157
Figure 8.10	Time evolution of ice mass .....	158
Figure 8.11	Time evolution of ice deposit .....	159
Figure 8.12	Torque-angle curves for wire sample.....	161
Figure 9.1	Icicle curtain beneath an iced cylinder .....	168

## LIST OF TABLES

Table 5.1	Parameters C1 and C2 as functions of the Reynolds number.....	82
Table 5.2	Formulae corresponding to surface zones.....	94
Table 6.1	Experimental parameters .....	104
Table 6.2	Parameters used for model validations .....	109
Table 7.1	Model input parameters.....	119
Table 7.2	Model parameters for comparisons between classical and new LCE- solving methods.....	126
Table 7.3	Model Parameters for simulating Joule effects under three distinct icing conditions.....	129
Table 7.4	Model parameters for predicting ice density distributions under three distinct icing conditions.....	135
Table 7.5	Model parameters for investigating the influence of droplet size.....	138
Table 8.1	Conditions for experimental test and model simulation of cable rotation.....	151
Table 8.2	Simulation conditions for both rigid and soft cables.....	154
Table 8.3	Predicted ice shapes for both rigid and soft cables .....	155
Table 8.4	Model parameters for reconstructing natural icing process .....	160

# **CHAPTER 1**

## **INTRODUCTION**

Atmospheric icing occurs when freezing raindrops, snow particles or supercooled cloud droplets come into contact with exposed surfaces. It is a serious and costly natural phenomenon which affects the operation of such services as electric power transmission and distribution, telecommunications, and so forth. Annually, a considerably large number of structural failures due to ice accumulation has been reported in several countries including Canada, the United States, Japan, England, and China among others. Approximately 140 tower-collapses as a result of ice accumulation have been reported and confirmed since 1959 in the United States alone (Mulherin, 1996).

Icing problems may be classified into two types in terms of the meteorological conditions that produce the ice formation, namely, precipitation icing and in-cloud icing. Precipitation icing is the most common icing mechanism, and it can occur in any geographical area subject to freezing rain or drizzle. The difference between the freezing rain and drizzle is purely one of drop size rather than intensity of precipitation. Usually, drizzle comes from sheets of low shallow cloud, whereas rain is more likely from deeper clouds (Poots, 1996). The frozen deposit due to precipitation icing usually appears as a clear type of glaze, and does not usually last longer than a day or two.

The second type of problem involves in-cloud icing. This type of icing condition is caused by the impingement of supercooled water droplets in a cloud on an exposed object. The ice formed under such conditions is mostly rime, and this process tends to occur in mountainous areas where clouds exist above the freezing level or in a supercooled fog at lower elevations as produced by a stable air mass with a strong temperature inversion (Lock, 1990). Such conditions can last for days or even weeks at a time.

In general, ice may be classified into three basic types, namely, glaze, hard rime and soft rime (Farzaneh et al., 1992). Glaze is transparent and has a density of about  $0.9 \text{ g/cm}^3$ . Hard rime is opaque and has a density of between  $0.6$  and  $0.87 \text{ g/cm}^3$ . Soft rime is white and opaque, with a density of less than  $0.6 \text{ g/cm}^3$ . The type of ice formed is determined by combinations of air temperature, wind speed, drop size, and liquid water content or rainfall intensity. A detailed description will be provided in the review of the literature.

## ***1.1 Background***

Under icing conditions, airborne icing particles come to impinge on and then adhere to a given conductor upon which ice will grow. An ice-covered object exposed to the wind undergoes an increase in both static and dynamic loads, the distribution of which varies mainly according to the shape of the ice accretion.

The potential for damage incurred to transmission facilities as a result of the icing phenomenon is considerable. Ice accumulation causes transmission-line oscillations to damp slowly, while in the mean time causing an increase in amplitude of these oscillations due to the non-uniform distribution of aerodynamic and gravitational loads. It is believed that the galloping, large-amplitude oscillation of ice-covered cables at low frequencies is responsible for around 1/3 of electric-line maintenance and operating costs (Ilinca et al. 1996). An asymmetrical accumulation also leads to the twisting of conductors and cables as well as to an acceleration in its degree of fatigue leading to the possibility of rupture. In extreme cases, excessive accumulations may cause serious structural failures to overhead power lines, towers, and other related equipment.

Among the numerous power system failures caused by icing of transmission lines, the one which occurred in southern Quebec and eastern Ontario in January of 1998 was exceptionally disruptive in terms of both its duration and the scale of the ensuing damage (Farzaneh, 2000). According to Statistics Canada (Lecomte et al., 1998), during this ice storm close to 1.4 million people in Quebec and 230,000 in Ontario were subjected to major power outages for over one week due to the fact that more than 1,000 power transmission towers and 30,000 wooden utility poles were destroyed by excessive ice-loads. After assessment of this tragedy, it became increasingly clear to industrial and public concerns that there had been a significant underestimation of the ice-load effect during the design of transmission lines for use under icing conditions.

The methods commonly used by researchers in order to investigate the icing process are summarized as follows:

1. Mathematical modelling,
2. Experimental simulation,
3. Statistical analysis based on data from on-site observations.

Of these three methods, it is clear that the study based on data observed on-site is the most reliable for design engineers. However, a complete set of observational data is not always available, since the setting up of the required system is too time-consuming and not cost-effective. Experimental simulation is a viable way of studying ice accretion since the test conditions may be controlled to a certain extent. The experimental results, however, are hardly comparable to observations made under natural conditions as they tend to vary over time. Mathematical/theoretical modeling is of great value when combined with experimental validation because of its efficiency and economy.

## ***1.2 The Problem***

A satisfactory ice model for use in establishing the critical ice load on transmission lines under icing conditions is not yet readily available, even though extensive studies on icing phenomena have been carried out to date by researchers in the domain. The reason for this lack is due to the fact that scientists have always been motivated by a research interest in the icing phenomenon alone as simulating this process requires a combination of multi-disciplinary fields of abstract knowledge. Practical applications of such an ice model, however, are not adequately addressed. Also, the study in itself leaves much to be

desired from the point of view of ice-model development. Newly-developed technology and calculation methods emerging from related domains make it possible and necessary to develop a new ice model capable of better satisfying the needs of the user in terms of its performance and accessibility. Hence there is a genuine need for carrying the relevant research even further.

As pointed out by Makkonen et al. (1984), there are several factors which hamper research and investigation into the ice accretion process.

- The complexity of the ice phenomenon itself: The icing of an object involves several feedback mechanisms and non-linear relationships between the icing rate and the various factors affecting it.

- The difficulty in assessing the relevant input parameters: Adequate ice-modelling requires such input parameters as the liquid water content and droplet size distribution of the fog or cloud. There are considerable technical problems involved in measuring these quantities accurately, even under laboratory conditions.

- The lack of experimental data: Precise quantitative verification of theoretical ice models has been virtually impossible to date, because of the above-mentioned difficulty in measuring the input parameters. These input parameters are highly interrelated in the natural environment. There are also practical problems involved in measuring the icing rate.

### ***1.3 Research Objectives***

The main objectives of this research are the following:

1. To develop a time-dependent 2D numerical ice model for simulating the ice accretion process on a fixed cylindrical object.
2. To model and simulate the ice accretion process on a rotating cable as an extension of the above-mentioned ice model.
3. To confirm the validity of the ice model by using experimental data obtained from tests in the CIGELE icing wind tunnel.

The modelling of the ice accretion process may contribute to acquiring a greater in-depth understanding of this particular phenomenon, and to provide the relevant data for developing a feasible de-icing solution. From the model simulation, it is possible to obtain the ice shape, ice-load, and density distribution among others.

The theoretical work consists of two phases. In the first phase, the ice accretion process on a fixed cable is modelled and simulated, while such model parameters as the Local Collision Efficiency (LCE) and the local Heat Transfer Coefficient (HTC) are evaluated on the basis of time-dependent airflow and water droplet trajectory computations. In the second phase, the ice accretion process on a rotating cable is studied specifically as an extension of the newly-developed ice code or model, taking into account the effects of wind and ice load.

The ultimate goal of this project is to develop an ice model intended for practical operational use, capable of supplying the ice-load information for transmission line design.



## ***1.4 Methodology***

This research project will be carried out in such a way that the theoretical modelling is followed by the experimental investigation which will produce data for validating the preceding modeling procedure. The mathematical model presented herein consists of a number of elementary components, as shown in Figure 1.1.

In particular, airflow field is solved according to the boundary layer theory, i.e. potential flow combined with flow boundary layer. The potential flow region under study is considered to be the superposition of a uniform flow and a disturbance flow which may be solved using the Boundary Element Method (BEM). The fluid boundary layer can be evaluated in terms of the velocity distribution on the common boundary as obtained from the preceding potential flow calculation.

The motion of water droplets was modeled on the basis of the balance between aerodynamic force, gravity, and buoyancy force. The Runge-Kutta numerical algorithm was applied in solving the differential equations of motion so as to obtain droplet trajectories. The local impingement efficiency was evaluated according to its original definition (McComber, 1981).

In modelling cable rotation under icing conditions, both gravitational and aerodynamic forces were taken into consideration. The values for the latter forces were derived from

the integration of air pressure and shear stress along the flow boundary, and were constantly updated according to real-time airflow computations.

In view of the extensive amount of coding work involved in this project, the Object Oriented Programming technique (OOP) was used to organize the entire project, since this technique makes it possible to maintain the ice code with relative ease.

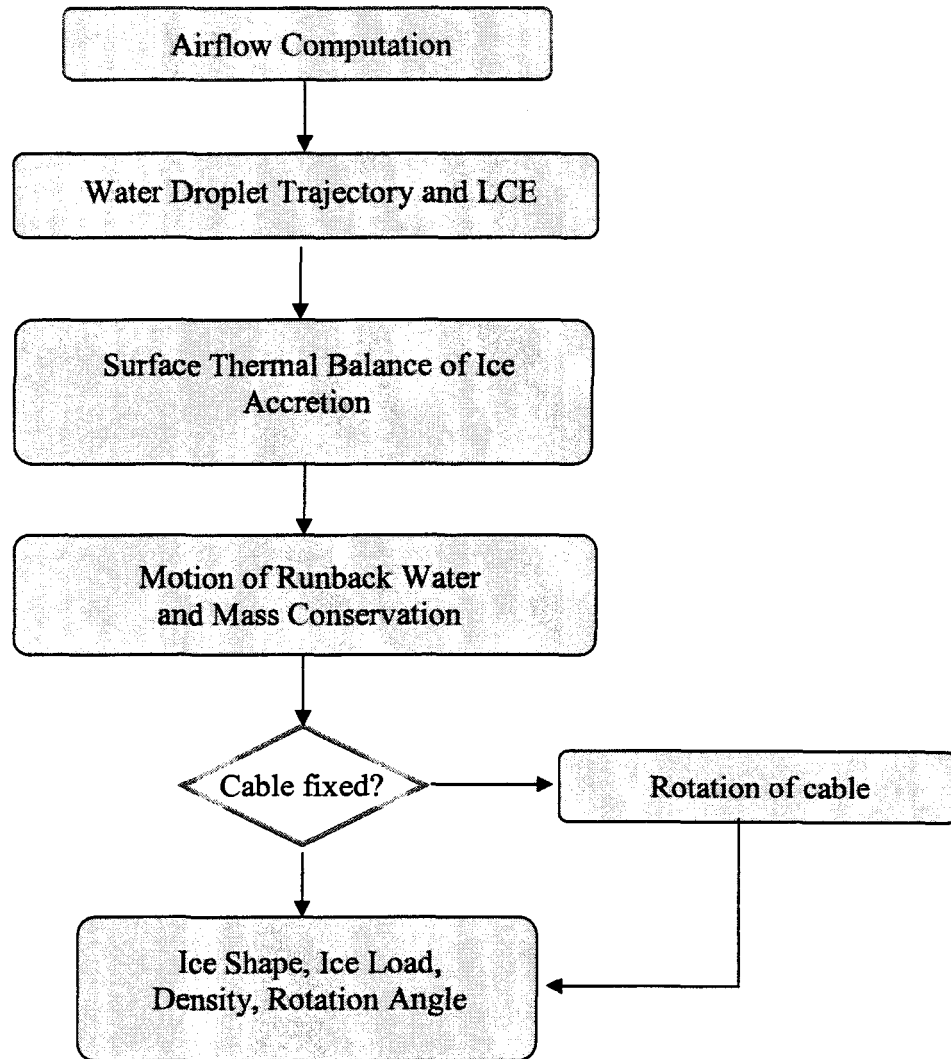


Figure 1.1 Elementary components of the ice model under discussion

## **CHAPTER 2**

### **REVIEW OF LITERATURE**

#### ***2.1 Introduction***

Nowadays, a wide variety of publications on the icing phenomenon may be found in the literature, and certain studies may even date as far back as the 1940s. Since then, the phenomenon has been subjected to extensive investigation prompted by the requirements of engineering practices in a number of northern countries, including Britain, Canada, Czech Republic, Finland, France, Germany, Hungary, Iceland, Japan, Norway, Russia, Switzerland, and the United States. These studies were made with the aim of compiling ice-load and wind-on-ice load databases in order to understand the various complex forms of wet-snow and ice accretion, to develop and to confirm the validity of icing models, and to introduce probabilistic design load approaches (Poots, 1996).

A number of the existing ice models concentrated on the global ice-load prediction alone, as in Jones's model (1996) and Makkonen's model (1984), while others focused on ice shape prediction so as to estimate the dynamic wind-on-ice loads together with static ice loads. More importance was assigned to the ice shape prediction, since it is easy to estimate the ice-load from the predicted ice shape simply by integrating the product of ice density and the area of any element over ice accretion. Also, knowing the ice shape makes it possible to investigate the dynamic force exerted on iced objects and in the case of cable icing, it is possible to obtain the overall loads sustained by its supports by means

of carrying out integration along its span. It should be pointed out that an irregular ice shape always aggravates the situation of the transmission line under icing conditions.

The complex nature of the icing process dictates that the quest for further understanding its mechanism requires a multi-disciplinary approach. Evaluating such parameters as airflow field and water droplet trajectories from a time-dependent perspective is extremely time-consuming and requires access to vast computational resources.

At an earlier stage of the research process, powerful computation tools were not so easily available as they are today, and apparently this lack hampered the advancement of studies on ice models. To date, ice model studies appear to have experienced three stages of development, based on the increasing accessibility of computational tools, whether in the form of hardware or software.

### **Stage 1: Enrichment and Collation of Basic Knowledge**

By the 1970s, a number of researchers had already carried out numerous fundamental studies either theoretically or experimentally. Langmuir and Blodgett (1946) successfully completed trajectory calculations for droplets passing in the vicinity of a circular cylinder. In his study on a circular cylinder, Ludlam (1951) took into account two different ice accretion regimes, namely, the dry regime and the wet regime, and he found that the type of regime is closely related to the water content of the non-perturbed flow at a given temperature and speed. Fraser, Rush and Baxter (1952) discovered that, under

certain conditions, not all of the impinging water is removed, and that part of the water remains in the pockets of the ice matrix resulting in the formation of spongy ice.

Messinger (1954) and List (1963) developed a heat-balance equation based on energy conservation, in particular for a circular cylinder. This equation is formulated on the basis of the assumption that ice accretion is a process of thermal equilibrium, and thus the sum of all heat transfer terms should be zero.

Contemporaneously, several researchers, including Langmuir & Blodgett (1946); Imai (1953); and Chainé and Castonguay (1974) among others, attempted to create a formula to represent the direct relationship between the prevailing climatic conditions and ice accretion. However, their endeavours met with partial success only.

These above-mentioned fundamental studies have had a profound influence on present-day numerical modelling. For example, the heat balance equation mentioned above is still widely used in modern numerical icing models, though with certain slight modifications. As another example, the curve-fitting functions obtained from the theoretical work of Langmuir and Blodgett (1946) is still used to evaluate the Local Collision Efficiency (LCE) in Lozowski's model (1983).

## **Stage 2: Earlier Attempts at Modelling the Ice Accretion Process on Computers**

In the 1980s, researchers began to write computer programs which would carry out model simulations, and these computer models made it possible to obtain data for

generating ice shapes under a wide range of simulation conditions. Before that time, such ice shapes for the purposes of research could only be obtained from experimental tests. However, the performance of these programs was comparatively limited and the results of simulation relied mainly on the individual interpretation of the researcher. Makkonen (1984) put forward a model based on boundary-layer theory for predicting the local heat transfer coefficient around a cylinder, taking into consideration the effect of roughness characteristics. Lozowski et al. (1983) presented a model which was designed to simulate in-flight ice accretion processes on an unheated, non-rotating cylinder where both rime and glaze can be accounted for. The model computes the thermodynamic conditions and the initial icing rate as a function of the angle around the upstream face of the cylinder using the classical Messinger equation.

### **Stage 3: Development of Time-Dependent and All-Inclusive Numerical Ice Models**

Nowadays, the computer is not only an indispensable calculating tool for researchers but it is also a communication interface between the theoretical model and its users. Newly-developed numerical ice models tend to be more complete and inclusive, and hence more complex. Certain time-consuming elements, such as the dynamic airflow computation and water droplet trajectory calculation, were incorporated in the model codes. Accordingly, the other parameters are constantly updated in response to the changes in ice geometry and they include such parameters as the local Heat Transfer Coefficient (HTC) which is essential in determining the ice shape of wet accretions. Meanwhile, the models themselves were upgraded from 2D to 3D. These new developments were more often to be found in studies on airfoil icing such as the

LEWICE model at the icing branch of NASA as described by Wright (1995), the one from ONERA as described by Gent (1990) and by Hedde (1992), and the CANICE model described by Paraschivoiu (1994). This research was so productive and successful that these models became applicable in the investigation of ice shapes under a variety of icing conditions, thereby producing model predictions displaying acceptable accuracy, although no model to date is capable of encompassing all cases without exception.

The ice codes or models themselves have also been made more easily accessible to the average layman. User-friendly graphical interfaces and vivid visualizations developed specifically for these models facilitate the understanding of the complex mechanism of ice accretion and draw the attention of relevant industrial concerns to the need for obviating the potential for damage caused by the icing phenomenon.

## ***2.2 Fundamentals of Modelling the Ice Accretion Process***

Icing intensity,  $I$ , may be determined theoretically from the equation formulated by Makkonen and Stallabrass (1984):

$$I = \frac{2}{\pi} EnUW \quad (\text{E 2-1})$$

where  $E$  denotes the collection coefficient. Under dry icing conditions, if the bouncing effect is disregarded,  $E$  may be replaced by the collision efficiency  $\beta$ .

$U$  and  $W$  denote the air speed and liquid water content, respectively, and

$n$  denotes the icing fraction of the overall collected water.



The surface of an ice-covered object may be discretized into a large number of elements in order to determine the shape of the ice accretion over time, then the above equation may be applied to each of these element. For any specific element, the water is collected partly from impinging water, and partly from the unfrozen runback water of its adjacent element as shown in Figure 2.1, in which the water film is assumed to flow from  $i-1$  to  $i$ , although there is a possibility that water might also flow from  $i$  to  $i-1$ . This flow direction is determined by the effects of air drag and gravity.

For each element, the mass conservation may be expressed as:

$$I^i = (M_r^i + M_i^i)n^i \quad (\text{E 2-2})$$

where  $M_i^i = E^i U W$  and  $M_r^i = E^{i-1} (1 - n^{i-1}) U W$

in which  $I^i$  is the local icing intensity at element  $i$ ;

$n^i$  the local icing fraction at element  $i$ ;

$E^i$  is local collection coefficient from the droplet trajectory calculation.

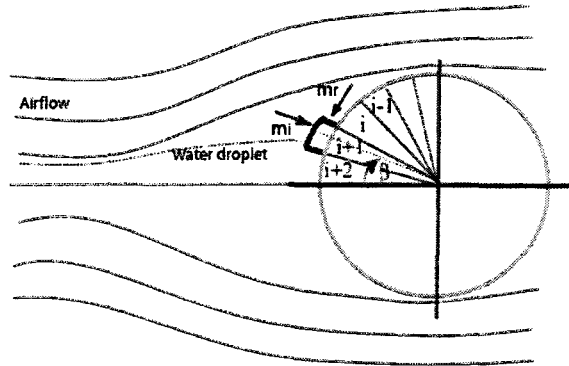


Figure 2.1 Local icing fraction

It should be noted that local airflow velocity does not appear in Eq. 2-1. The terms of the LCE and local icing fraction, however, are closely associated with the airflow velocity distribution, details of which will be discussed in the following section.

### ***2.3 Analysis of Airflow Dynamics***

A key problem in investigating the icing phenomenon on cylinders is obtaining accurate flow calculations for complex geometry and high Reynolds numbers, as is typical of many icing situations. The airflow across an iced body is compressible and viscous, a complete solution for which, however, poses considerable mathematical difficulty for all but the most simple flow boundary geometry.

So far, numerous studies have been carried out to find a solution to the governing differential equations for such a flow numerically, however, limited success has hitherto been obtained using such a procedure which has hitherto proved to be overly time-consuming from a computational viewpoint, as pointed out by Bazeos and Beskos (1990).

In most classical icing models, airflow computation was sidestepped due to the difficulties described above; instead, a number of simplified calculation procedures, such as those of Makkonen (1984) and McComber (1984), were applied. In Makkonen's procedure, the airflow was taken as a constant free stream and the change in ice accretion shape was disregarded. The theoretical formulae used to represent the airflow about a circular object are as follows:

$$U = -1 - (Y \times Y - X \times X) / (X \times X + Y \times Y)^2 \quad (\text{E 2-3})$$

$$V = 2 \times X \times Y / (X \times X + Y \times Y)^2 \quad (\text{E 2-4})$$

where the dimensionless coordinates  $X$  and  $Y$  are defined by  $X=x/D$  and  $Y=y/D$ , where  $D$  is the diameter of the object. The velocity components for any node in the field may be obtained from the following equations:

$$u_x = U \times U0; \quad (\text{E 2-5})$$

$$u_y = V \times U0; \quad (\text{E 2-6})$$

where  $U0$  is the onset free-stream speed.

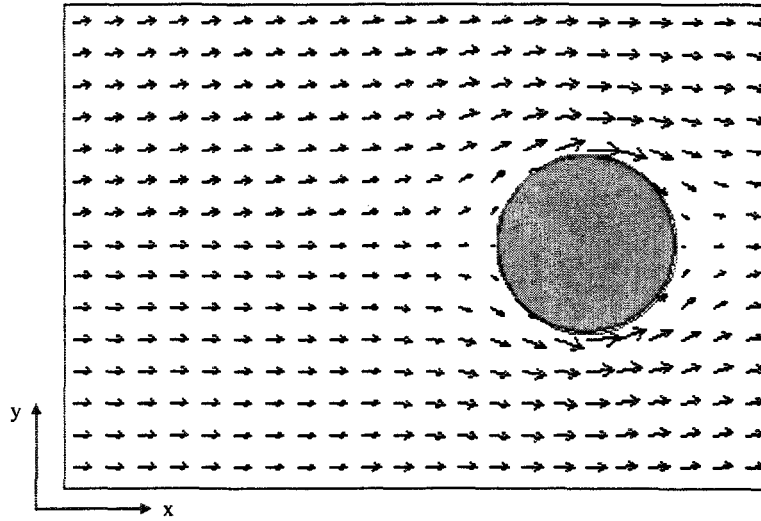


Figure 2.2 Potential flow around a circular object

More recently, ice model developers have begun to incorporate the airflow computation into their models so as to obtain the velocity distribution. The airflow in their models was still taken as a free stream or potential flow, while the elements of turbulence and rotation were usually disregarded. The computation process, however, is made time-dependent to account for the variation in ice accretion shape. The flow solver

used in the LEWICE code (1995) developed at Douglas, for instance, is a two-dimensional potential flow code capable of handling up to 10 separate bodies and up to 105 panels in its modified form (Hess & Smith, 1975). According to them, the use of a potential flow code is desirable due to its speed of execution and its ability to calculate a flow field around the irregular geometry of the ice shapes produced during ice accretion. The Douglas Hess-Smith code produces a flow solution by using a distribution of sources, sinks, and/or vortices along the object geometry. In calculating the flow field, contributions from all the sources, sinks, and/or vortices are summed up. The body surface itself is represented by several straight line segments called panels.

Bazeos & Beskos (1990) pointed out that the evaluation of potential flow by the Boundary Element Method (BEM) is superior to that obtained using the Panel Method or indirect BEM, since the physical properties of flow deal with potential and flux, rather than sources and vortex density.

Lesnic et al. (1995) introduced a practical approach to modelling the flow past a body with an arbitrary cross-sectional shape. The airflow field was treated as a potential flow within the separation model and the object immersed in the fluid can be an obstacle with an arbitrary cross-sectional shape. A tangential detachment of the flow at the edges of the obstacle was assumed, and hence the infinite behaviour of the velocity at these positions is removed.

## ***2.4 Droplet Trajectory Calculation and Local Collision Efficiency***

The Local Collision Efficiency (LCE) is a key parameter for ice accretion simulation, since it describes the distribution of droplet impingement on the surface of an object. In order to evaluate the LCE according to its original definition, it is necessary to obtain the trajectories for hundreds of droplets, which further demands a thorough and all-inclusive solution to the airflow field. Performing both these computations, however, requires a painstaking approach to the task.

Seminal work by Taylor (1940), and Langmuir & Blodgett (1945), has laid the foundations for studying the impact of cloud droplets on structures and, in more recent years, for developing the theory of the inertial deposition of aerosols on objects. Consider a stream of particles moving in a horizontal direction toward a circular cylinder placed perpendicular to the direction of the airflow. The particles far upstream are assumed to be moving at the free stream velocity. On approaching the cylinder, a particle undergoes a deflecting force due to the diverging streamlines, and a resistance originating in its own inertia. Thus the particle motion relative to the airflow decreases and the particle may fail to reach the cylinder surface before it is swept away by the airflow. The collision efficiency of the cylinder,  $E$ , is defined as the ratio of the mass flux of impinging particles on the upstream side of the cylinder, to the mass flux that would be experienced by the surface if the particles had not been deflected by the air stream. An identical definition may be derived from the work of Taylor (1940), and Langmuir & Blodgett (1945), as follows:

$$E = \frac{\text{Number of particles arriving on the object by impact}}{\text{Number of particles geometrically incident on the object}} \quad (\text{E } 2-7)$$

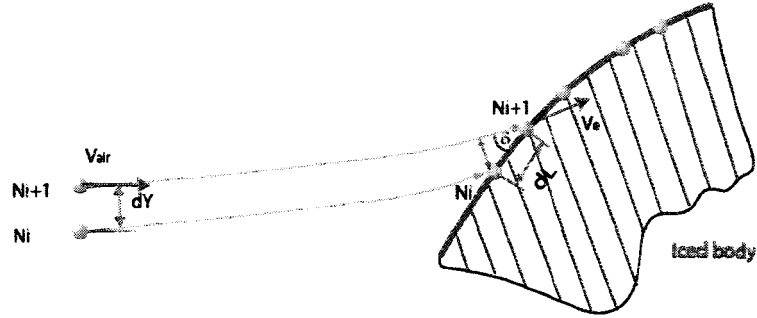


Figure 2.3 Definition of LCE

The Local Collision Efficiency (LCE) may be formulated as follows:

$$\beta(\theta) = \frac{dY}{dL} \quad (\text{E } 2-8)$$

where  $dY$  is the vertical distance between two trajectories in the onset flow,

and  $dL$  is the distance between the impact points on the object surface.

The alternative to Eq. 2-8, however, is easier to apply in model calculations, and it is a function of the local impact speed,  $V_e$ , and angle,  $\delta$ , as shown in Fig. 2.3. It may be formulated as follows:

$$\beta(\theta) = \frac{\frac{\vec{V}_e \cdot \vec{l}}{|\vec{l}|}}{V_{air}} = \frac{|V_e| \times \cos(\frac{\pi}{2} - \delta)}{V_{air}} \quad (\text{E } 2-9)$$

It should not be hard to prove that both of the above equations are numerically identical when the liquid phase is assumed to be a continuum.

In the past, many ice model researchers preferred to use empirical approximations to obtain the Local Collision Efficiency directly in order to avoid the complexity of field computations. Gates et al. (1984) reported two approximate methods commonly used by those who attempted to develop ice models. One approach, used by Ackley and Templeton (1978), and by Makkonen (1984), assumes that the accretion retains a known simple shape as it grows, in this case, roughly circular. The impingement coefficient can thus be readily obtained by a function of dimensionless parameters using tabular interpolation, or by fitting the curves plotted according to pre-computed values. An alternative approach, formulated by Lozowski et al. (1979, 1983), assumes that the first thin accreted layer represents a small perturbation in the shape of the accreting body, thereby causing the airflow, droplet trajectories, and local collision efficiency to experience small perturbations. This layer should be addressed by applying perturbation methods to the dynamic equation for gaseous and liquid phases. In this approach, a heuristic argument is used to estimate the perturbations.

For wire icing, Makkonen (1984) proposed an empirical correction to the total collection efficiency. The collection efficiency,  $E_m$ , based on the Median Volume Diameter (MVD) of the droplet size distribution may thus be determined. The calculation is again based on the Langmuir & Blodgett method for the dimensionless equation of motion for a droplet in an airflow.

Jones (1996), however, attempted to integrate, and thus numerically solve, the differential equation for water droplet trajectory developed by Lozowski (1983), taking

into account both gravitational force and air drag on freezing drizzle or precipitation-sized droplets, as follows:.

$$\frac{d\vec{v}}{dt} = -3 \left[ \frac{C_D P_a}{4d\rho_0} \right] \left| \vec{v} - \vec{V} \right| \left( \vec{v} - \vec{V} \right) + \vec{g} \quad (\text{E 2-10})$$

where  $\vec{v}$  is the droplet velocity,  $\vec{V}$  is the wind velocity,  $C_D$  is the drag coefficient of the droplets,  $d$  is the droplet diameter, and  $\vec{g}$  is the acceleration of gravity. In the absence of a solution to this equation for rain and drizzle-sized droplets, Jones assumed that the droplets fall at their terminal velocity and move horizontally at the wind speed.

It should be noted that Eq. 2-10 is impossible to solve unless the nodal-wise airflow vector,  $\vec{V}$ , is available, therefore airflow computation is a prerequisite for water droplet trajectory calculation.

## ***2.5 Velocity and Thermal Boundary Layer***

- Velocity Boundary Layer

A major practical breakthrough with regard to viscous fluid computation was made when, according to Kays & Crawford (1993), Brandt discovered that the influence of viscosity is confined to an extremely thin region very close to the object under investigation, and that the remainder of the flow field can be treated approximately as



nonviscous, that is, it may be calculated by applying the methods of potential flow theory described earlier in this chapter.

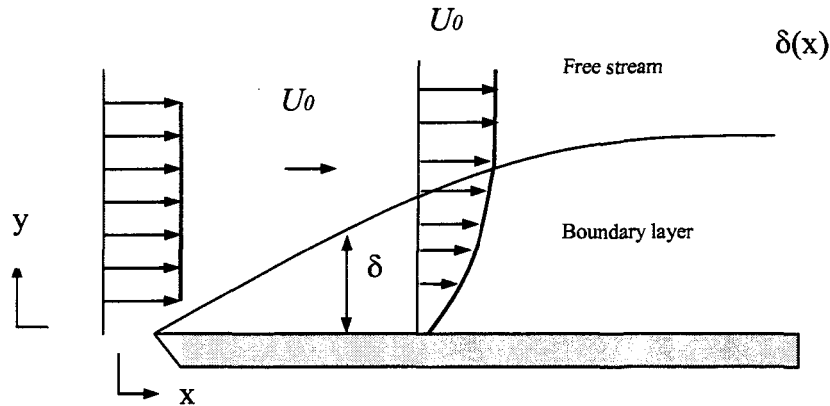


Figure 2.4 Velocity boundary layer

The thin region near the body surface, which is known as the boundary layer, lends itself to relatively simple analysis by the very fact of its thinness in relation to the dimensions of the body. A fundamental assumption of the boundary-layer approximation is that the fluid immediately adjacent to the body surface is at rest relative to the body, an assumption that appears to be valid except for very low-pressure gases when the mean free path of the gas molecules is large compared to the body. Thus the hydrodynamic or momentum boundary layer may be defined as the region in which the fluid velocity changes from its free-stream value to zero at the body surface, as shown in Figure 2.4. In reality, no precise “thickness” with regard to the boundary layer has yet been defined, although boundary-layer thickness may be considered as the distance in which most of the velocity change takes place.

So far, only a few exact solutions to the equations of motion for boundary layers are known, and these are mainly for laminar flow. When the calculation procedure becomes overly tedious and time-consuming, it is often worthwhile to search for an approximate approach, such as integral methods. The integral equations of the boundary layer provide the basis for a number of approximate procedures, but are, in themselves, exact at least within the boundary-layer approximation. The very nature of the integral solutions arises from the manner in which they are generally employed.

- Thermal Boundary Layer

Just as a velocity boundary layer develops when there is fluid flow over a surface, a thermal boundary layer develops concurrently, if the fluid free stream and surface temperature differ. The region of the fluid in which these temperature gradients exist is the thermal boundary layer, and its thickness,  $\delta_t$ , is typically defined as the value of  $y$  for which the ratio  $\left[ \frac{(T_s - T)}{(T_s - T_\infty)} \right] = 0.99$ . With increasing distance from the leading edge, the effects of heat transfer penetrate further into the free stream and the thermal boundary layer grows.

A number of integral equations may be applied in evaluating the Nusselt number for the laminar boundary layer, the turbulent boundary layer, if any, and the wake section. The free-stream velocity above the boundary layer may be determined by solving the equations of the airflow boundary layer as described in Chapter 3, and the input parameters may then be used for the thermal calculation of the boundary layer.

Once the local Nusselt number is known, the local HTC,  $h$ , may be obtained according to the following formula:

$$h = \frac{Nu \cdot K_f}{L} \quad (\text{E 2-11})$$

where,  $K_f$  is the thermal conductivity of the fluid, and  $L$  is a characteristic dimension of the model under consideration.

### **2.5.1 Effect of Reynolds Number and Roughness on the Velocity Boundary Layer**

Roughness or imperfections of the surface tend to provoke early transition, as does also a high degree of turbulence in the free stream outside the boundary layer. A most important factor, however, is the Reynolds number. If this number is measured in terms of the distance along the surface, then for values less than about  $10^5$ , the laminar boundary layer is very stable and it is difficult to provoke transition. However, with an increase of the Reynolds number, the stability of the laminar boundary layer decreases, and transition is more and more easily provoked. With a Reynolds number, in terms of distance along the surface, greater than about  $2 \times 10^6$ , considerable care must be taken in keeping the surface smooth while at the same time eliminating external disturbances so as to avoid an early transition. Surface roughness has a potential for hastening the transition of the boundary layer as mentioned above. The small roughness elements tend to behave like bluff bodies and eddies are cast off them which then disturb the laminar boundary layer and induce transition to turbulent flow and in consequence the drag usually increases. Eddies are likewise cast off the roughness elements when the boundary layer is turbulent and then they directly increase the local drag. The larger the roughness elements, the larger the drag increment which they cause.

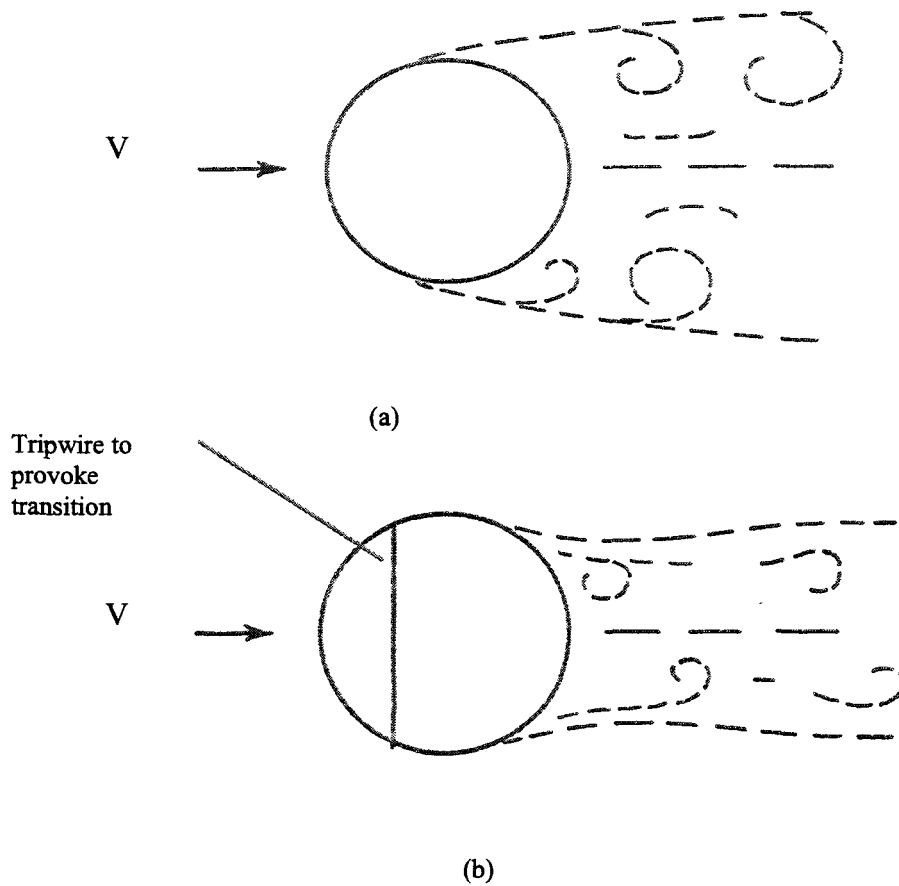


Figure 2.5 (a) Flow past a sphere with laminar boundary layer separation.

(b) Flow past a sphere with turbulent boundary layer separation.

It is of interest to note, however, that in certain cases it is possible to decrease the drag of a body by causing transition to occur earlier through surface roughness. Such cases only occur with bluff bodies and at Reynolds numbers which are sufficiently low for the boundary layer to separate early in the laminar state; the wake is then wide and the pressure drag high. If transition is then provoked before separation, the boundary layer, when it does separate, is turbulent and hence separates much further aft from the body than does the less robust laminar boundary layer. The wake is, in consequence, narrower

and the pressure drag is reduced, so that there is a marked net reduction in the total drag, as shown in Figure 2.5 (Duncan et al., 1970). Such a process may be observed in the case of a smooth bluff body like a sphere or cylinder as the Reynolds number increases. At low Reynolds numbers the boundary layer is wholly laminar and separates early from the surface causing a large eddying wake; the drag coefficient is in consequence high. With an increase of the Reynolds number a critical value is eventually reached at which the boundary layer goes turbulent before separation, and separation occurs later. The wake at that stage diminishes as does the drag coefficient. The Reynolds number at which this occurs is called the critical Reynolds number.

### **2.5.2 Effect of Reynolds Number and Roughness on the Thermal Boundary Layer**

In general, surface roughness tends to boost the convective HTC by hastening the boundary layer transition. As a result, in typical conditions of icing on stationary structures, the convective Heat Transfer Coefficient (HTC ) is 2-3 times higher for a rough cylinder than for a smooth cylinder. In typical aircraft icing conditions it may even be 5-6 times higher (Makkonen,1984).

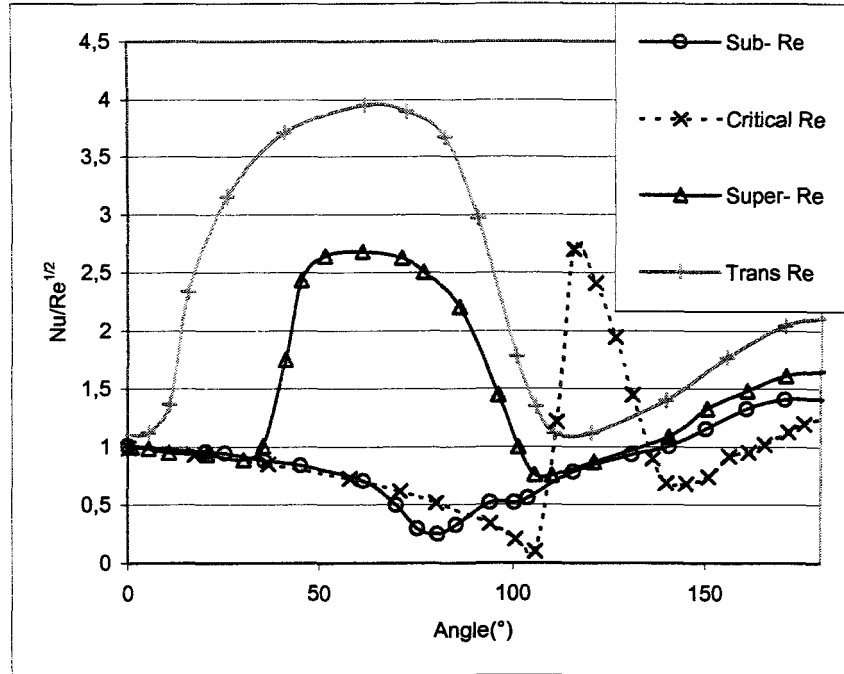


Figure 2.6 Flow past a sphere with laminar boundary layer separation.

In comparison with surface roughness, the influence of the Reynolds number of a flow on a rough object is far more profound. For an object of modest roughness ( $k_s/D=75 \times 10^{-5}$ ), each of the four flow ranges is represented in Figure 2.6 (Achenbach, 1977). In the sub-critical range ( $Re=9.2 \times 10^4$ ), the boundary layer is laminar throughout; its separation is indicated by a minimum close to  $\phi=80^\circ$ . The heat-transfer distribution in the critical flow range ( $Re=4.1 \times 10^5$ ) is characterized by the occurrence of separation bubbles located at the minimum Nu of close to  $\phi=105^\circ$ , as well as by the substantial rise of Nu in the region where the turbulent shear layer reattaches to the rear surface of the cylinder. At about  $\phi=140^\circ$ , the turbulent boundary layer separates as indicated by another minimum in the experimental curve. The curve  $Re=5.9 \times 10^5$  represents the supercritical flow range. There

is a direct transition from a laminar to a turbulent boundary at  $\phi=60^\circ$ , generating a high heat transfer coefficient downstream. The separation occurs at around  $\phi=115^\circ$ .

With a further increase of the Reynolds number, the laminar-turbulent transition point approaches the front stagnation point. At about  $Re=10^6$  the trans-critical flow range is reached, characterized by the presence of a turbulent boundary layer on the entire cylinder surface upstream of the separation point, except in the immediate vicinity of the front stagnation point.

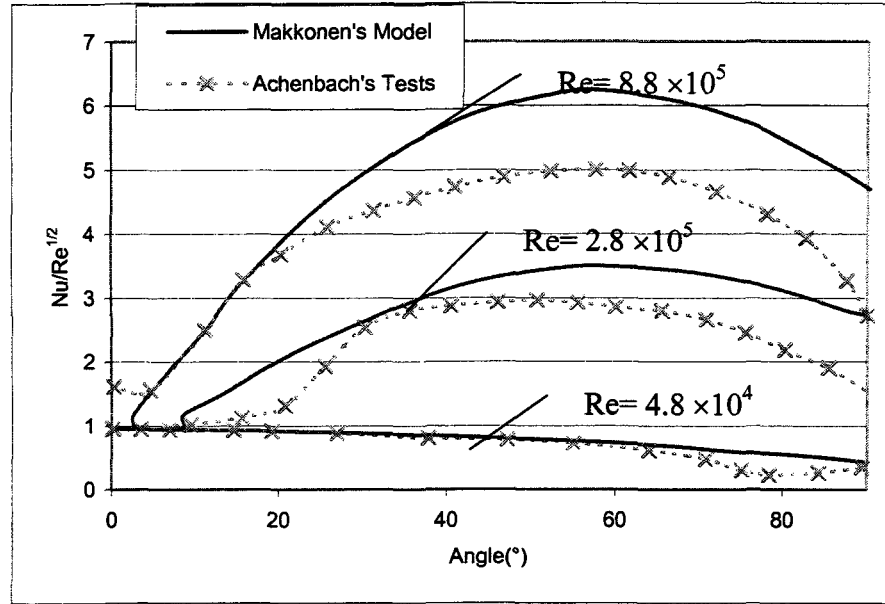


Figure 2.7 Local heat transfer coefficient  $Nu/Re^{1/2}$  on a rough circular cylinder at various cylinder Reynolds numbers. The cylinder diameter  $D$  is 15 cm, the roughness element height,  $k$ , is 0.9 mm, and the equivalent sand roughness  $k_s$  is 1.35mm. The solid lines are model simulations and the points are experimental values obtained by Achenbach (1977).

It should be pointed out that the critical Reynolds number decreases with an increasing roughness parameter,  $k_s/d$ ; this implies that at a given point on the surface of the cylinder,

the boundary layer undergoes transition from laminar to turbulent flow at decreasing Reynolds numbers (Achenbach, 1971).

Makkonen (1984) put forward a mathematical model to predict the local heat transfer coefficient along the cylinder surface, based on the integral equations of the boundary layer. The local velocity above the boundary layer, was evaluated from the potential flow velocity distribution around a cylinder. In particular, the local free-stream velocity above the boundary layer was obtained with the aid of the Bernoulli equation. The model calculation results were then compared with Achenbach's data (1977), as shown in Figure 2.7. The solid lines are model simulations, while the points represent experimental values obtained by Achenbach. For a small cylinder and a low Reynolds number, Makkonen's model correctly predicted the tendency of a laminar boundary layer to prevail at all angles on the upstream side, while no boundary layer transition occurs, and the heat transfer coefficient decreases slowly with an increasing angle  $\phi$ . An apparent discrepancy is found downstream, at the angular position of  $70^\circ$ , which might arise from the fact that the boundary layer separation was not taken into consideration in this model.

The Reynolds number in the case of cable icing lies within a range of  $10^4$  to  $10^5$ , and falls under sub-critical flow conditions. Thus, the windward side of the cable presents a primarily laminar boundary layer upstream of the separation point.

### **2.5.3 Evaluating the Nusselt Number for a Rough Cylinder**

- Makkonen's Correlation



The average convective heat transfer coefficient for a rough cylinder, as used by Makkonen, is valid for Reynolds numbers between  $7 \times 10^4$  and  $9 \times 10^5$ . The Reynolds number is a function of the cylinder diameter and is evaluated at the average temperature of the cylinder and air temperatures at the boundary layer.

$$\overline{Nu} = 0.032 Re^{0.83} \quad (E\ 2-12)$$

- Achenbach's Correlation

The local convective heat transfer coefficient for a rough cylinder, as measured by Achenbach, is estimated as a function of the Reynolds Number,  $Re$ , based on the diameter of the cylinder and the angular position,  $\theta$ .

$$Nu(\theta) = 1.2 Re^{0.5} (2 + \sin(3.6(\theta - 25^\circ))) \quad (E\ 2-13)$$

Eq. 2-13 was also used in Lozowski's model (1983) to estimate the heat transfer coefficient locally.

The mean value for the Nusselt number is obtained by integrating the Nusselt number along the effective cooling zone between  $-25^\circ$  and  $25^\circ$ , and then by applying integration to Eq. 2-13 which yields:

$$\overline{Nu} = 0.227 Re^{0.5} \quad (E\ 2-14)$$

- Grenier's Correlation

The average convective heat transfer coefficient used by Grenier (1986) was estimated as a function of the Reynolds number,  $Re$ , based on the diameter of the

cylinder and evaluated at the average temperature between the cylinder temperature and the air boundary layer temperatures.

$$\overline{Nu} = 0.2 Re^{0.61} \quad (E 2-15)$$

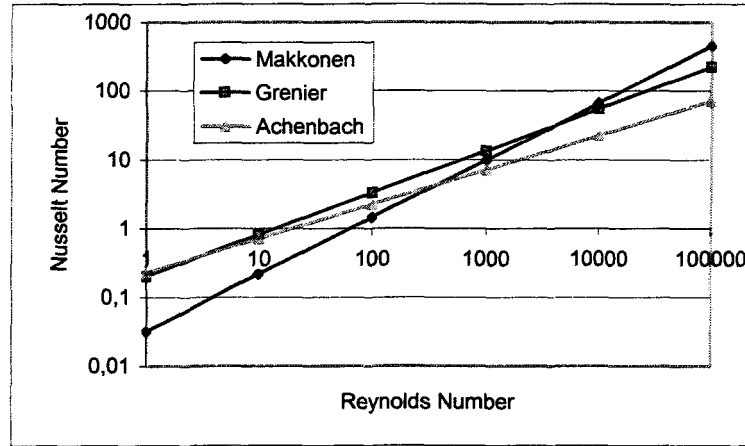


Figure 2.8 Nusselt number for a rough cylinder

Figure 2.8 shows three correlations graphically, representing those of Makkonen, Grenier, and Achenbach, respectively. It may be observed that the three curves in the figure are similar for Reynolds number lower than 10,000 while they differ from each other to a high degree elsewhere. At a Reynolds number of 100,000, for example, Makkonen's correlation predicts a Nusselt number three times greater than the one in Achenbach's correlation, and twice as great as the one in Grenier's correlation.

## 2.6 Thermodynamics of Ice Accretion

When applying the thermodynamics of ice accretion, the microphysical details are usually disregarded, and the impinging super-cooled water is considered as a continuum. According to Lozowski et al. (1983), the quantitative formulation in terms of a balance of heat fluxes at the icing interface may be written as:

$$Q_c + Q_e + Q_v + Q_k + Q_w + Q_f = 0 \quad (\text{E 2-11})$$

where the terms for the heat fluxes are as follows:

$Q_c$  is the sensible heat flux by convection between the accretion and the airflow streams  $= -\pi \cdot h(T_s - T_a)$ .

$Q_e$  is the evaporative or sublimate heat flux  $= h \left( \frac{\text{Pr}}{S_c} \right)^{0.63} \frac{\epsilon l_v}{p c_p} (e_a - e_s)$ ,

$Q_v$  is the heat flux due to aerodynamic heating  $= \pi \cdot h r_v V^2 / (2 c_p)$ , where  $V$  is local air speed.

$Q_k$  is the heat flux due to the conversion of droplet kinetic energy into heat  $= R_w V^2 / 2$ , where  $V$  is droplet impact speed.

$Q_f$  is the latent heat flux to the accretion due to freezing of some, or all, of the directly impinging water  $= l_{fs} R_w n$ , and  $l_{fs} R_s n$  due to freezing of runback water.

$Q_w$  is the sensible heat flux between the directly impinging water and the underlying accretion  $= c_w R_w (T_a - T)$ , and  $c_w R_s (T_s - T)$  between the runback water and the underlying accretion.

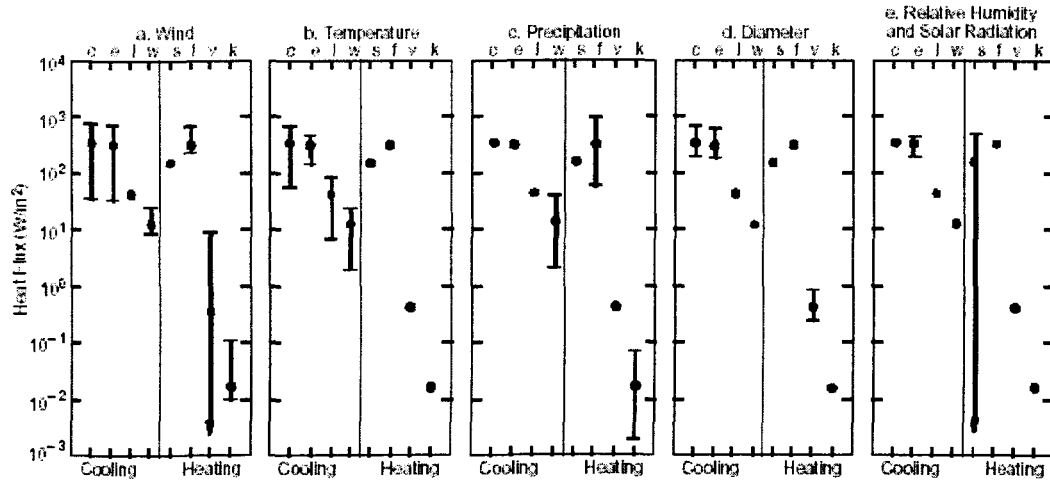


Figure 2.9 Comparison of heat flux terms in typical freezing-rain conditions. Standard conditions (black symbols) for the parameters are  $V = 3 \text{ m/s}$ ,  $T = -3 \text{ }^{\circ}\text{C}$ ,  $P = 3 \text{ mm/hr}$ ,  $Rh = 0.90$ ,  $Sr = 100 \text{ W/m}^2$ ,  $Dc = 3 \text{ cm}$ . In each plot one or two of these parameters is varied about the standard conditions as follows: (a)  $0 < V < 10 \text{ m/s}$ , (b)  $-6 < T < -0.5 \text{ }^{\circ}\text{C}$ , (c)  $0.5 < P < 10 \text{ mm/hr}$ , (d)  $0.5 < Dc < 10 \text{ cm}$ , (e)  $0.80 < Rh < 1.00$  and  $0 < Sr < 200 \text{ W/m}^2$ . Minimum convective and evaporative fluxes in (a) are provided by free convection. Key: e = evaporative cooling, c = convective cooling, l = longwave cooling, w = cooling from warming water, s = shortwave solar heating, f = heat of fusion, v = viscous heating, k = kinetic heating.

The respective magnitudes of these fluxes are compared in Figure 2.9 (Jones, 1996) for various ranges of temperature, wind speed, precipitation rate, relative humidity, and diffuse solar radiation typical of freezing-rain events. With regard to these fluxes, it should be noted that the convective cooling, evaporative cooling and heat of fusion are the most significant factors. Both the convective and evaporative heat flux are functions of the local Heat Transfer Coefficient (Nusselt number). The value of  $h$  may be influenced even further by the geometry of the ice accretion and its surface roughness.

## ***2.7 Surface Temperature of Ice Accretions***

Knowing which ice regime prevails at any given position on the ice surface is a prerequisite for calculating the surface temperature (Karev and Farzaneh, 2004). At the outset, a wet regime is assumed, and the corresponding surface temperature should be at the freezing point of water, or 0°C. The icing fraction is then calculated based on the thermal balance equation. If the calculation result does not lie between 0 and 1, the initial assumption is proved to be false. It may then be concluded that a dry regime has been attained and thus, that the corresponding icing fraction should be 1. In view of the fact that the heat balance equation is a non-linear function, a number of numerical methods may readily be applied to it.

## ***2.8 Ice Volume and Ice Density.***

The ice volume for an arbitrary surface element  $i$  at a time step  $j$  may be obtained from the equation as follows:

$$V_i^j = \frac{m_i^j}{\rho_i^j} \quad (\text{E 2-16})$$

where  $m_i$  denotes the ice mass, and  $\rho_i$  denotes the ice density.

The type of ice obtained from the surface of an iced object is a function of atmospheric and meteorological conditions. When ice is formed under different atmospheric and environmental conditions, it displays totally different patterns of behaviour. Ice may be

classified into three basic types, namely, glaze, hard rime, and soft rime. Rime comes into being when the conditions are such that supercooled water droplets freeze instantly at the moment of impact. There is no unfrozen water on the surface and this absence promotes surface roughness. Hard rime is opaque due to the presence of air bubbles which are trapped during the rapid freezing process. Supercooled droplets may be trapped on the surface since they do not freeze upon impact, and they tend to gather together to form larger droplets. Usually, surface droplets are larger than impinging droplets and this fact helps to explain why rough elements may also be observed on certain accretions of hard rime. The presence of these rough elements on the surface leads to an increase in the rate of heat transfer, which in turn speeds up the ice build-up process. In some extreme cases, a protuberance composed of a mixture of rime and glaze emerges. Glaze is characterized by a slower freezing process due to the presence of some large-sized supercooled droplets. Of the three types of ice, glaze is of the highest density and its surface is smooth and transparent. In general, the density of ice is a function of surface temperature. For wet accumulations, the surface temperature may reach zero and the density may go as high as  $917\text{kg/m}^3$ . For dry accumulations, the surface temperature is lower than  $0^\circ\text{C}$  and the corresponding density varies over a wide range.

Equation 2-16 dictates that ice density may affect the predicted ice shape to such a degree that great care should be taken when dealing with this parameter. The mass of the frozen fraction is derived from the thermal balance equation, as described in Eq. 2-11. The ice thickness is inversely proportional to its density. Ice density may be calculated by using certain empirical formulae which were usually obtained from curves generated by

experimental data. Most of these formulae, however, are functions of the Macklin parameter.

### 2.8.1 Ice Density Formula based on Macklin's Parameter

Macklin's density parameter (1962) is defined in the formulation:

$$R = V_0 d_m / (2t_s) \quad (\text{E 2-17})$$

where  $d_m$  is the median volume diameter of the droplets ( $\mu\text{m}$ );  $V_0$  is the impact speed of the droplets ( $\text{ms}^{-1}$ ) at the stagnation point as obtained from droplet trajectory calculations (Langmuir & Blodgett, 1946); and  $t_s$  is the local surface temperature on the iced surface ( $^{\circ}\text{C}$ ).

- Macklin's Ice Density (1962)

The first equation for ice density was developed by Macklin and is a function of the Macklin parameter:

$$\rho_i = \rho_{ref} \left( \frac{R}{R+1.5} \right)^2 \quad (\text{E 2-17})$$

$\rho_{ref}$  is a reference density corresponding to water density at  $4^{\circ}\text{C}$ .

- Bain and Gayet's Ice Density (1983)

This equation was defined by Bain and Gayet and is also a function of the Macklin parameter:

$$\begin{aligned} \rho_i &= 0.11R^{0.76} && \text{for } R \leq 10, \\ \text{or } \rho_i &= R(R+5.61)^{-1} && \text{for } 10 < R \leq 60, \end{aligned}$$

$$\text{or } \rho_i = 0.917 \quad \text{for } R > 60. \quad (\text{E 2-19})$$

- Jones and Macklin's Ice Density (1988)

This equation was defined by Jones and Macklin and is a function of the Macklin parameter:

$$\begin{aligned} \rho_i &= 0.218R^{0.51} && \text{for } R \leq 10, \\ \text{or } \rho_i &= R(1.13R + 2.15)^{-1} && \text{for } 10 < R \leq 60, \\ \text{or } \rho_i &= 0.84 && \text{for } R > 60. \end{aligned} \quad (\text{E 2-20})$$

- Makkonen and Stallabrass's Ice Density (1984)

This equation was developed by Makkonen and Stallabrass, and is a function of the Macklin parameter in the following formulation:

$$\rho_i = 387 + 425 \log(R) - 0.0823(\log(R))^2 \quad (\text{E 2-21})$$

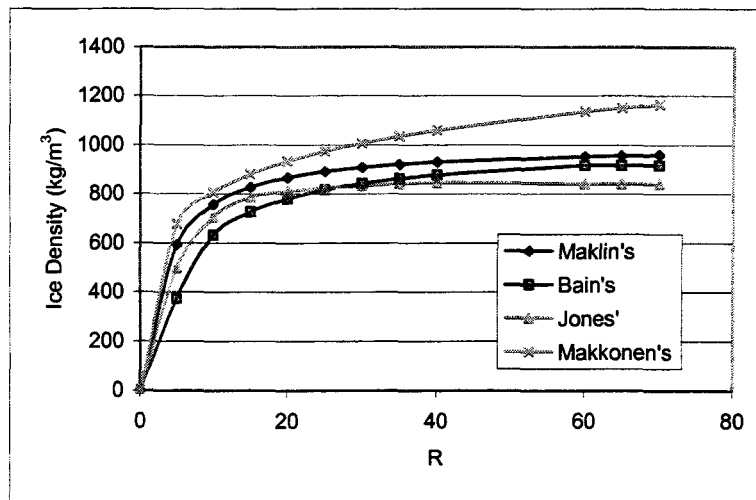


Figure 2.10 Relationship between ice density and Maklin number



Figure 2.10 shows four correlations graphically, representing those of Macklin, Bain, and Jones, and Makkonen, respectively. It may be observed that, of these four formulae, Makkonen's correlation predicted the highest ice density over the entire Macklin-number range while Bain's produces the lowest value over the small Macklin-number section, and then Jones' ice density takes its place to become the lowest over the large Macklin-number section.

### 2.8.2 LEWICE Ice Density

The equation developed by LEWICE is a function of the frozen fraction of supercooled water,  $f$ , as follows:

$$\rho = 917 \cdot (1 - f) + 840 \cdot f \quad (\text{E 2-22})$$

## 2.9 Conclusion

This chapter has introduced relevant aspects of modeling ice accretion processes, including the basic principles of an ice model, the evolution of techniques used in modeling this process as well as a number of specific researches on aspects of the ice model.

## CHAPTER 3

### AIRFLOW COMPUTATION

#### 3.1 Introduction

Airflow computation plays an essential role in the icing model under discussion. Once the velocity field is established, it is possible to evaluate air drag force over the water droplet and, in turn, to determine its trajectory; the local convective heat transfer rate may be evaluated according to the velocity distribution on the airflow boundary, while it is possible to determine the motion of surface runback water according to the surface air shear stress derived from the same airflow computation. Also, the calculation procedure proposed herein was carried out in a time-dependent manner, and hence it responds fully to the shape change of an iced object. It should be noted that time-dependent airflow computations make it possible for droplet trajectory calculations, as will be seen in the next chapter.

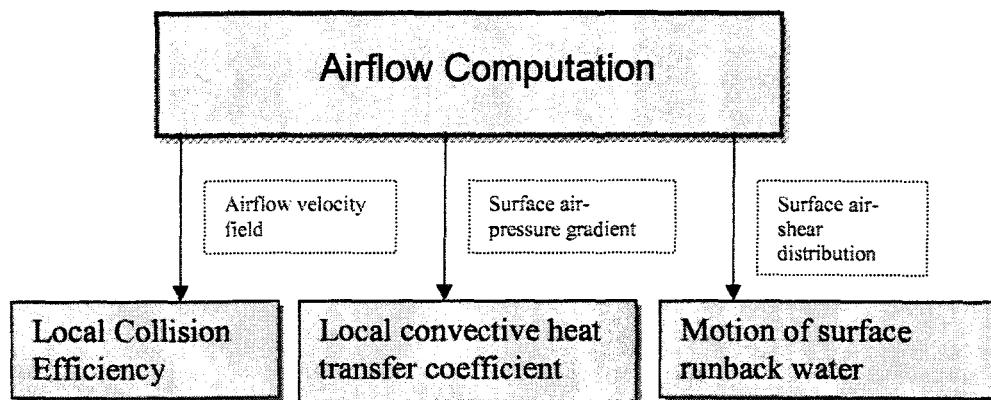


Figure 3.1 Airflow computation and its role in the ice model

The airflow across an iced object is a compressible and viscous flow which is governed by the set of Navier-Stokes differential equations. A converging solution to this equation

has proved to be costly and time-consuming from a computational point of view, thus there is little purpose at present in incorporating it in the proposed ice model. In practical applications, a full solution to the flow field is unnecessary, since the calculation is only required for the upstream airflow where the cylindrical object receives the major portion of water droplet impingement.

Boundary layer theory was applied here to evaluate the airflow field. According to this theory, the airflow about an obstacle can be divided into two regions, namely, the inviscid free-stream flow or potential flow, and the viscous flow boundary layer in the vicinity of the object. Physically, these two regions border each other and share the same boundary, as shown in Figure 3.2. Accordingly, flow calculation was divided into two iterative steps composed of free-stream and boundary layer calculations. These two steps are mutually correlative and are repeated until convergence is reached.

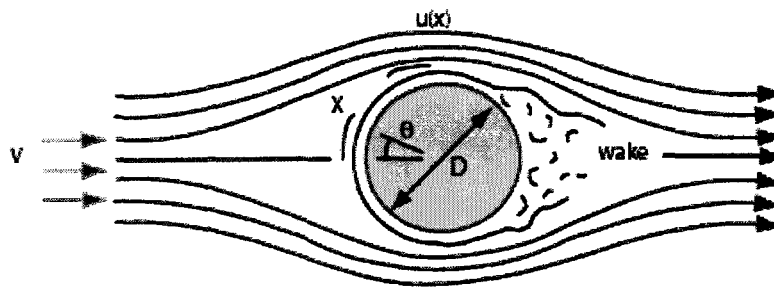


Figure 3.2 The airflow field about an object

Currently, the Finite Element Method (FEM), the Panel Method, and the Boundary Element Method (BEM) are the numerical procedures commonly used in solving the potential flow. When compared with the latter two, the FEM requires a complete discretization of the entire flow field, and thus demands the greatest amount of

computational time and resources. The BEM is superior to the Panel Method, which is itself an indirect BEM, since it deals with such physical properties of flow as potential and flux instead of sources and vortex density as is the case in the Panel Method (N.Bazeos et al., 1990). This is one reason why the Boundary Element Method (BEM) is used to solve for the potential flow.

### ***3.2 Basic Principles***

As mentioned above, the computation for airflow was divided into two independent calculations, one for the potential flow and the second for the boundary layer. These calculations are carried out in an iterative manner, as shown in Figure 3.3. The free-stream velocity distribution at the boundary, obtained from the potential flow calculation, is an input parameter for calculating the boundary layer. The separation point of the boundary layer affects the free-stream velocity field to a considerable degree by changing the contour of the flow boundary layer. The potential flow calculation yields the free-stream velocity distribution along the outer edge of the boundary layer, and this distribution is subsequently used in the boundary-layer calculation to determine the relevant separation points. The boundary shape used in a subsequent iteration can thus be determined according to the separation points obtained from the iteration in process. Since the boundary separation point is not yet known at the outset, it is assumed that no boundary layer separation has occurred for the first attempt.

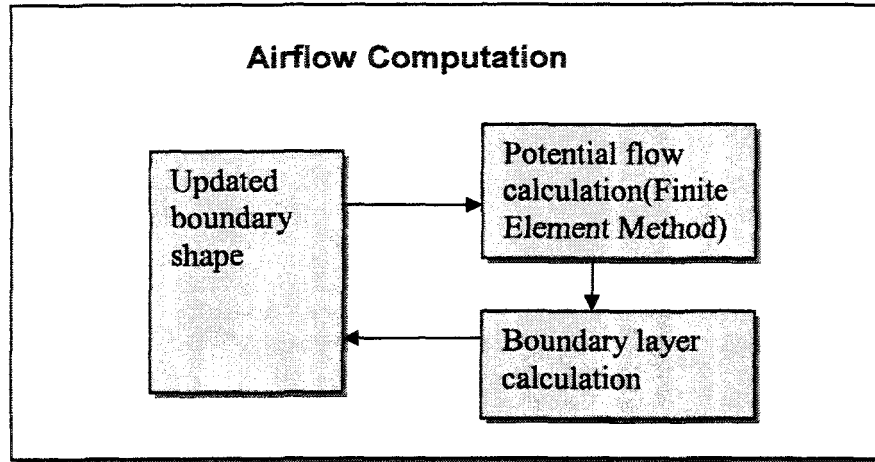


Figure 3.3 Calculation procedure for airflow computation

### 3.3 Potential Flow

As indicated earlier, potential flow is an ideal, irrotational and incompressible flow which can be solved numerically by using the BEM. The flow around an object may be viewed as the combination of a uniform stream and a disturbance flow according to the theory of flow superposition. The uniform stream is of initial velocity when the border of the body is seen as transparent, thereby allowing the stream to enter and exit freely. The disturbance flow simulates the effect imposed by an immersed body. Accordingly, the stream function,  $\varphi$ , at any position in the flow field may be expressed as a combination of the initial stream,  $\varphi_1$ , and the disturbance flow,  $\varphi_2$ , as follows:

$$\varphi = \varphi_1 + \varphi_2 \quad (\text{E 3-1})$$

where  $\frac{\partial \varphi}{\partial x} = v_y$  and  $\frac{\partial \varphi}{\partial y} = v_x$ .

The equation  $\varphi_1 = V_0 y$ , defines the steady onset flow, and  $\varphi_2$  is a perturbation stream function induced by the immersed object. Since the disturbance flow is incompressible and irrotational, and thus of zero divergence, it may be expressed in the form of Laplace's equation, as follows:

$$\nabla^2 \varphi_2 = 0 \quad (\text{E 3-2})$$

Since the uniform stream  $\varphi_1$  is known, it is possible to solve the variable  $\varphi_1$  in terms of the disturbance stream  $\varphi_2$ .

The boundary conditions of the problem may be written as  $\varphi_2 = -\varphi_1 = -V_0 y$  on  $\Gamma$ , if the function value of the streamline on the surface of the object,  $\Gamma$ , is tentatively assumed as zero in the formulation  $\varphi = 0$ . For general application,  $\varphi_2$  will be replaced by  $\phi$  when Eq. 3-2 is transformed in accordance with the BEM in the following section.

When Equation (E 3-2) is implemented with the residual integral equation according to the Galerkin method, this equation may be written as follows:

$$I = \int_A \phi \cdot \nabla^2 \phi dA = 0 \quad (\text{E 3-3})$$

By applying Green's theorem and integrating the above equation by parts, Equation (E 3-3) may be written as follows:

$$\int_A \phi (\nabla^2 \phi) dA = - \int_A \phi (\nabla^2 \phi) dA + \int_{\Gamma} \phi \frac{\partial \phi}{\partial n} d\Gamma - \int_{\Gamma} \phi \frac{\partial \phi}{\partial n} d\Gamma = 0 \quad (\text{E 3-4})$$

The fundamental solution to the 2-D problem can be written as follows:

$$\phi = \frac{1}{2\pi} \ln\left(\frac{1}{r}\right) \quad (\text{E 3-5})$$

According to its definition, the fundamental solution represents the field generated by a concentrated unit charge acting at a point,  $i$ . The effect of this charge is propagated from  $i$  to infinity without any consideration of boundary conditions.

Equation 3-5 may also be written as  $\nabla^2 \phi + \Delta^i = 0$  where  $\Delta^i$  represents a Dirac Delta function which tends to be infinite at point  $i$  and is equal to 0 elsewhere. The integral of  $\Delta^i$  is equal to 1 in the formulation  $\int_A \nabla^2 \phi = 1$ .

Based on these considerations, Equation (E 3-4 ) can be written at point  $i$  as

$$\phi = \int_{\Gamma} \phi \frac{\partial \phi}{\partial n} d\Gamma - \int_{\Gamma} \phi \frac{\partial \phi}{\partial n} d\Gamma \quad (\text{E 3-6})$$

Applying Green's third law and integrating (E 3-6) by parts yields

$$C_i \phi_i + \sum_{j=1}^n \int_{l_j} \phi \frac{\partial \phi}{\partial n} dl = \sum_{j=1}^n \int_{l_j} \phi \frac{\partial \phi}{\partial n} dl \quad (\text{E 3-7})$$

where  $C_i = \frac{\theta}{2\pi}$  in which  $\theta$  is the internal angle of the corner in radians.

Defining  $q = \frac{\partial \phi}{\partial n}$  and replacing  $\frac{\partial \phi}{\partial n}$  with  $q$ , the equation (E 3-7) can be transformed into

the following formula:

$$C_i \phi_i + \sum_{j=1}^n \int_{l_j} \phi \frac{\partial \phi}{\partial n} dl = \sum_{j=1}^n \int_{l_j} \phi q dl \quad (\text{E 3-8})$$

When the boundary is divided into  $n$  segments or elements, the values of  $\phi$  and  $q$  at any point on an arbitrary element may be defined in terms of their nodal values and two linear

interpolation functions,  $N_1$  and  $N_2$ , which are given in terms of the homogeneous coordinate  $\xi$ , a dimensionless coordinate varying from  $-1$  to  $+1$ .

$$\varphi(\xi) = N_1 \cdot \varphi_1 + N_2 \cdot \varphi_2 = \begin{bmatrix} N_1 & N_2 \end{bmatrix} \begin{bmatrix} \varphi_1 \\ \varphi_2 \end{bmatrix} \quad (\text{E 3-7})$$

$$q(\xi) = N_1 \cdot q_1 + N_2 \cdot q_2 = \begin{bmatrix} N_1 & N_2 \end{bmatrix} \begin{bmatrix} q_1 \\ q_2 \end{bmatrix} \quad (\text{E 3-8})$$

where

$$N_1 = 0.5 * (1 - \xi) \quad (\text{E 3-9})$$

$$\text{and} \quad N_2 = 0.5 * (1 + \xi) \quad (\text{E 3-10})$$

Substituting  $\varphi$  and  $q$  with Equation (E 3-7) and (E 3-8), Equation (E 3-6) becomes,

$$C_i \varphi_i + \sum_{j=1}^n \begin{bmatrix} h_{ij}^1 & h_{ij}^2 \end{bmatrix} \begin{bmatrix} \varphi_1 \\ \varphi_2 \end{bmatrix} = \sum_{j=1}^{2n} \begin{bmatrix} g_{ij}^1 & g_{ij}^2 \end{bmatrix} \begin{bmatrix} q_1 \\ q_2 \end{bmatrix} \quad (\text{E 3-11})$$

$$\text{where } h_{ij}^1 = \int_{\Gamma_j} N_1 \frac{\partial \phi}{\partial n} d\Gamma, \quad h_{ij}^2 = \int_{\Gamma_j} N_2 \frac{\partial \phi}{\partial n} d\Gamma,$$

$$g_{ij}^1 = \int_{\Gamma_j} N_1 \phi d\Gamma, \text{ and } g_{ij}^2 = \int_{\Gamma_j} N_2 \phi d\Gamma.$$

Substituting (E 3-11) into (E-6) yields:

$$C_i \varphi_i + \sum_{j=1}^n H_{ij} \varphi_j = \sum_{j=1}^{2n} G_{ij} q_j \quad (\text{E 3-12})$$

where  $H_{ij}$  is equal to the  $h_{ij}^1$  term of element  $j$  plus the  $h_{ij-1}^2$  term of element  $j-1$ .

For a closed boundary  $H_{ii} = - \sum_{j=1 \text{ and } j \neq i}^n H_{ij}$ , while for an open boundary  $H_{ii} = 1 - \sum_{j=1 \text{ and } j \neq i}^n H_{ij}$ .



The formulae used to obtain the nodal values for velocities in the flow field are the following:

$$v_x = \frac{\partial \phi}{\partial y} = \int_{\Gamma} q \left( \frac{\partial u^*}{\partial y} \right) d\Gamma - \int_{\Gamma} u \left( \frac{\partial q^*}{\partial y} \right) d\Gamma \quad (\text{E 3-13})$$

$$v_y = \frac{\partial \phi}{\partial x} = \int_{\Gamma} q \left( \frac{\partial u^*}{\partial x} \right) d\Gamma - \int_{\Gamma} u \left( \frac{\partial q^*}{\partial x} \right) d\Gamma \quad (\text{E 3-14})$$

The above relations still hold for the external potential flow, since the disturbance flow at infinity satisfies the Gauss condition in the formulation  $\int_{\Gamma} q d\Gamma \equiv 0$ , and thus it is valid

when applying the same formulae to solve external flow problems. The entire flow field was discretized into a grid of 800×800 volume elements, and the nodal values of flow velocity may be determined by applying Equations (E 3-8) and (E 3-9) to each node of this grid. The velocity at any given point may then be obtained by linear interpolation.

- **Boundary Conditions**

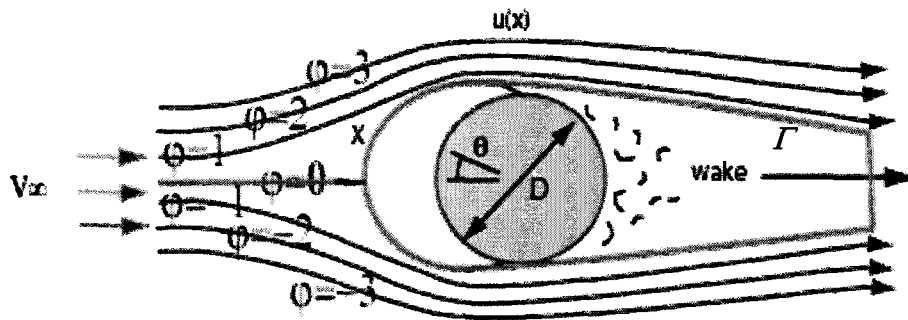


Figure 3.4 Input parameters and boundary conditions for BEM calculation.

By definition, a streamline is a locus of points having a constant value of the stream function. It may be assumed that the air stream around an object is composed of an array

of streamlines, the values of which may be defined in the way indicated in Figure 3.4. In order to solve the external flow around the obstacle body, the flow boundary,  $\Gamma$ , was defined in such a way as to coincide with the outer edge enclosing the object and its resultant wake. The boundary of the wake was determined on the basis of the assumption that the air boundary layer separates from the object surface in the tangential direction. The value of the streamline passing along this boundary may be treated as zero in the formulation  $\varphi = 0$ .

- **Time-Dependent Boundary Discretization**

During model simulation, the shape of the boundary,  $\Gamma$ , should be updated over time in response to the position changes of the boundary layer separation points, as indicated by the heavy green line in Figure 3.4. At the outset, no flow boundary separation was assumed and the surface of the object was taken as the initial boundary for the BEM calculation.

### ***3.4 Airflow Boundary Layer***

The fluid boundary layer may be evaluated based on the free-stream velocity distribution on the outer edge of the flow boundary. In the empirical formulae, which will be introduced in subsequent sections, this velocity distribution is integrated along the surface of the object so as to determine the positions of transition points and separation points. These formulae will also be used for the further evaluation of such parameters as the momentum thickness and frictional coefficient for both laminar and turbulent sections.

### 3.4.1 Laminar Boundary Layer

The laminar boundary layer under a pressure gradient is governed by the integral momentum equation as described by Duncan (1970). The direct application of this equation proved to be impossible from a practical point of view due to the difficulty in defining the term for the velocity profile in the presence of a pressure gradient. The Thwaites method described in the book (Gerhart et al., 1992), however, demands no such prerequisite, and is thus the most viable way of evaluating the laminar boundary layer. The feasibility of this method is further confirmed by its wide use in related areas of research. The Thwaites method (1949) may be formulated as follows:

$$\Theta^2 - \Theta_0^2 = \frac{0.45U_0}{U_x^6} \int_{x_0}^x U_x^5 dx \quad (\text{E 3-15})$$

where  $\Theta$  is the momentum thickness;

$U_0$  is the onset flow velocity;

$U_x$  is the free-stream velocity on the boundary;

and  $x_0$  denotes the location of the stagnation point in the surface-attached coordinate system.

$U_0$  is an input parameter for the ice model, and  $U_x$  may be obtained from the potential flow calculation, as described in the preceding sections. If the integration starts from the stagnation point,  $x_0$  may be replaced by 0. Thus, Equation 3-15 may be solved for any position in the laminar boundary layer. The calculation procedure may be carried out according to the following steps:

- a) Obtain  $U(x)$  from potential flow calculation, taking  $\Theta_0$  as zero when calculation starts from stagnation point.
- b) At any  $x$ , calculate momentum thickness,  $\Theta$ , from Equation 3-8.
- c) Calculate dimensionless pressure gradient,  $\lambda$ , in formulation  $\lambda \equiv \frac{\Theta^2}{\nu} \left( \frac{dU_x}{dx} \right)$  and evaluate  $R_\Theta$  according to  $R_\Theta \equiv \frac{U\Theta}{\nu}$ .
- d) Calculate air shear stress,  $T$ , according to  $T(\lambda) \approx (\lambda + 0.09)^{0.62}$  and shape factor,  $H$ , according to  $H(\lambda) \approx \begin{cases} 2.61 - 3.75\lambda + 5.24\lambda^2 & (\lambda > 0) \\ \frac{0.0731}{0.15 + \lambda} + 2.088 & (\lambda < 0) \end{cases}$
- e) Calculate skin-friction coefficient,  $C_f$ , using formula  $C_f = 2T_\Theta(\Lambda) / R_\Theta$ .
- f) Calculate wall shear stress,  $T_w$ , according to  $T_w \equiv \frac{\mu T U_x}{\Theta}$ .
- g) Calculate boundary thickness,  $\delta^*$ , according to  $H = \frac{\delta^*}{\Theta} = H(\Lambda)$ .

### 3.4.2 Turbulent Boundary Layer

The airflow sweeping across the iced object is characterized by a high Reynolds number. Under the influence of surface roughness, the initial laminar boundary flow tends to become unsteady and a flow boundary transition may thus occur earlier. There are few satisfactory methods for solving the Reynolds-averaged equations which hold particularly for the turbulent boundary layer (Kays and Crawford, 1993). Nevertheless, a

number of integral approximations are available for evaluating the turbulent boundary layer empirically.

The approximate method developed by Spence (Duncan et al., 1970) is in use currently and has wide application in a number of related research fields. The approximation may be written as follows:

$$\frac{d\Theta}{dx} + \frac{U_x'}{U_x}(H+2)\Theta = \frac{\tau_w}{\rho U^2} = \frac{1}{\zeta^2} \quad (\text{E 3-9})$$

where  $\Theta$ ,  $H$ ,  $x$ ,  $U_x$  and  $\tau_w$  bear the same definitions as those shown above, while  $\zeta$  is a dimensionless parameter. It is necessary to establish the relations between  $\Theta$ ,  $H$ , and  $\zeta$  in order to obtain a solution for  $\Theta$ . Experimental results have shown that the velocity profile may be viewed as a single-parameter function of  $H$  for the turbulent boundary layer (Duncan, 1970), while Spence further suggested using the following exponential approximate formula for the velocity profile when there is a large adverse pressure gradient:

$$\frac{U_y}{U_x} = \left(\frac{y}{\delta}\right)^{\frac{H-1}{2}} \quad (\text{E 3-10})$$

where  $y$  is measured normal to the  $x$  coordinate, and penetrates into the boundary layer. The integral equation may be solved using  $H=1.5$ , and an empirical integral equation in terms of  $\Theta$  may thus be obtained.

$$\Theta^{6/5} U_x^{4.2} - \Theta_t^{6/5} U_t^{4.2} = 0.0106 \text{Re}^{-1/5} \int_{x_t}^x U_x^4 dx \quad (\text{E 3-11})$$

where  $x_t$  is the coordinate at the transition point, and  $U_t$  is the free-stream velocity at the outer edge of the boundary layer. According to Duncan (1970), the validity of applying

Eq. 3-11 is supported by the fact that the momentum thickness,  $\Theta$ , is insensitive to the choice of the shape coefficient,  $H$ . From Ludwig-Tillman's equation, it is possible to obtain the friction coefficient using:

$$C_f = 0.246 R_\Theta^{-.268} 10^{-0.678 H} \quad (\text{E 3-12})$$

where the dimensionless parameter  $R_\Theta$  is the momentum thickness and may be defined as

$$R_\Theta = U_x \Theta / \nu.$$

In order to evaluate the shape coefficient  $H$  with greater precision than heretofore, Spence's equation should be used, and may be written as follows:

$$U_x^2 X(H) = C_1 - 0.0014 \int_{x_i}^x \frac{U_x^2}{\Theta R_\Theta^{1/5}} dx \quad (\text{E 3-13})$$

where  $X(H) = 2.105 - \frac{0.442}{(H-1)}$ , and  $C_1 = [U_x^2 X(H)]_{x=x_i}$ .

The wall shear stress,  $\tau_w$ , can be evaluated according to the following formula:

$$\tau_w = \frac{\rho U_x^2}{2C_f} \quad (\text{E 3-14})$$

### 3.4.3 Transition Points

In the preceding sections, a concentrated effort was made to develop integral formulae for solving the velocity laminar boundary layer and turbulent boundary layer. These formulae on their own, however, are not sufficient to complete the task of evaluating the specific flow boundary layer under investigation. Additional work should be done in order to determine the transitional zone where the laminar boundary flow turns into a

turbulent boundary flow. It should be noted that the transition is an incremental process, rather than an abrupt one. It is still valid to assume, however, that the dimension of the transition section is as small as a point for the flow under discussion, and may be evaluated on the basis of the momentum thickness:

$$R_{\theta} = 1.174 \left[ 1 + 22400 / R_x \right] R_x^{0.46} \quad (\text{E 3-15})$$

and the generally acceptable value for the critical Re number is

$$R_{x_{tr}} = 3.2 \times 10^5 \quad (\text{E 3-16})$$

From Michel's expression (*in* Duncan, 1970), the critical Reynolds number may be obtained in terms of the momentum thickness as follows:

$$R_{\theta_{cr}} = 430 \quad (\text{E 3-17})$$

This method provides a high degree of accuracy, since the local pressure gradient is taken into account.

### 3.4.4 Separation Points

The task of determining the separation point may be carried out by using the Strafford correlation method, whose validity has already been verified experimentally by Cebeci (1974). By dividing the flow boundary layer into two regions, namely, the internal and external regions, Strafford associated the separation criterion with the pressure gradient of the external boundary layer, which may be formulated as follows:

$$C_p \left( x \frac{dC_p}{dx} \right)^{1/2} (10^{-6} Re_x)^{-1/10} = f(x) \quad (\text{E 3-18})$$

where  $C_p = 1 - (\frac{U}{U_a})^2$ , in which  $U_a$  is the flow velocity at the starting point of the adverse gradient.

If a laminar section or a favorable pressure gradient develops in the boundary layer, it is necessary to substitute  $x$  with  $(x - x')$ , and  $R_x$  with  $U_m(x - x')/\nu$ . The factor  $x'$  represents the distance from the imaginary stagnation point to the point of inception of the adverse gradient. The factor  $x'$  is calculated using the Spence equation as follows:

$$x' = x_m - \int_{x_i}^{x_m} (\frac{U_x}{U_m})^4 dx - 94.3 \Theta_r R_{\Theta_r}^{1/5} (u_i/u_m) \quad (\text{E 3-19})$$

where  $x_m$  is the position of minimum pressure,

$\Theta_r$  is the momentum thickness at the transition point, and

$R_{\Theta_r}$  is the non-dimensional momentum thickness at the transition point.

It is opportune, at this point, to evaluate these expressions numerically so as to obtain the function  $f(x)$  as a criterion to be used for estimating the separation point. In formulation, this function may be detailed as follows:

$f(x) \leq 0.3$  no separation detected;

$0.3 \leq f(x) \leq 0.5$  separation detected at point where maximum value is found;

$0.5 \leq f(x)$  separation detected at point where  $f(x) \equiv 0.5$ .

### **3.5 Feedback Effect in Airflow Calculations due to Boundary Layer Separation**

Since the two interactive zones, potential flow and boundary layer, cannot be evaluated independently, iteration of calculations was made in order to determine the boundary



layer separation points and therefrom, a new boundary geometry for the subsequent free-stream computation. The iteration process should not be terminated until a convergent solution is obtained. For the particular airflow under discussion, it was found that, after three successive iterations, the boundary layer separation points display no apparent change, as may be observed in Figure 3.5. Therefore, in order to save valuable computation time, three iterations in the computer code were considered ample for attaining the sought-for accuracy.

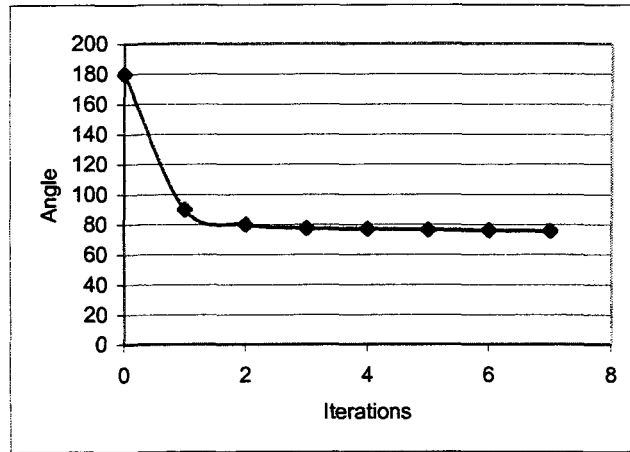


Figure 3.5 Evolution of angular position for boundary-layer separation points during simulation.

### ***3.6 Computation of Airflow Past an Object with an Arbitrary Cross-sectional Shape***

In the BEM-based potential flow calculation described above, the flow boundary is assumed to coincide with the surface of the object and hence there must be a free streamline passing along the same surface. This assumption, however, only holds for the initial stage of ice accretion when the surface is still smooth. As ice builds up, the

surface of the iced body presents increasing surface asperity, and as a result, it can no longer be used directly for potential flow calculation. In such a case, a specific calculation procedure is designed to determine the flow boundary based on the original geometry of the ice-covered object, and may only be applied to the upstream surface. Such a practice may be justified by the fact that the trajectories of the droplets directed towards the object were affected primarily by the upstream airflow.

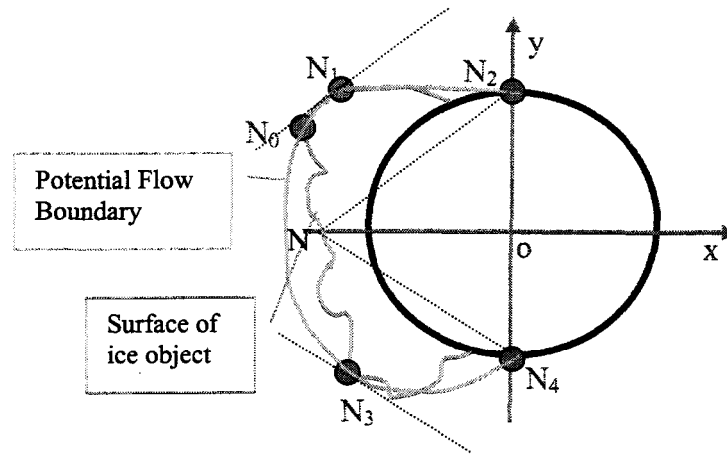


Figure 3.6 Algorithm for surface smoothing

### 3.6.1 Determining the Control Points

1. Find the leftmost point of the iced object,  $N_0$ .
2. Find the nodes which are farthest from  $NN_2$  and  $NN_4$ , i.e.  $N_1$  and  $N_3$  (see Figure 3.6).
3. Find the nodes intersected by the  $y$  axis, i.e.  $N_2$  and  $N_4$ . These two nodes together with  $N_0$ ,  $N_1$  and  $N_3$ , mentioned above, will be used as control points to generate a new curve which will represent the updated flow boundary.

### **3.6.2 Algorithm for Boundary Curve Based on Control Points Developed Above**

A number of algorithms may be taken from among the available options, and the curves generated by these algorithms may be totally different in shape. A number of important curve-generating algorithms are listed below:

- **The Lagrange Polynomial (LP)**

The curve generated from the Lagrange polynomial will pass through all the control points. Given the  $n+1$  data points, the polynomial so developed is of a degree  $n$ . For large  $n$ , such a curve would be too loose and it may also oscillate excessively. In practice, a tight curve is preferred. Also, the LP is unique. In principle, there are an infinite number of curves that pass through any set of given points, and the intended one may not happen to be the LP. As a result, it may be concluded that a useful curve should be of a low degree by nature and should depend on parameters that affect the shape of the curve.

- **The Bézier Curve**

The Bézier curve is a parametric curve  $P(t)$  which is a polynomial function of the parameter  $t$ . The degree of the polynomial depends on the number of points used to define the curve. The method uses control points to produce an approximating curve which does not pass through the interior control points but is attracted by them.

- **The B-Spline**

The B-Spline curve overcomes the main disadvantages of the Bézier curve, namely, (i) the degree of the Bézier curve depends on the number of control points, (ii) it provides

only global control, and, (iii) individual segments are easy to connect with C1 continuity, but C2 is difficult to obtain. The B-spline curve features local control and any desired continuity. In addition to the above-mentioned control points, the values of certain quantities called “knots” are real numbers and may offer additional control over the shape of the curve.

The B-Spline algorithm was adopted, particularly because the order of this parametric function does not increase as the number of control points grows. This same algorithm will be used later on in the research to fit a particular set of control points, thereby generating an artificial surface which will represent the airflow boundary.

### ***3.7 Airflow Field Visualization***

Figure 3.7 shows the airflow simulation results after executing the present ice code. The graphs in Figures 3.7 (a) and (b) represent the airflow patterns for the original non-iced cylindrical object and the ice-covered object, respectively. For the cylinder, the airflow is symmetrical in the windward direction, and airflow separation occurs at an angle of about  $80^\circ$ , as shown in Figure 3.7 (a). According to observations made by Duncan (1970), this separation occurs in the laminar section, rather than in the turbulent one. The mechanism involved in this type of separation may be explained by the fact that the Reynolds number in such a case is less than  $10^5$ . Accordingly, the laminar boundary layer remains relatively stable, making it difficult for this layer to transform itself into a turbulent boundary layer. The pattern of airflow velocity distribution is more sophisticated in the case of the iced object of a complex geometrical shape, as shown in

Figure 3.7 (b). It should furthermore be noted that, for a flow about an ice-covered cable, the boundary layer separation is dependent to a high degree on the individual geometry of the cable.

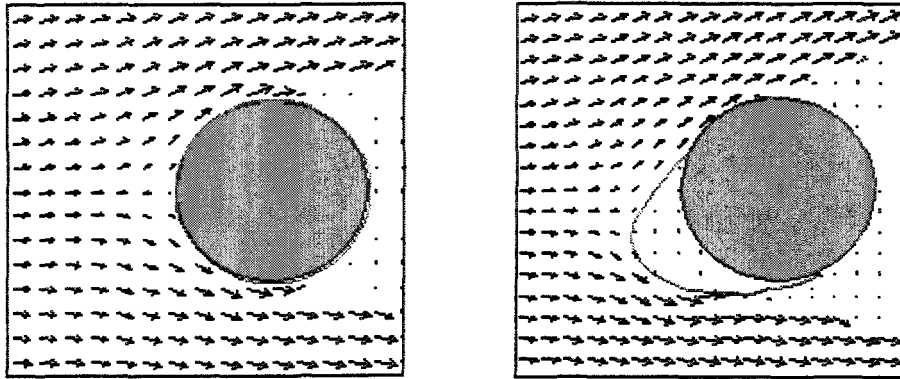


Figure 3.7 Airflow (a) about a plain object, and (b) about an ice-covered object

### ***3.8 Conclusions***

This chapter provided a discussion of the details of the methods used to perform airflow computations in the proposed ice model. The velocity distributions obtained from model calculations were then presented and analyzed. The validity of using these methods was verified by referring to certain related research provided in the review of the literature.

## CHAPTER 4

### DROPLET TRAJECTORY AND COLLISION EFFICIENCY

#### *4.1 Introduction*

Calculating local collision efficiency is of prime importance in predicting the shape of the ice accretion, since the mass of supercooled droplets impinging on the surface of an iced body may easily be obtained using the formula  $WU\beta$ , where  $U$  and  $W$  are both constants. For a dry accretion, the amount of water impingement collected at any given position is proportional to its local collision efficiency.

As an *a priori* requirement, it is necessary to track the trajectories numerically for a number of droplets in accordance with the original definition of Local Collision Efficiency (LCE) as will be seen in Equation 4-13. This tracking procedure demands the greatest amount of computational time, as well as storage resources, compared to the time required for running any other elementary components in the model.

For a time-dependent ice model in particular, it is necessary to account for the feedback effect of changing ice geometry. It should be noted that the changes in ice geometry will result in the variation of such parameters as the airflow velocity field, the motion pattern of water droplets, and the LCE.

Thus, the ice model under discussion takes into account the feedback effect of changing geometry during cable icing, as well as the changed airflow velocity field. In particular, airflow is computed on the basis of the new geometry of the iced cable, and thereby the updated airflow velocity distributions are established. The equation of motion is solved so as to obtain the trajectories for a number of droplets. The feedback mechanism of the changing geometry of iced cables is accounted for by recording the occurrence of collisions of water droplets with the iced cable surface.

## ***4.2 Basic Principles***

In the proposed model, the motion of water droplets was modeled on the basis of the balance between the forces of air drag, gravity, and buoyancy. The Runge-Kutta algorithm was adopted here to solve the set of differential equations of motion for obtaining droplet trajectories. The local collision efficiency was then evaluated according to its definition. Lastly, a third order polynomial interpolation was performed to obtain the local collision efficiency at the relevant position. The air drag force was obtained and updated from airflow field computations during ice accretion simulations, considering that this force is predominant with regard to the other terms in the equation of motion for small droplets or drizzle.

### **4.2.1 Equations Governing the Motion of a Water Droplet**

A particular droplet in the vicinity of transmission line cables is liable, at any instant, to undergo electric-field effects. The nature and magnitude of the influence of such effects are dependent on the parameters of the cables as well as on the natural ambient

conditions. Farzaneh (2000) pointed out that several phenomena are associated with the influences of an electric field on droplets, thus making it inappropriate to conduct an analysis by singling out any given phenomenon from all the others. The force due to the electrical field,  $\vec{F}_e$ , is disregarded in the model presented here so as to avoid incurring greater complexity.

The forces considered in the equation of motion are the following:

- **Air Drag Force**

The air drag force acting on a water droplet may be expressed as the product of the drag coefficient,  $C_d$ , air density, frontal area of the droplet, and velocity difference between air and droplet, in the formulation:

$$\vec{F}_d = 1/2 \rho_a C_d A \left| \vec{V} - \vec{v} \right| (\vec{V} - \vec{v}) \quad (\text{E 4-1})$$

in which  $\vec{V}$  is derived from the airflow computation.

In the case of a low Reynolds number, it is preferable to evaluate the  $C_d$  together with the Reynolds number itself, according to the formulae, as described in the remaining part of this section.

- **Gravity**

The classical formula for gravity is used herein, as follows:

$$\vec{F}_g = \rho_e \vec{g} V \quad (\text{E 4-2})$$



- **Buoyancy Force**

Droplets immersed in the air are subjected to the buoyancy force induced by the pressure difference between their upper and lower surfaces. The definition for this force yields:

$$\vec{F}_v = \rho_a \vec{g} V \quad (\text{E 4-3})$$

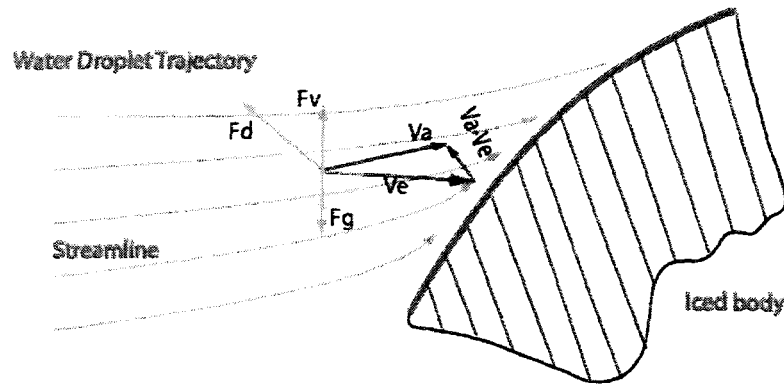


Figure 4.1 Forces experienced by droplet

Formulating these forces into the equation of motion, as shown in Figure 4.1, yields:

$$m \vec{a} = \vec{F}_d + \vec{F}_g + \vec{F}_v \quad (\text{E 4-5})$$

The dimensionless form of this equation reads:

$$k_i \frac{d\vec{v}}{dt} = k_d \left( \vec{V} - \vec{v} \right) + (k_g - k_v) \vec{g} \quad (\text{E 4-6})$$

where  $k_i = \frac{2R_a^2 \rho_e}{9\mu}$

$$k_d = \frac{C_d R_e}{24}$$

$$k_g = \frac{2R_a^2 \rho_e}{9\mu}$$

$$k_v = \frac{2R_a^2 \rho_a}{9\mu}$$

where  $\vec{v}$  is the droplet velocity,  $\vec{V}$  is the wind velocity,  $C_d$  is the drag coefficient of the droplet,  $D$  is the drop diameter, and  $\vec{g}$  is the acceleration of gravity.

In particular,  $k_d$  is evaluated by combining the formulae corresponding to the experimental studies carried out independently by Langmuir et al.(1946) and Beard et al. (1969), as follows:

$$\frac{C_d R_e}{24} = 1 + 0.189 \times \text{Re}^{0.632} \quad \text{for } 21 < \text{Re} \leq 200$$

$$\frac{C_d R_e}{24} = 1 + 0.115 \times \text{Re}^{0.802} \quad \text{for } 2 < \text{Re} \leq 21$$

$$\frac{C_d R_e}{24} = 1 + 0.102 \times \text{Re}^{0.955} \quad \text{for } 0.2 < \text{Re} \leq 2$$

and

$$\frac{C_d R_e}{24} = 1 + 0.197 \times \text{Re}^{0.63} + 2.6e-4 \times \text{Re}^{1.38} \quad \text{for the remaining Re numbers}$$

After taking components, Equation 4.6 can be reduced to a set of first-order ordinary differential equations as follows:

$$k_i \frac{dv_x}{dt} = k_d (V_x - v_x), \text{ for the } x\text{-axis,} \quad (\text{E 4-7})$$

$$k_i \frac{dv_y}{dt} = k_d (V_y - v_y) - (k_g - k_b)g, \text{ for the } y\text{-axis,} \quad (\text{E 4-8})$$

and

$$\frac{dx}{dt} = v_x$$

$$\frac{dy}{dt} = v_y$$

The signs in the equations may vary according to the definition of directions for both  $x$ - and  $y$ -axes.

#### 4.2.2 Solutions

The velocities  $v_x$  and  $v_y$  appear on both sides of the above differential equations thereby making them nonlinear. In view of the difficulties involved in finding a theoretical solution, seeking numerical solutions to them is recommended. It should be noted that these equations are a set of first-order differential formulae, to which the Runge-Kutta algorithm may conveniently be applied. Here, a four-variable Runge-Kutta algorithm was used to solve the equations numerically.

#### 4.2.3 Initial Conditions and Time Steps

Initially, water droplets were located on the upstream side of the object at a horizontal distance of  $5 \times D_{\text{cable}}$  as shown in Figure 4.3, where the gradient of the airflow velocity field is assumed to be 0. The initial velocity  $x$  components of water droplets may be expressed as  $v_x = V_0$  in which  $V_0$  is the onset free-stream speed.

$$v_y = 9.32 \times (1 - e^{-(MVD/1.77)^{1.147}}) \quad D > 300 \mu m ,$$

or

$$v_y = 0 \quad D < 300 \mu m$$

where the  $y$  component is the terminal droplet speed (Best, 1950).

The time step is carefully designed to meet the requirements of computational efficiency and accuracy. To initiate the calculation procedure, a larger time step is adopted to account for a minor velocity change. With droplets approaching the icing object, the time step is scaled down to compensate for a sharper velocity gradient. Also, the time step should be proportional to the diameter of the cable,  $D_{cable}$ , and inversely proportional to the onset air speed,  $V_{air}$ . In formula form, the factors may be expressed as follows:

$$\Delta T \propto D_{cable}/V_{air} \quad (E\ 4-12)$$

#### 4.2.4 Surface Collision

In order to obtain the LCE, it is necessary to detect the location of collision points accurately. These points are to be found at the intersection of the trajectories and the surface of the body.

Since the surface is divided into a number of linear elements, it may be regarded as a polygon. Thus, this problem may be converted in such a manner as to solve the intersections between the straight line T1-T2, and the polygon, as shown in Figure 4.2. T1 and T2 are the points on the trajectory corresponding to two sequential time steps.

The details of the procedure for determining the occurrence of collisions are provided below:

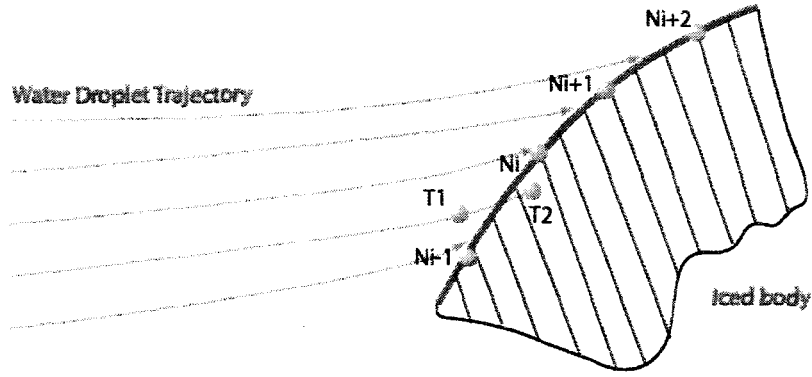


Figure 4.2 Collision points of water droplets

For any element, the coordinates for the intersection point read:

$$X_J = (Y_{Ni+1} - Y_{T2} - K_N \times X_{Ni+1} + K_T \times X_{T2}) / (K_T - K_N) \quad (E\ 4-13)$$

$$Y_J = Y_{T2} + K_T \times (X_J - X_{T2}) \quad (E\ 4-14)$$

where

$$K_T = (Y_{T2} - Y_{T1}) / (X_{T2} - X_{T1}) ;$$

$$K_N = (Y_{Ni+1} - Y_{Ni}) / (X_{Ni+1} - X_{Ni}) ;$$

$T1$  and  $T2$  represent droplet positions corresponding to two successive time steps; and

$Ni$  and  $Ni+1$  represent the two nodes of the surface element  $i$ .

The condition used to determine the occurrence of a surface collision is as follows:

$$(Y_J - Y_{T1}) \times (Y_J - Y_{T2}) < 0 \quad \text{and} \quad (Y_J - Y_{Ni}) \times (Y_J - Y_{Ni+1}) < 0 \quad (E\ 4-15)$$

If the condition above is satisfied, then the impact point lies between nodes  $Ni$  and  $Ni+1$ .

Otherwise, the above tracking procedure will continue until surface collision occurs or the droplet goes beyond the boundary of the calculation zone.

#### 4.2.5 Evaluating Local Collision Efficiency

The definition of the LCE yields:

$$\beta(\theta) = \frac{dY}{dL} \quad (\text{E 4-16})$$

where  $dY$  is the vertical distance between two trajectories in the onset flow, and  $dL$  is the distance between the impact points on the ice mass surface, as shown in Figure 4.3.

The value of  $dY$  varies with the number of droplets chosen for tracking the trajectories. Achieving the desired accuracy, requires the presence of a certain minimum number of droplets so as to produce an adequate number of trajectories for the calculation of the LCE. In the case under study, the trajectories of 200 droplets were implemented in one simulation.

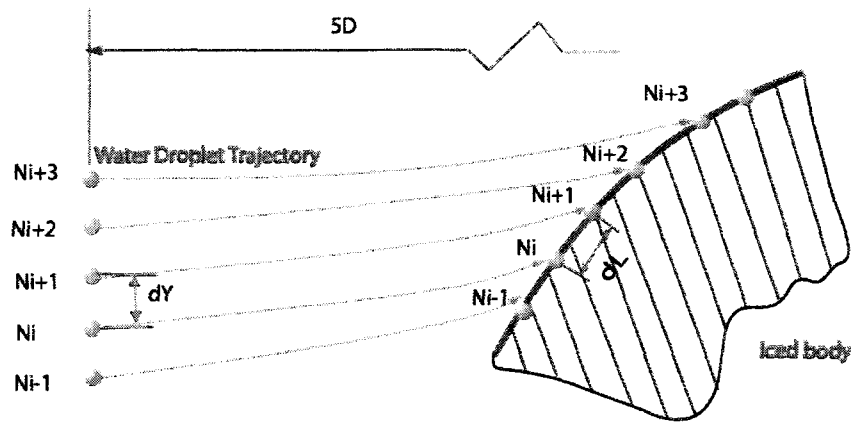


Figure 4.3 Definition of the local collision efficiency

Finally, a third-order polynomial interpolation was carried out to obtain the local collision efficiency at the relevant position.

During the simulation, the Median Volume Diameter (MVD) was used to represent a spectrum of droplets. The validity of this practice will be assessed in the next section.

### 4.3 Simulation and Validation of Results

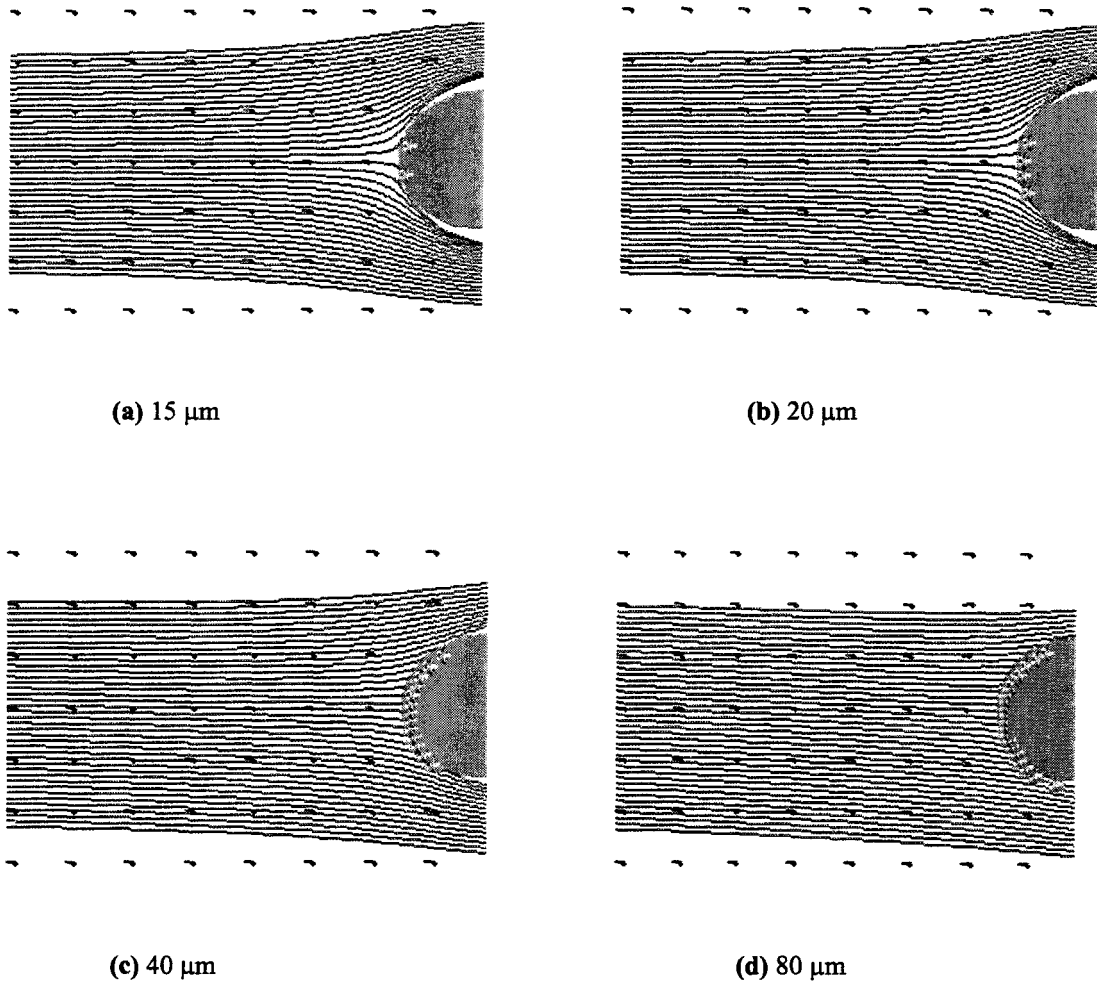


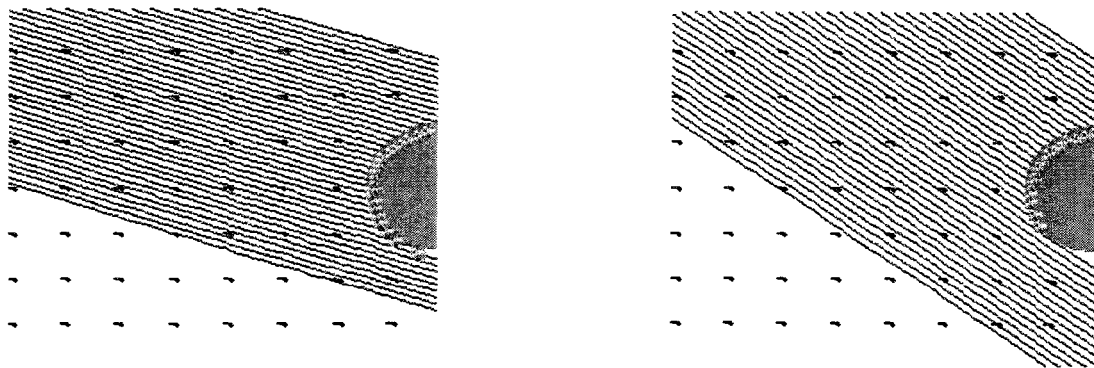
Figure 4.4 Trajectories for water droplets of different diameters.

Additional simulation conditions: cable diameter = 34.925 mm; wind speed = 5 m/s.

Figure 4.4 shows the droplet trajectories for droplet sizes ranging from 15  $\mu\text{m}$  to 80  $\mu\text{m}$ . It will be seen that gravity imposes no perceivable influence on the trajectories in the case of small droplets, but rather that the trajectory pattern is determined mainly by droplet inertia. From the figures, it may also be deduced that the larger the droplet, the



greater the LCE and maximum impingement angle. In the case of small droplets, gravity may be disregarded in the equation of motion. This conclusion, however, cannot be extended to include the case of freezing rain. Figure 4.5 shows trajectory simulations for droplets of 0.5 and 1 mm in diameter which are typical under conditions of freezing rain. It may be observed that the droplets being simulated travel in oblique straight lines and that the water flux is uniform in relation to the object. It is evident that the effect of air drag is negligible in comparison with the effects of gravity and inertia in such cases.



(a) 0.5 mm

(b) 1 mm

Fig 4.5 The influence of gravity on the trajectories of water droplets

Additional simulation conditions: droplet diameter = 1 mm;  
cable diameter = 34.925 mm;  
wind speed = 5m/s.

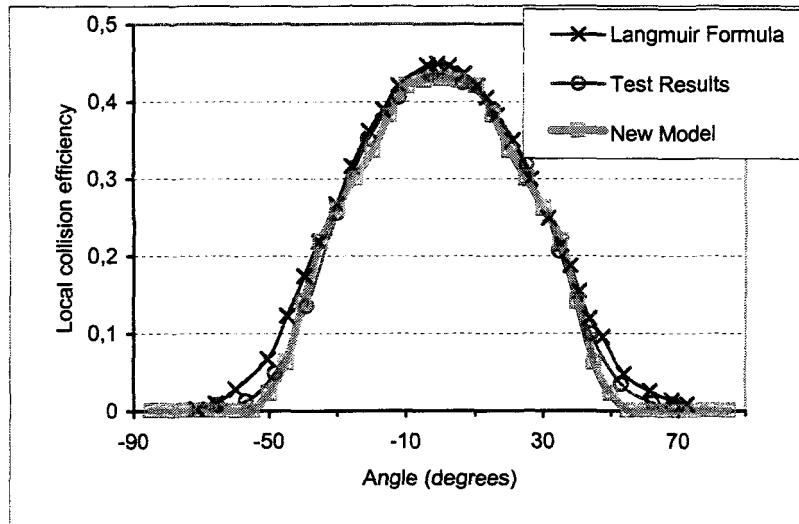
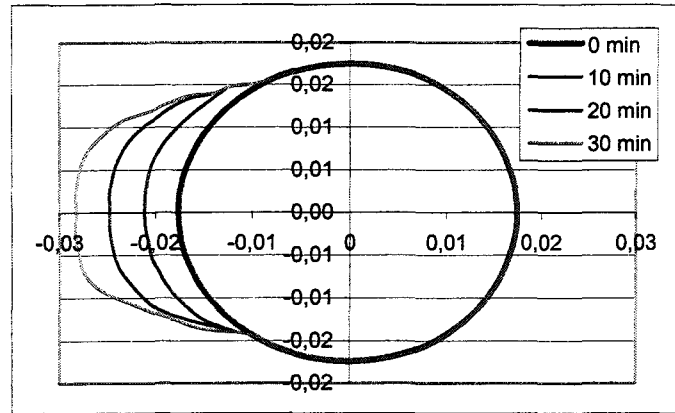
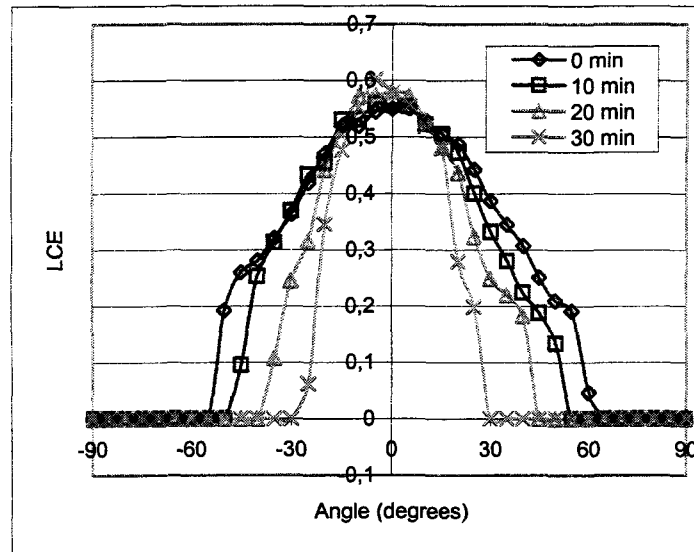


Figure 4.6 Comparisons based on both model simulations and Test Results.  
 Additional conditions: air speed 81.02 m/s; air temperature 8.2°C;  
 MVD 16.45  $\mu\text{m}$ ; pressure 95.65 kPa; diameter 10.16 cm.

Figure 4.6 is used to demonstrate the validity of the proposed procedure. The three curves plotted in Figure 4.6 represent the model simulations obtained from applying the method, together with the empirical Langmuir formula and the results of the experimental tests carried out at the Federal Aviation Agency (1991). On the whole, a comparison of the curves reveals that the simulation results of the proposed method are in satisfactory concordance with their experimental counterpart as well as with those of the Langmuir formula. The slight shape difference at the bottom of the curves may result from an inaccuracy in the numerical calculations which may be reduced to some degree by refining the surface mesh, that is to say, increasing the element number. Additional computation time and storage resources would be needed to implement such a refinement.



(a) Ice Shapes



(b) LCE

Figure 4.7 Time evolution of the Ice shape and LCE for an icing object

As described above, the shape change during the ice accretion process is taken into account in the proposed procedure. Figure 4.7 demonstrates how the LCE varies in response to the shape change of an ice-covered object. In particular, Figure 4.7(a) shows the time evolution of the ice shape, while Figure 4.7(b) displays the LCE distribution corresponding to each time step. It may be seen from Figure 4.7(b) that, as ice builds up

on the object, the LCE curve appears to be slimmer on either side in relation to the  $y$ -axis, while the peak of the curve shows no observable change. The maximum impingement angle also undergoes variation, that is to say, its value shifts from an initial  $60^\circ$  to  $30^\circ$  at the end of a 30-min simulation period. This implies that the object is no longer exposed to the water flux at the angular position between  $30^\circ$  and  $60^\circ$  as it was at the beginning of the simulation. These changes in the LCE may serve to explain why a time-dependent calculation yields a narrower ice shape than the one using a constant collection efficiency distribution, when observed from the direction which is perpendicular to the incoming airflow. It should be mentioned here, that it is still appropriate to use the constant LCE method for estimating ice-accretion thickness at the frontal edge of the object in the windward direction, since the LCE in this region (around  $0^\circ$  on the  $x$ -axis) undergoes no major change over time, as shown in Figure 4.7(b). This is further proof that it is worth while devoting a substantial amount of effort to this aspect of the model.

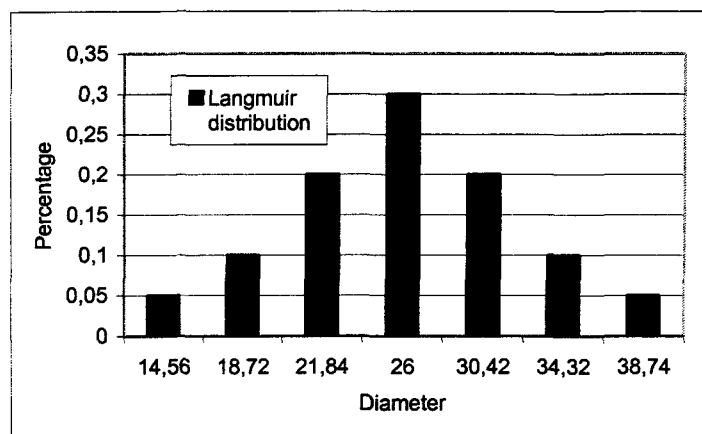


Figure 4.8 Langmuir volume distribution

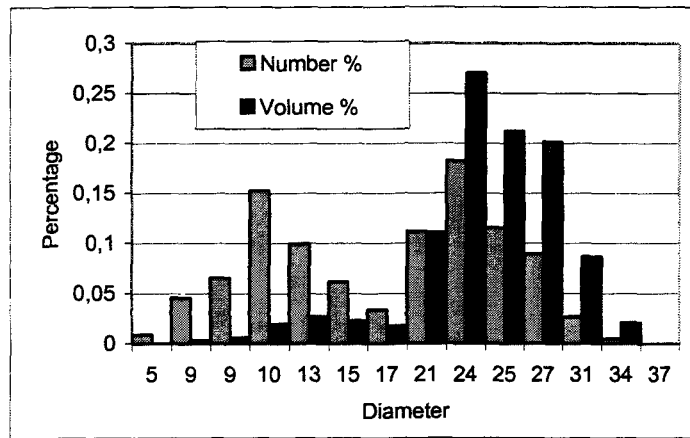


Figure 4.9 Droplet size and volume for bimodal case

In order to examine the influence of the Droplet Size Distribution (DSD) on the LCE, two droplet spectra with different diameter distributions were used in LCE calculations. The first spectrum has a bimodal distribution corresponding to certain natural conditions, and the second is assigned a Langmuir distribution which is most readily adopted by ice model researchers. The LCEs obtained for these two spectra were then compared to those of a monodisperse spectrum of the same Median Volume Diameter (MVD).

Figure 4.8 shows the Langmuir volume distribution (disperse-spectrum type B) with an MVD of 26  $\mu\text{m}$ . Figure 4.9 shows a typical bimodal droplet size distribution for in-cloud icing and its number percentage as indicated by the lighter-coloured Volume. Figure 4.10 shows the comparison of the cumulative volume distributions for both of the above cases; both have MVDs of 26  $\mu\text{m}$ .

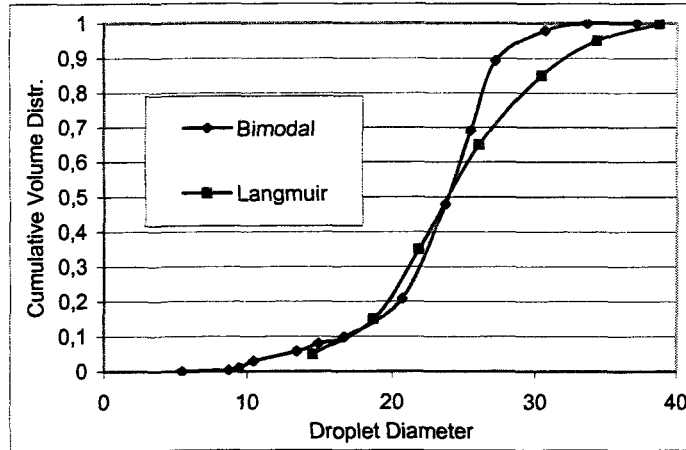


Figure 4.10 Cumulative volume distribution for both cases

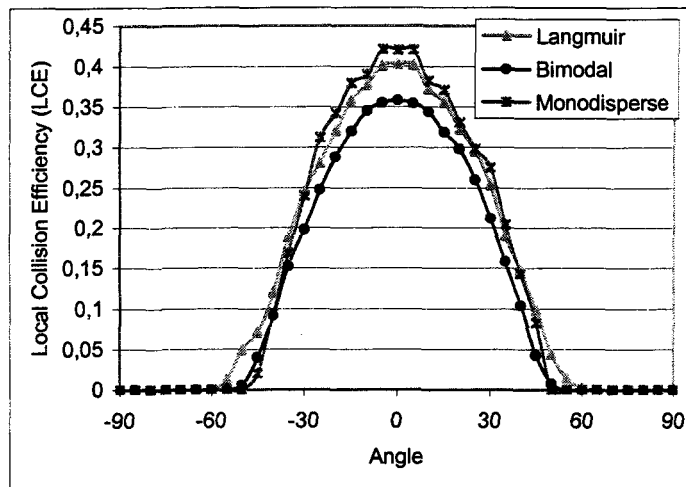


Figure 4.11 LCE distributions for three cases of different DSDs

The calculation results are demonstrated in Figure 4.11, from which it is clear that the LCE curve in the monodisperse droplet-size distribution is a good match for the Langmuir curve, despite the fact that it shows an obvious deviation from the curve in the bimodal distribution. According to the same figure, the peak value for the latter distribution reads 0.36, which is 10 percent less than that of the monodisperse case. Thus, these results may contribute to justifying the practice of using a batch of MVD droplets, in place of a spectrum of droplets, to obtain the LCE. Based on the reasoning provided

earlier, however, great care should be taken when extending such a method to cover a bimodal distribution.

#### ***4.4 CONCLUSIONS***

In this chapter, details of modeling the movement of a droplet in the vicinity of an icing object were provided. This procedure was then used as a tool to analyze the effect of the droplet size on the icing process. A number of conclusions may be drawn from the model simulations, including:

- The ice model described herein takes into account the feedback effect of the changing geometry during ice accretion, as well as the changed airflow velocity field.
- Compared to the commonly used Langmuir curve-fitting formulas, the proposed procedure displays a greater capacity for predicting complex ice shapes.
- The proposed calculation procedure, from its derivation, may be applied to a wide range of icing conditions, such as in-cloud icing, freezing fog, and freezing rain.

## CHAPTER 5

### THERMAL BALANCE AND SURFACE WATER FLOW

#### *5.1 Introduction*

The solution to the thermal balance equation is used for determining the icing fraction of the overall collected supercooled water on any given surface sector. This supercooled water may be collected either from the incoming water flux or from the unfrozen water on the adjacent sector. The local heat transfer coefficient is a key parameter in the thermal balance equation for ice accretion, since two of the principal terms in this equation, namely, the convective heat flux and the evaporative heat flux, are functions of this heat transfer coefficient, as described in the review of the literature.

Once the icing fraction is obtained for wet accumulations, the mass of unfrozen water may also be determined by subtracting the frozen portion from the total collected water. The unfrozen water tends to move over the surface under the combined action of gravity and air drag. Conventionally, the unfrozen portion is assumed to shift completely to the adjacent surface element during each simulation step. Hence, according to this assumption, no unfrozen water would remain on the ice-covered surface at the end of each calculation step. It appears, however, that this is not the case in reality.

In order to estimate the amount of water retained on the surface at the end of each simulation step, it is necessary to model the motion of the surface runback water. The surface water film will run back along the substrate surface under the action of such



external forces as gravity, air drag and surface tension. One part of the water film will move upwards while the remainder will run down. It is not necessary for the runback water to start its motion at the stagnation point, as has been assumed by a number of researchers. The starting point is defined as the location at which the effects of the external forces cancel each other out, and the water-flow undergoes a change in direction. Once the flow direction on any particular surface element is known, it is possible to establish the calculation sequence and determine the amount of water gained from the preceding element together with the amount discharged to the next one.

In this chapter, the method used to determine the local heat transfer coefficient will be discussed, and the calculation results obtained using this method will be compared with those of experimental tests in order to justify its applicability. The details of the thermal balance equation will be provided further on in the chapter, and a discussion on the modeling of the surface water film will also be included.

## ***5.2 Solution to Thermal Boundary Layer***

- The laminar boundary layer

For a body of arbitrary shape, Echert proposes an approximate solution to the differential equations of the laminar boundary layer (Kays and Crawford, 1993), as follows:

$$\Delta^2 = \frac{11.68\nu \int_0^x U^{1.87}(x)dx}{U^{2.87}(x)} \quad (\text{E 5-1})$$

where  $\Delta$  denotes the conduction thickness, and  $U$  is the local free stream velocity on the outer edge of the air boundary layer.

The local HTC may be obtained using  $h_x = K_f / \Delta$ , where  $K_f$  is the thermal conductivity of water.

- The turbulent boundary layer

The local HTC in the turbulent boundary layer may be evaluated in terms of the Stanton number which is a function of the Reynolds number based on enthalpy thickness, as follows:

$$St = 0.0287 Pr^{-0.4} \frac{R^{0.25} (t_0 - t_x)^{0.25} \mu^{0.2}}{\left[ \int_0^x R^{1.25} (t_0 - t_x)^{1.25} G_x dx \right]^{0.2}} \quad (E 5-2)$$

where  $t_0$  is the surface temperature;

$t_x$  is the temperature in the free stream at the outer edge of the boundary layer;

$Pr$  is 0.72 for the air;

$R$  is the transverse radius of curvature of the body; and

$G_x$  may be written in the formulation:  $G_x = \rho_x U_x$  in which  $\rho_x$  and  $U_x$  are the air density and the free-stream velocity, respectively, on the outer edge of the boundary layer.

Then, the local heat transfer coefficient in the turbulent boundary layer may be evaluated in terms of the Stanton number, as follows:

$$h_x = \rho C_p U_x St(x) \quad (\text{E } 5-3)$$

where  $\rho$  is the free-stream air density, and  $C_p$  is the specific heat of air at constant pressure.

The formulae described above may be applied to solve the thermal boundary layer for arbitrarily specified variations in free-stream velocity and surface temperature, both of which may be expressed entirely in terms of local variables.

- The wake region

For a given flow perpendicular to a cylinder, the Nusselt number in the wake region may be evaluated according to the approximate method proposed by Morgan (*in* Kays & Crawford, 1993), in which the Nusselt number is expressed as a function of the Reynolds number, as follows:

$$Nu = C_1 Re_d^{C_2} \quad (\text{E } 5-4)$$

where  $C_1$  and  $C_2$  may be evaluated according to the Reynolds numbers listed in Table 5.1.

Re	$C_1$	$C_2$
$10^{-4}$ - $4 \times 10^{-3}$	0.437	0.0895
$4 \times 10^{-3}$ - $9 \times 10^{-2}$	0.565	0.136
$9 \times 10^{-2}$ -1	0.800	0.280
1-35	0.795	0.384
$35$ - $5 \times 10^3$	0.583	0.471
$5 \times 10^3$ - $5 \times 10^4$	0.148	0.633
$5 \times 10^4$ - $2 \times 10^5$	0.0208	0.814

Table 5.1 Parameters  $C_1$  and  $C_2$  as functions of the Reynolds number

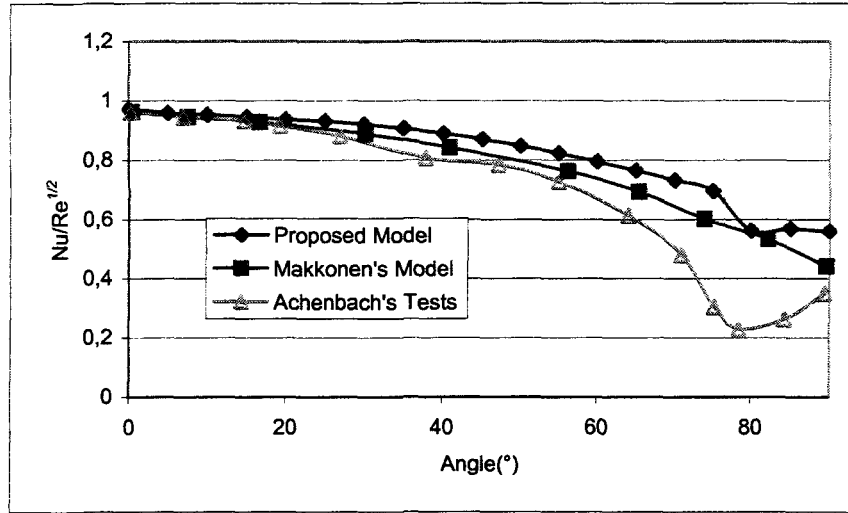


Figure 5.1 Comparison of local HTC's obtained from present simulation and those of earlier studies  
Additional conditions: air speed 8 m/s; cylinder diameter: 3.49 cm.

The local HTC, as obtained by solving the above approximate formulae, is compared with the results yielded by Makkonen's model (1984) and Achenbach's experimental study, as shown in Fig. 5.1. The y-axis represents the relative Nusselt number which is scaled with the Nusselt value at the stagnation position. The local HTC's on the upstream side of a cylindrical object will then be plotted against their local angular position,  $\theta$ , starting from the stagnation point, as shown in Figure 5.1. For  $\theta < 75^\circ$ , all three curves display the same trend: the HTC tends to decrease slowly with increasing angle. At about  $\theta = 75^\circ$ , the proposed model and Achenbach's tests both report a boundary layer separation characterized by a abrupt drop in the local HTC. In Makkonen's study, the boundary layer separation is disregarded, and the laminar boundary layer is thus to be found on the upstream side of the cylinder throughout. Based on a comparison of these three curves, it may be concluded that the local HTC distribution in the proposed

calculation procedure reflects the actual developing process of the flow boundary layer better than the one in Makkonen's model.

It should be pointed out that, in the case of cable icing, the Reynolds number is primarily of order  $10^4$  to  $10^5$ , which implies a sub-critical flow condition. Thus, it may be predicted that the windward side of the cable will present a laminar boundary layer upstream of the separation point, throughout.

### 5.3 Thermal Balance Equation and Joule Heating

Provided that the incoming supercooled water is treated as a continuum, details of the microphysics involved are usually disregarded at the time of formulating the thermal balance equation, as has already been indicated in the review of the literature. The quantitative formula, in terms of a balance of heat fluxes at the icing interface, may be written as follows:

$$Q_c + Q_e + Q_v + Q_k + Q_w + Q_f + Q_r = 0 \quad (\text{E 5-5})$$

where

$Q_c$  is the sensible heat flux between accretion and airflow by convection. In formula:  $-\pi \cdot h(T_s - T_a)$ .

$Q_e$  is the evaporative heat flux. In formula:  $h \left( \frac{\text{Pr}}{S_c} \right)^{0.63} \frac{\mathcal{E}_v}{pc_p} (e_a - e_s)$ ,

$Q_v$  is the heat flux due to aerodynamic heating. In formula:  $\pi.hr_vV^2/(2C_p)$ , in which  $V$  is local air speed, and  $r_v$  is the recovery factor for viscous heating.

$Q_k$  is the heat flux due to the conversion of droplet kinetic energy into heat. In formula:  $R_wV^2/2$ , where  $V$  is droplet terminal speed.

$Q_f$  is the latent heat flux to the accretion due to freezing of some, or all, of the directly impinging water, in formula:  $l_{fs}R_w n$ ; and  $l_{fs}R_s n$  for runback water.

$Q_w$  is the sensible heat flux between the liquid water and the underlying accretion. In formula:  $c_wR_w(T_a - T)$ , and  $c_wR_s(T_s - T)$  for runback water and the underlying accretion.

$Q_r$  is the sensible heat flux from Joule heating, the details of which will be provided later in this section.

Both of the cooling fluxes,  $Q_c$  and  $Q_e$ , are usually the most important heat sinks under a wide range of conditions, and they are also both functions of the HTC. The local HTC,  $h$ , may be obtained by following the calculation procedure described in the preceding section.

Since the object under consideration may also be an energized cable which carries an electric current, it is necessary to account for the heat flux, in particular from the resistive

or Joule heating in the heat-balance equations. The term corresponding to this portion of heat flux may be expressed in formulation as follows:

$$Q_r = I^2 R_c / (\pi D_c) \quad (\text{E 5-6})$$

where the rated current,  $I$ , may be calculated according to the following formula:

$$I = (\text{Economical Current Density}) \times (\text{Conductor Cross-sectional Area})$$

The conductor resistance,  $R_c$ , is a function of conductor temperature, and by referring to certain technical manuals, it is possible to obtain the resistances at both high and low temperatures,  $T_{high}$  and  $T_{low}$ , respectively. Consequently, the resistance at any particular temperature,  $T_c$ , may be obtained by using linear interpolation according to the following equation:

$$R(T_c) = \left[ \frac{R(T_{high}) - R(T_{low})}{T_{high} - T_{low}} \right] \times (T_c - T_{low}) + R(T_{low}) \quad (\text{E 5-7})$$

The example provided below is intended for comparing resistive heat flux with a number of other major heat fluxes, including convective heat flux, evaporative heat flux, and so forth. The diameter of the cable under consideration is 2.63 cm. Other parameters related to this type of cable are the rated current:  $I = 490 \text{ amp.}$  and the electric resistance:  $R_c = 8.14 \times 10^{-5} \text{ ohms/m} (0.131 \text{ ohms/mile}).$

The wind speed was set at 5m/s throughout the simulation. The heat fluxes obtained are shown in Figure 5.1 in which the magnitudes are represented by vertical bars. In total, five bars were displayed in the figure to represent convective heat flux; sublimate heat flux; dissipated heat flux from the warming-up of newly-collected water; latent heat flux; and resistive heat flux. It will be observed that the resistive heat flux is comparable to

convective heat flux and sublimation heat flux in terms of their values. The resistive heat flux tends to warm the ice mass, while the latter two tend to cause its temperature to drop. In the chapter on model simulations, further details will be provided with respect to the effect of Joule heating caused by an electric current. It should be noted that, for a totally ice-covered cylinder, the above-mentioned method may be applied without risk of substantial error, whereas for a partially ice-covered cylinder, this method may cause a higher degree of inaccuracy when evaluating the effect of Joule heating, since the resistive heat flux under such a condition tends to show a great irregularity on the surface of the icing cylinder.

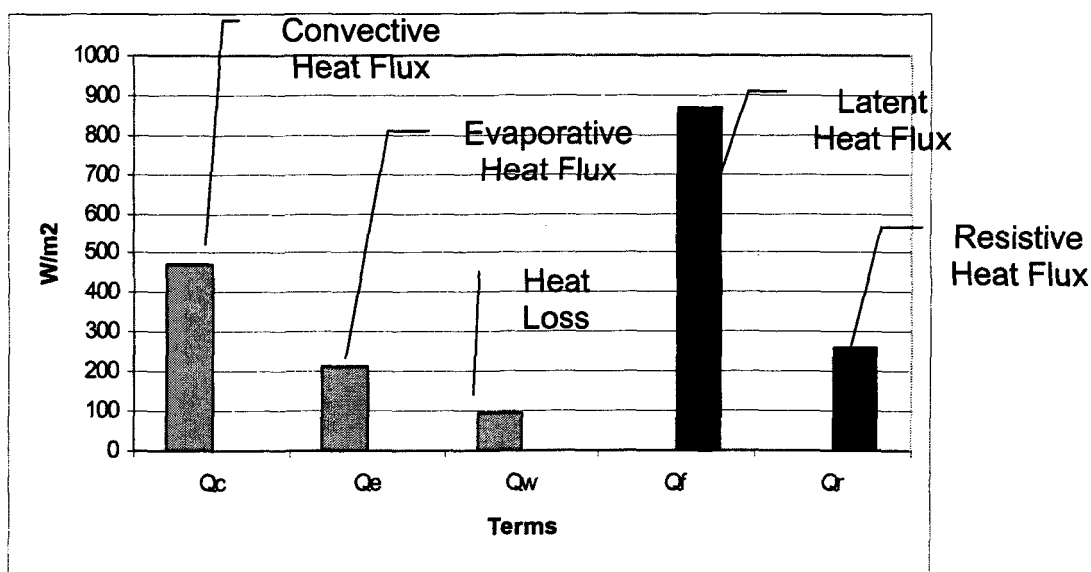


Figure 5.2 Magnitude analysis for heat fluxes in the heat balance equation

#### 5.4 Modelling the Flow of a Water Film

A number of assumptions were made in order to pursue the current research on modelling the flow of a water film on the surface of an icing object, as follows:

1. The runback water is invariably treated as a thin water film.



2. The water film on each surface element is so thin, when compared to the dimension of the individual element, that it is possible to regard it as a laminar flow over a flat plate.
3. A steady flow is assumed for the runback water, and the thickness of the water film is assumed to undergo no sudden change between two consecutive time steps.

#### 5.4.1 Separation Point of the Water Film

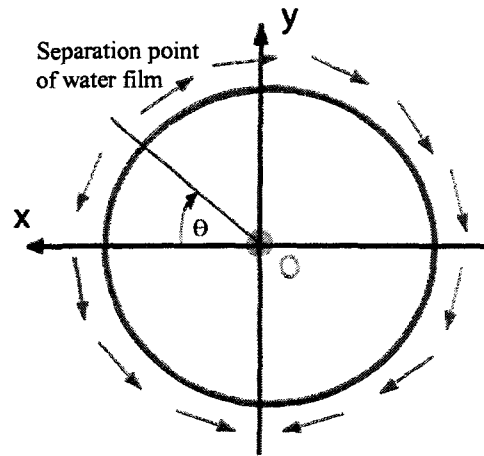


Figure 5.3 Diagram for water-flow direction

The separation point under discussion is described as the starting point of the water film by Karev et al. (2004). The concept of a separation point may have wider application since, in the case of a high Reynolds number, the water film on the surface of a cylinder may present two streams which flow in two opposite directions, as shown in Figure 5.3. In such a case, the starting point is also the water-film separation point. There are two calculation loops for mass conservation and thermal balance equations in the proposed ice code. Both calculation loops start from the separation point, and one proceeds clockwise while the other moves counter-clockwise, sector by sector, as indicated by the



Of all the forces acting on the water film, only air drag and gravity affect its flow direction. In Figure 5.4, it will be observed that points of action for gravity and air drag force do not coincide, thereby complicating the task of comparing the effects of these two forces. Nevertheless, it is possible to compare the average flow velocities induced by gravity  $V_g$  and air drag force  $V_t$ , independently of each other.

$$V_g = \frac{1}{3} \frac{\gamma}{\mu} d^2 \sin \theta \quad (\text{E 5-7})$$

$$V_t = \frac{\tau_{air}}{\mu} \frac{d}{2} \quad (\text{E 5-8})$$

If  $V_t - V_g > 0$ , then the water film moves upwards; otherwise, it flows downwards. Details for developing Eq. 5-7 and Eq. 5-8 will be provided in the remaining part of this chapter.

### 5.4.3 Mass Conservation of the Water Film

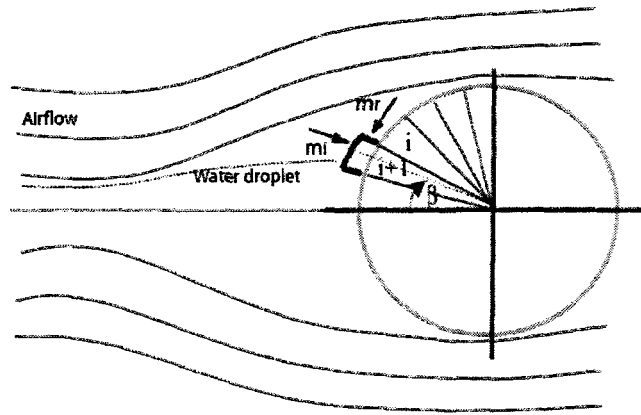


Figure 5.5 Diagram for the mass conservation of a water film.

For a specific element, the water is collected from water impingement,  $m_i$ , and the unfrozen water,  $m_r$ , from the preceding element, as shown in Figure 5.5 where the water film is observed to move from  $i$  to  $i+1$ . The flow direction of water may also move from  $i$  to  $i+1$  when air drag is predominant in relation to gravity.

Once the thickness of the water film is known, it is possible to estimate the flow speed according to the following formula:

$$\text{Speed of water flow} = \frac{\text{Total water discharge}}{\text{Water film thickness}} \quad (\text{E 5-8})$$


---

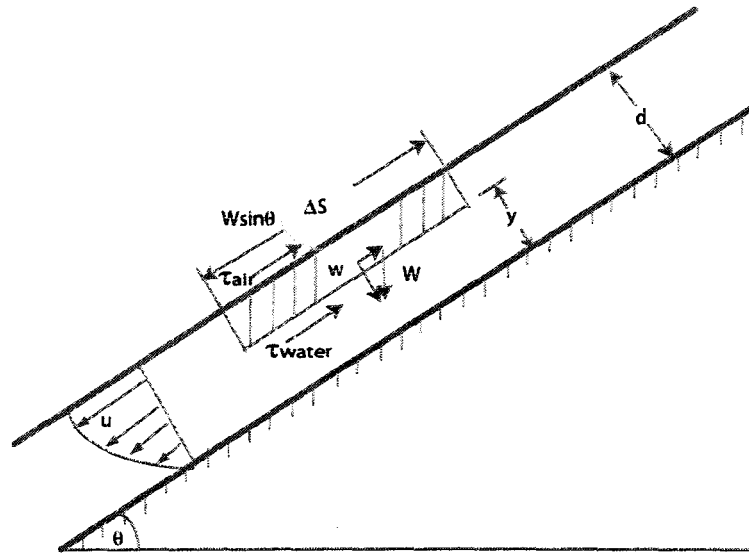


Figure 5.6 Inclined flow between a fixed plate and moving plate

The water film may be regarded as a flow between a fixed plate and moving plate, as shown in Figure 5.6. These plates are inclined at an angle  $\theta$  with regard to the horizontal plane. It is possible to apply the momentum equation to an element of fluid, the top of which is the liquid surface. The element has a unit width normal to the page. The pressure is hydrostatic across any section normal to the plane, as a uniform distribution is assumed. Also, the depth is constant, so that the pressure forces of the end sections of the element will cancel each other out. Therefore, the momentum equation reduces to:

$$\tau \Delta s + \tau_{air} \Delta s - W \sin \theta = 0 \quad (E 5-9)$$

$$\text{consequently, } \tau \Delta s + \tau_{air} \Delta s - \gamma(d - y) \Delta s \sin \theta = 0 \quad (E 5-10)$$

$$\text{leading to } \tau = \gamma(d - y) \sin \theta - \tau_{air} \quad (E 5-11)$$

Here, the Reynolds number is based upon the depth of the flow. With a thin water film, the Re number is small enough to develop a laminar flow. It is possible to substitute  $\mu \frac{du}{dy}$  for  $\tau$  and then solve the equation for the velocity distribution, as follows:

$$\mu \frac{du}{dy} = \gamma(d - y) \sin \theta - \tau_{air} \quad (E 5-12)$$

Upon integrating, the above equation becomes

$$u = -\gamma(d - y)^2 \sin \theta / (2\mu) - \tau_{air} y / \mu + C \quad (E 5-13)$$

To evaluate the constant of integration, we observe that  $u=0$  when  $y=0$ ; therefore,

$$C = \frac{\gamma}{\mu} \frac{d^2}{2} \sin \theta \quad (E 5-14)$$

The velocity distribution is then given by

$$u = -\gamma(y - 2d)y \sin \theta / (2\mu) - \tau_{air} y / \mu \quad (E 5-15)$$

the discharge per unit width is now obtained by integrating the velocity,  $u$ , over the depth of the flow.

$$q = \int_0^d u dy = \frac{1}{3} \frac{\gamma}{\mu} d^3 \sin \theta - \int_0^d \tau_{air} y / \mu dy = \frac{1}{3} \frac{\gamma}{\mu} d^3 \sin \theta - \frac{\tau_{air}}{\mu} \frac{d^2}{2} \quad (E 5-16)$$

The average velocity is now obtained by dividing the above equation by the cross-sectional area  $d$ ,

$$V = \frac{q}{d} = \frac{1}{3} \frac{\gamma}{\mu} d^2 \sin \theta - \frac{\tau_{air}}{\mu} \frac{d}{2} \quad (E 5-17)$$

It should be observed that the average velocity is derived from the superposition of two terms, i.e. the velocity induced by gravity and the velocity induced by air shear stress. Such a notion may serve to establish the separation points on the surface water film, as described in an earlier section. It should be pointed out, in particular, that the above equation holds only for the water film in zone 1, where the water film flows downwards, as shown in Figure 5.6. A change of sign should be made when the equation is intended to apply to the water film anywhere else on the surface.

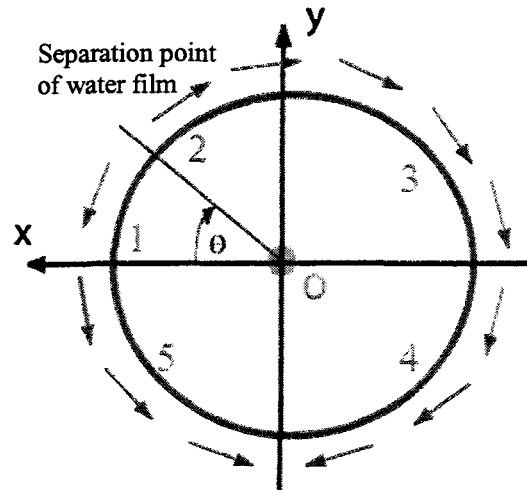


Figure 5.7 Diagram of the division of surface zones.

As indicated in Figure 5.7, the water film on the substrate can be divided into 5 zones numbered from 1 to 5. There is a separate formula which applies to each of these zones, as shown in Table 2.

Number	Formulae
1	$q = \frac{1}{3} \frac{\gamma}{\mu} d^3 \cos \theta - \frac{\tau_{air}}{\mu} \frac{d^2}{2}$
2	$q = -\frac{1}{3} \frac{\gamma}{\mu} d^3 \cos \theta + \frac{\tau_{air}}{\mu} \frac{d^2}{2}$
3	$q = \frac{1}{3} \frac{\gamma}{\mu} d^3 \cos \theta + \frac{\tau_{air}}{\mu} \frac{d^2}{2}$
4	$q = \frac{1}{3} \frac{\gamma}{\mu} d^3 \cos \theta - \frac{\tau_{air}}{\mu} \frac{d^2}{2}$
5	$q = \frac{1}{3} \frac{\gamma}{\mu} d^3 \cos \theta + \frac{\tau_{air}}{\mu} \frac{d^2}{2}$

Table 5.2 Formulae corresponding to surface zones.

In the above equations,  $q$  is a known value and is numerically equal to the sum of impinging water and runback water from the adjacent element. The air shear stress,  $\tau_{air}$ , is obtained from airflow velocity field calculations within the same ice code. It appears that  $d$  is the only unknown variable in this non-linear equation, thus the Newton-Raphson iterative algorithm was used to solve this equation numerically.

Zero was taken as the initial estimate for the thickness of the water film so as to start the iteration calculation process. In the subsequent time step, its value was obtained from the preceding time step calculation.

#### 5.4.4 Calculation Procedure

1. Determine the boundary separation point on the basis of the water-film thickness from the preceding time step.
2. Obtain the mass flow rate based on the mass conservation law;
3. Solve E 5-16 to obtain the depth of the water film;
4. Solve E 5-17 to obtain the flow speed.

#### 5.5 Water-Film Calculation and Interpretation of Results

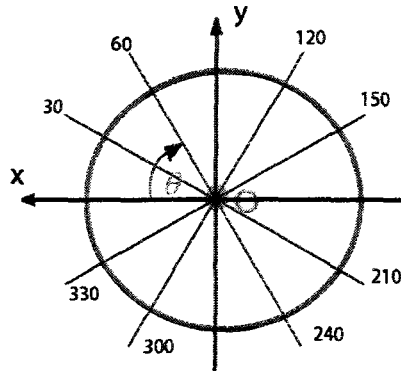
Model Input Parameters					
No.	Air Speed(m/s)	Temperature(°C)	MVD( $\mu\text{m}$ )	Diameter(mm)	LWC( $\text{g/m}^3$ )
1	10	-5	26	34.9	2.5
2	5	-5	26	34.9	2.5
3	5	-5	26	34.9	5.0
4	15	-5	35	34.9	2.5

Table 5.3 Conditions applied in water-film calculations

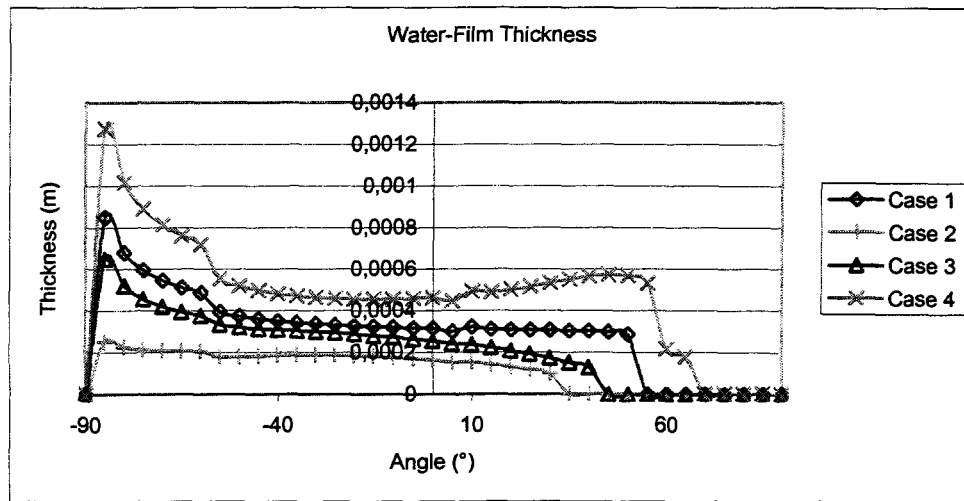
Four cases were studied using the calculation procedure described above. The cylinder under consideration in each case is 34.9 mm in diameter, and the detailed simulation conditions for each specific case are listed in Table 5.3. A comparison between each of the cases was implemented by varying one or two of the parameters at a time, such as wind speed, LWC or MVD. After calculation, the water-film and speed distributions on the upstream surface were obtained and illustrated by the curves, as shown in Figure 5.8



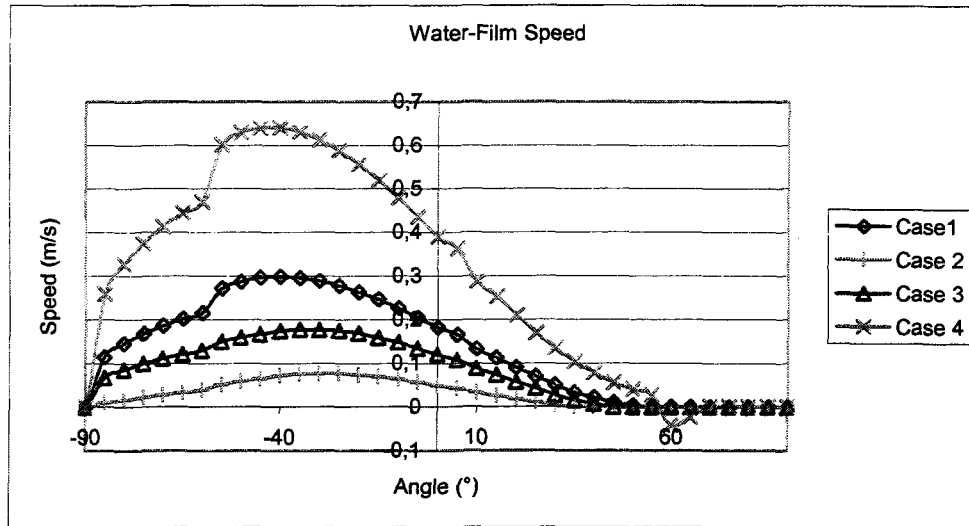
The curves for water-film thickness in Cases 1, 2, and 3, in Figure 5.8(b), display the same trend, i.e. the water-film thickness increases from an upper to a lower position upstream of the cylinder. This trend is characterized by the ever-rising curves which represent the water-film thickness, and may be explained by the fact that the angular position of the water-film separation point coincides with the highest position of the water film in all three cases, where the water film invariably flows downwards. As a result, the sector on the lower side tends to present more water on its surface than the preceding one, since the subsequent sector receives the unfrozen water from the adjacent area as well as incoming water impingements. Figure 5.8( c ) reveals that the speed of the water-film flow tends to accelerate with a decrease in the angle  $\theta$ . An exception to this trend is seen in Case 4 which presents an increase in both the wind speed and LWC compared to the preceding three cases. In contrast with the first three cases, Case 4 undergoes an initial abrupt increase in water-film thickness, then a slight drop and lastly a rise again, moving from the upper to the lower half of the cylinder. A sluggish growth in thickness may be observed at the angular position of about  $65^\circ$ , while a change in flow direction may be detected at the same position in Figure 5.8( c ), which may taken as an indication that the water-film separation occurs at this point. The occurrence of water-film separation may cause a change in the distribution of the water-film thickness, as shown in Figure 5.8( b ). It may also be concluded from these curves, that water-film thickness is an essential factor in determining the speed of the surface water-film flow, and that the thicker the water film, the faster its flow speed is.



( a ) Definition of angular position on cylinder surface.



( b ) Distribution of the water-film thickness on the upstream side



( c ) Distribution of the water-film flow speed on the upstream side

Figure 5.8 Water-film thickness and speed on the surface of a cylinder

## 5.6 Conclusion

In this chapter, a description was provided for the method used to determine the local heat transfer coefficient, and the results thus obtained were then compared with related experimental data so as to confirm its validity. Next, the modelling process for the flow of a water film was discussed in detail. Finally, this procedure was used to investigate four cases representing typical icing conditions, thereby revealing the thickness and speed distributions under these conditions.

## **CHAPTER 6**

### **EXPERIMENTS AND MODEL VALIDATION**

An array of experimental tests was carried out in the CIGELE Atmospheric Icing Research Wind Tunnel (CAIRWT) in order to validate the ice model discussed and developed in the preceding chapters. The instruments in the wind tunnel should be adjusted meticulously so that the conditions set for experimental tests are closely representative of those observed under natural conditions. The experimental conditions will later be used as input parameters for model simulations.

This chapter will provide an overview of the experimental set-up and the instruments involved in the tests. Further details will contribute to clarifying the method employed to calibrate the instruments used for creating the requisite test conditions. The latter conditions were designed to duplicate the icing process from dry to wet accumulations, and a specific consideration of variations in cylinder diameter was also included. The ice shapes thus obtained will be compared with those from model simulations, and will subsequently be discussed further on in the chapter.

#### ***6.1 Experimental Set-up and Instruments***

The CIGELE Atmospheric Icing Research Wind Tunnel (CAIRWT) is located in the CIGELE icing research pavilion which was built in 1998. It is a closed-loop atmospheric

icing tunnel capable of duplicating icing conditions as they occur in nature on transmission line cables.

The CAIRWT may be divided according to function into a number of subsystems or component elements, including the tunnel circuit, tunnel test section, air drive and speed control system, and a spray-bar device.

- **Tunnel Circuit**

The tunnel circuit in the CAIRWT is an air passage consisting of a number of connected segments, and these segments are of different shapes and cross-sections forming a closed circuit for air circulation, as shown in Figure 6.1. The total length of this circuit is about 30 m. Air in the wind tunnel is driven by a 45 kW motor whose frequency may vary from 0 to 60 Hz. This feature makes it possible for the wind speed in the tunnel to attain speeds of up to 30 m/s.

In addition, the CAIGELE Atmospheric Research Icing Wind Tunnel is equipped with a refrigerating system, which allows the air temperature in the channel to drop as low as  $-30^{\circ}\text{C}$ . In this system, ammonia ( $\text{NH}_3$ ) is used as the coolant for dissipating heat and attaining a drop in air temperature.

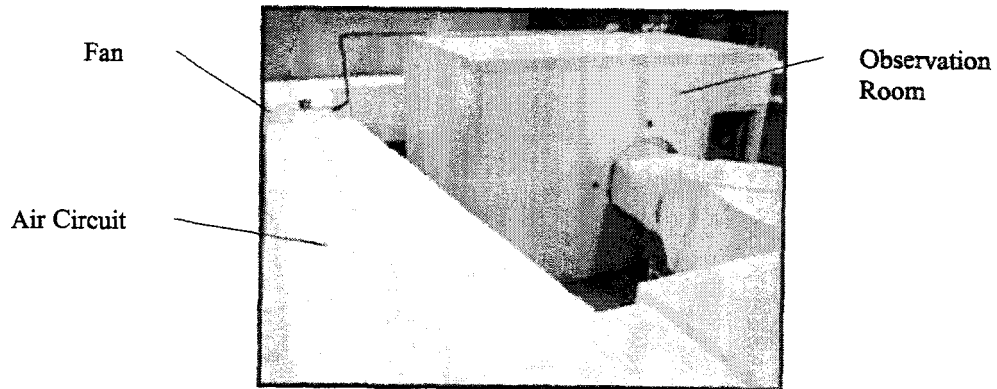


Figure 6.1 A top view of the CIGELE icing research wind tunnel

- Test Section

One segment of the air circuit is for the use of the test section which measures  $0.9 \text{ m} \times 0.45 \text{ m} \times 3.05 \text{ m}$  (width  $\times$  height  $\times$  length). A test model can be mounted inside this section, as shown in Figure 6.2. The walls of the test section are made of transparent Plexiglas through which ice accumulation processes occurring on the test model may be monitored. The entire test section is housed in a control room measuring  $3.5 \text{ m}$  long  $\times$   $4.5 \text{ m}$  wide  $\times$   $3 \text{ m}$  high.

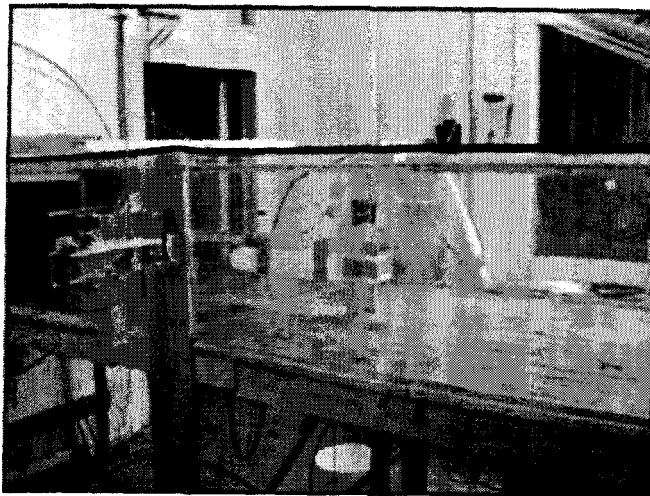


Figure 6.2 Test section of the CIRWT

- Air Drive and Speed Control System

As described above, airflow in the wind tunnel is generated by a 45 kW motor, and airspeed may attain speeds of up to 30 m/s when the motor is functioning at full capacity.

A Pitot-static probe positioned at the mid-point of the test section is used to measure the total and static pressure. Once the data is obtained, it is transferred to a Data-Acquisition system via a precise differential pressure transducer (Omega, USA), where the test-section free-stream velocity is computed and recorded. At the start of the test program, an aerodynamic test is run in order to establish a relationship between the test airspeed and the fan speed in revolutions per minute (Mousavi, 2003), as shown in Figure 6.3. This relationship is used to select a fan speed which will achieve the desired test airspeed.

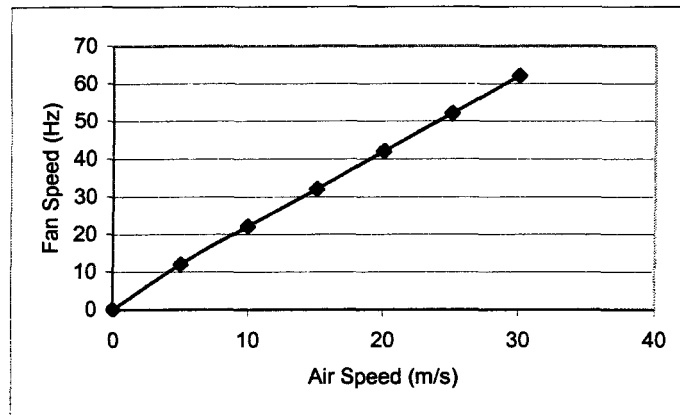


Figure 6.3 Relationship between air and fan speed

- Spray Bar

The spray bar, as shown in Figure 6.4, is located at the inlet of the test section, at a distance of 4.4 m from the middle of the test section where the test cylinder is mounted.

The spray bar is equipped with three air-atomization water spray nozzles at the trailing edge which are used to produce the appropriate sized droplets for the test program.

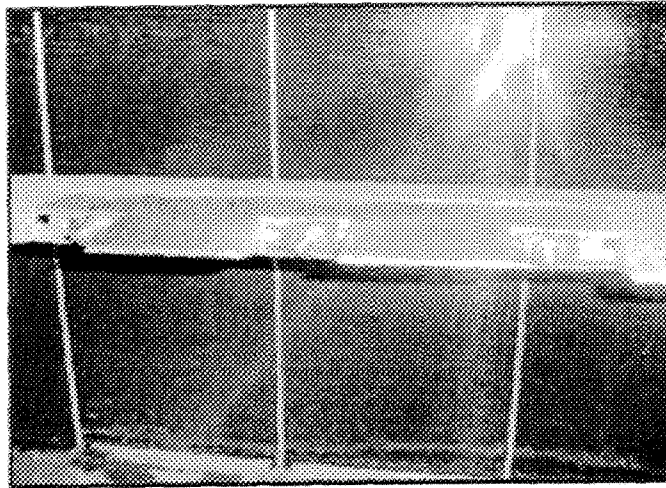


Figure 6.4 Spray bar fitted with three nozzles

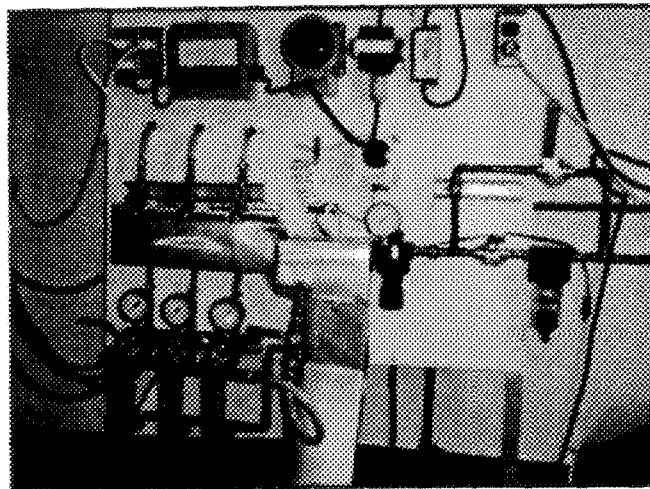


Figure 6.5 Control panel for air and water pressures and water flow rate

The three nozzles on the spray bar are supplied with water and air through three separate water and air supply lines. The air and water pressures, and the flow rate may be adjusted through the valves or meters on a control panel, as shown in Figure 6.5. A



desired Droplet-Size Distribution (DSD) at the mid-point of the test cylinder may be obtained through controlling the water flow rate, and the water and air pressures, among other parameters (Karev et al., 2002).

The existing experimental set-up in the CAIRWT provides facility in setting the values for most of the major parameters, including air speed and air temperature. Other parameters such as the Liquid Water Content (LWC) and the Median Volume Diameter (MVD), however, cannot be accurately estimated until a specific test is under way. These parameters may be divided into two groups on the basis of the means applied to determine their values, as shown in Table 6.1. The parameters in the first group may be set with ease simply by adjusting the controls or valves, while for those appearing in the second group, the values can only be accurately determined by measurement. The measuring process proved overly time-consuming, thus substantiating the merits of modelling and simulating the ice accretion process numerically.

<b>Group no.</b>	<b>Parameters</b>
1 (to be set)	Wind Speed, Air Temperature, Diameter of test cylinder, Pressures for both water and air pipelines, Type of nozzle
2 (to be measured)	LWC, Droplet Size Distribution (or MVD)

Table 6.1 Experimental parameters

## 6.2 Measuring the LWC and MVD

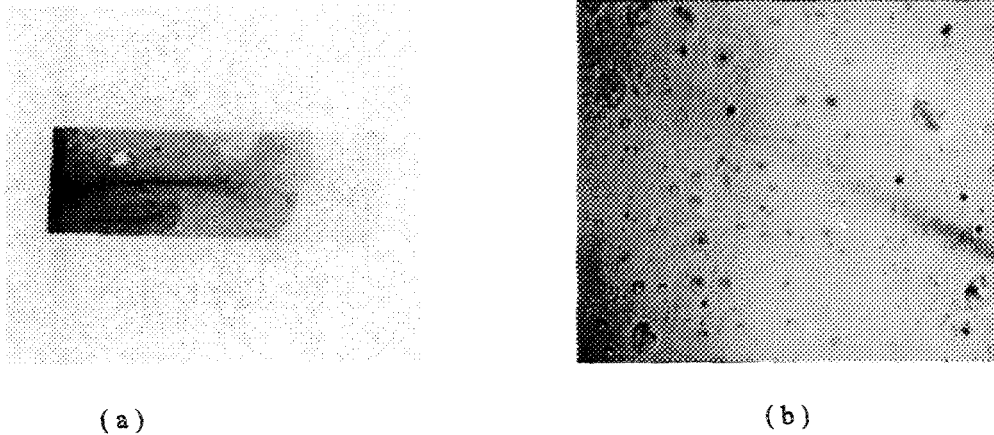


Figure 6.6 (a) Collargol coated slide  
(b) Traces of water droplets under a microscope

Measuring the Droplet Size Distribution (DSD) or MVD in the test section tends to be a time-consuming procedure. The DSD is especially volatile and dependent to a high degree on both experimental conditions and the type of instruments adopted. A slight change in any of these may result in a permutation of the pattern obtained. A number of relevant studies (Ide et al., 1990) concerning DSD in the wind tunnel reveal that, for any given nozzle, this parameter is a function of the pressures in both the water and air pipelines. The relationship between the DSD and other parameters may be represented by a group of curves. It should also be noted that wind speed is an additional factor causing changes in the DSD.

In the test program under discussion, only the LWC and MVD at the centre of the test section will be measured. The MVD is measured using the collargol coated slide method, in which the true droplet size is determined directly under a microscope, while the LWC

may be measured using a commonly-used method whereby a small cylinder together with its support is installed in the test section. The location of this small cylinder should be coincident with the centre of the test model, while a motor attached to one end of this small cylinder sets it rotating slowly and evenly. The ice on the cylinder is then collected and placed on a scale for weighing at the end of 1 or 2 minutes of collection time. Subsequently, it becomes possible to evaluate the LWC using a mathematical formula introduced by Stallabrass (1978) based on the ice-load data. It may be seen from this formula that the LWC is a function of the ice load and MVD. Also, a number of further tests should be carried out in order to determine the relationship between MVD, LWC and air speed.

In order to obtain DSDs and LWCs which reflect natural icing conditions more closely, the water and air pipelines were set at low values. In particular, the pressure in the air pipeline was set at  $6.9 \times 10^4 \text{ Pa}$  and  $1.38 \times 10^5 \text{ Pa}$  while, at the same time, the pressure difference was deliberately maintained at  $2.07 \times 10^5 \text{ Pa}$ . Accordingly, the pressures in the water pipeline were  $2.76 \times 10^5 \text{ Pa}$  and  $3.45 \times 10^5 \text{ Pa}$ . Also, the water flow rate was maintained at a low level of about  $100 \text{ cm}^3/\text{min}$  or  $200 \text{ cm}^3/\text{min}$ . At the outset of the test program, a number of tests were carried out in order to determine the tendency displayed by the curve for MVD plotted against air speed.

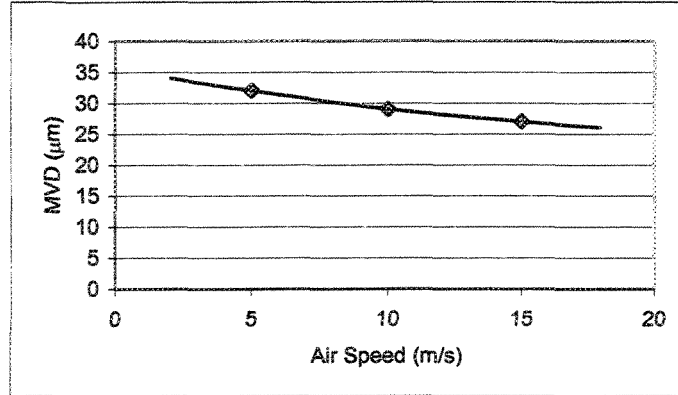


Figure 6.7 Relationship between MVD and air speed under experimental conditions

Additional conditions:  $P_{air} = 10 \text{ psi}$ ;  $P_{water} = 40 \text{ psi}$ ; water flow rate =  $100 \text{ cm}^3/\text{min}$ .

Figure 6.7 reveals that MVD values display a slight drop with increasing air speeds, while Figure 6.8 shows that the LWC increases at an accelerating rate with greater air speeds. It should be noted that during these tests other conditions remains constant. The trends displayed by these curves may serve to establish an optimal combination of test conditions.

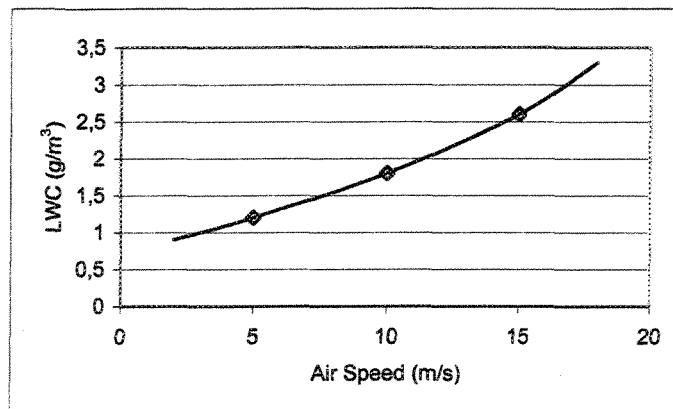


Figure 6.8 Relationship between LWC and air speed under experimental conditions

Additional conditions:  $P_{air} = 10 \text{ psi}$ ;  $P_{water} = 40 \text{ psi}$ ; water flow rate =  $100 \text{ cm}^3/\text{min}$ .

### 6.3 Acquiring Ice Shape Data

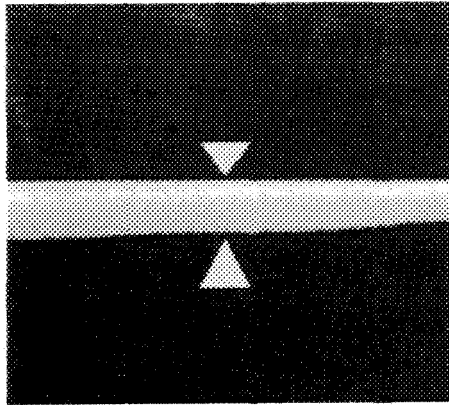
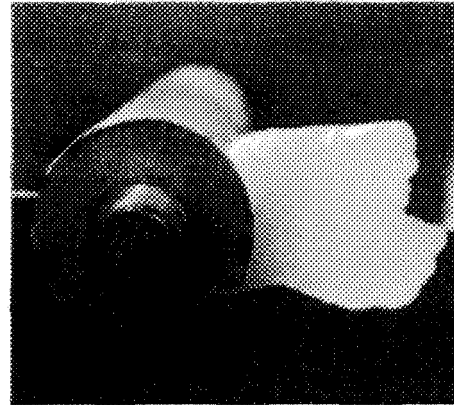


Figure 6.9 ( a ) An iced cylinder



( b ) Cross-sectional ice shape at midpoint of same cylinder

At the end of each test, the ice accretion covering the cylindrical model is cut into two at the midpoint using a heated metal plate, thereby obtaining a cross-sectional ice shape, as shown in Figure 6.9 (b).

### 6.4 Comparison of Ice Shapes from Model Simulation and Experiments

Here, five cases were considered in order to make a comparison of ice shapes between test results and model simulations. Cases 1 and 2 were designed to simulate a dry accumulation for a thin cable (19.05mm) and a thick cable (34.9mm), respectively. Cases 3 and 4 were intended to simulate a semi-wet and wet accumulation, respectively, on a cable of the same diameter as the one in Case 2, while Case 5 was used to demonstrate the wet-icing process on a cable of 19.05 mm in diameter. Detailed parameters are listed in Table 6.2. All the tests and model simulations, as described herein, were limited to a duration of 30 minutes each.

Case No.	Model Input Parameters				
	Air Speed(m/s)	Temperature(°C)	MVD( $\mu\text{m}$ )	Diameter(mm)	LWC( $\text{g/m}^3$ )
1	5	-15	34	19.05	1.2
2	5	-15	35	34.9	1.2
3	10	-10	28	34.9	1.8
4	10	-5	26	34.9	1.8
5	5	-5	33	19.05	1.2

Table 6.2 Parameters used for model validations

The ice shapes obtained from both the model simulation and experimental measurements in Case 1, are illustrated on the left- and right-hand sides of Figure 6.10, respectively. By comparing the ice shapes predicted by the model with those from experimental measurements, it will be observed that the proposed ice model correctly predicts the tendency of the ice accretion. The ice tends to grow outward axially with an ice shape which is broad perpendicular to the wind, while the ice mass tends to display a flat frontal edge. Also, the new model accurately predicts the thickness of the ice accretion on the cylinder surface, and the maximum impingement angle characterized by the ice-covered area appearing on the cylinder surface.

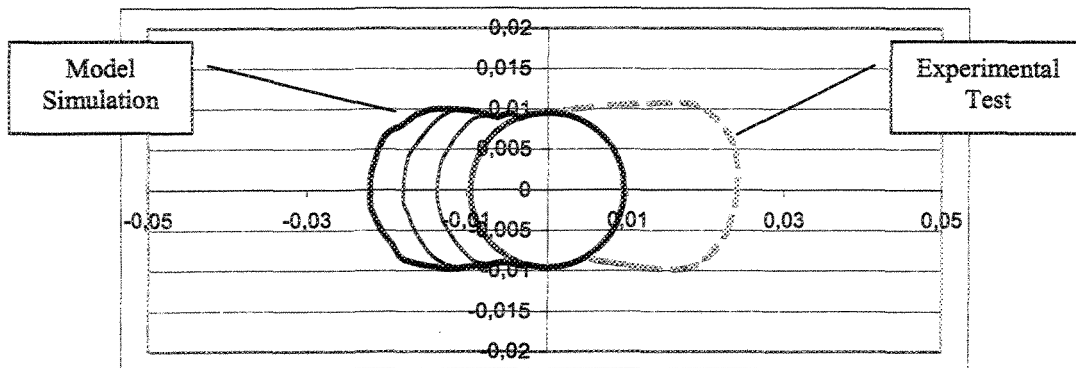


Figure 6.10 Comparison of ice shape - Case 1

Conditions: Air Speed 5 m/s, Air Temperature  $-15^{\circ}\text{C}$ ,  
MVD  $34\text{ }\mu\text{m}$ , Diameter 19.05 cm.

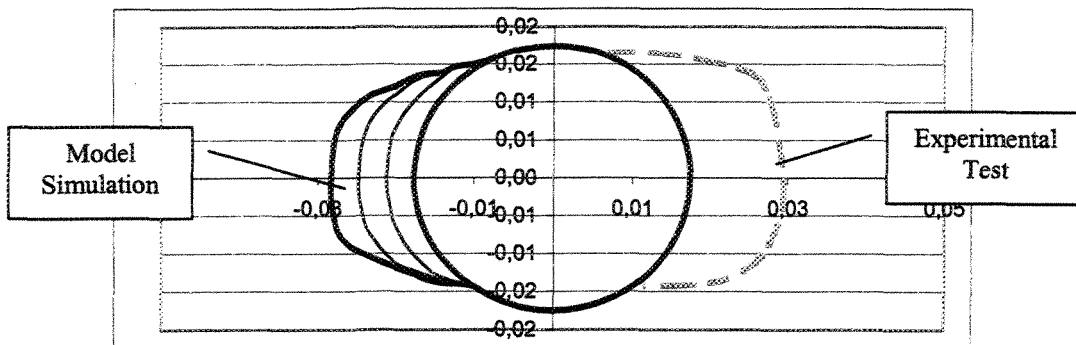


Figure 6.11 Comparison of ice shape - Case 2

Conditions: Air Speed 5 m/s, Air Temperature  $-15^{\circ}\text{C}$ ,  
MVD  $35\text{ }\mu\text{m}$ , Diameter 34.9 cm.

Figure 6.11 shows a further example of the ice shapes obtained under dry icing conditions with a change in cylinder diameter from 19.05 cm to 34.9 cm. On the left-hand side of the figure are the shapes predicted by model calculations, while the right-hand side shows the shape obtained by experimental measurement. The numerical simulation is in agreement with the experimental counterpart as regards ice-growth tendency on the

whole, whereas the shape in the model prediction appears to be slightly narrower than the one in the experimental measurement. This may be explained by airflow and Local Collision Efficiency calculations, where the boundary layer separation occurs at about  $80^\circ$  for a cylinder with a moderately rough surface. It should also be noted that the oversized roughness elements on the ice-covered cylinder may lower the trans-critical Reynolds number. As a result, the boundary layer transition may occur even at a sub-critical Reynolds number as found in the current case, and hence the boundary layer separation may be delayed and occur on the rear of the cylinder. An earlier boundary layer transition, and thus a delayed boundary layer separation, may cause an increase in LCE, therefore the measured ice load in an experimental test should be greater than the ice load from a theoretical prediction under the same condition in both studies. This may be the reason that the ice shapes in the model prediction are narrower than those in experimental tests.

It should be noted, furthermore, that Cases 1 and 2 share all their parameters except for the cylinder diameter, however, the ice mass in the test for Case 1 covers more surface area than the one accumulated in Case 2. The ice mass on a small cylinder is not proportional to the diameter of the cylinder, as might be deduced from the figure, rather, the ice accretion process on a small cylinder tends to show a higher icing rate, as will be shown in the next chapter. Based on observation of the above two cases, the proposed ice model displays good performance in simulating and predicting ice growth shapes under dry icing conditions.



Simulating the ice accretion process under wet icing conditions presents a genuine challenge in this field of research. Case 3 was designed to respond to such a requirement, and a comparison of ice shapes under semi-wet icing conditions is provided in Figure 6.12. The ice shapes obtained from the model simulation are displayed on the left-hand side of the figure, while the shapes from test measurements are shown on the right-hand side. The ice is found to be asymmetrically distributed along the  $x$  axis, and the extra ice on the lower half of the cylinder presents a sharp edge, in accordance with the ice shape measurements on the right-hand side of the figure. The abnormality of the sharp edge may be explained by the processes of surface thermal balance and water movement. The wet regime occurs solely at the leading edge facing the airflow where maximum water impingement is found. This unfrozen water tends to flow downwards. On its downward path, this water encounters adverse cooling fluxes, and then becomes frozen at some point close to its original position. The above process may be identified on the ice shape measurements by the asperity appearing at the leading edge of the cylinder close to the  $x$ -axis. The unfrozen water on the ice surface invariably flows downwards due to gravity. The effect of air drag under such conditions, however, is negligible when compared to the effect of gravity. Symmetry prevails throughout on the right-hand side except for the above-mentioned asperity. With regard to the simulated ice shapes on the left-hand side, some extra ice may be seen on the lower half of the frontal edge, which is an indication of semi-wet icing. The fact that both upper and lower edges of the ice mass remain dry is confirmed by the ice growing outward axially. Based on the ice shapes measured, the proposed ice model successfully predicts the ice accretion process under semi-wet icing

conditions, even though the results are overly smooth when compared to those from the tests.

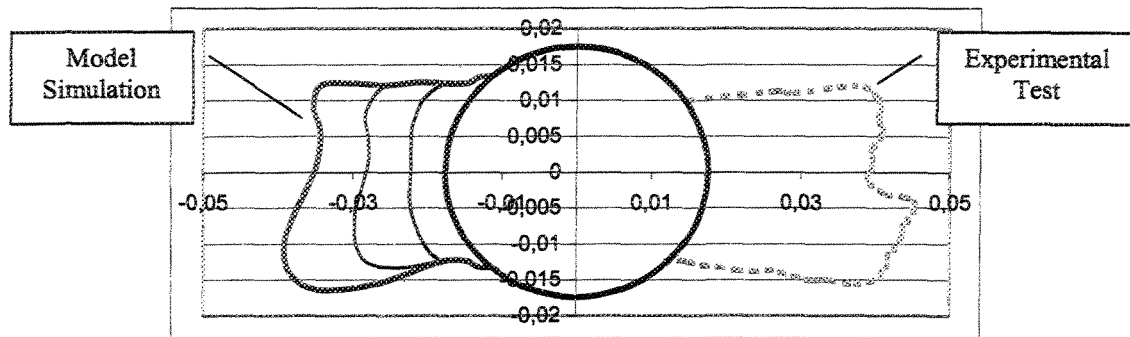


Figure 6.12 Comparison of ice shapes - Case 3

Conditions: Air Speed 5 m/s, Air Temperature  $-10^{\circ}\text{C}$ ,  
MVD  $28\text{ }\mu\text{m}$ , Diameter 34.9 cm.

Case 4 makes use of fully-wet icing conditions. The ice shapes obtained from experimental data and model simulations are provided in Figure 6.13. Under such conditions, a wet regime prevails throughout on the upstream side of the cylinder. The unfrozen water forms a water film on the surface of the iced cylinder, and under the action of gravity and air drag, it tends to flow downwards along the ice surface. Ice produced under these conditions occurs in the form of high-density transparent glaze. The ice shapes measured, as shown on the right-hand side of the figure, present a smooth surface closely similar to those observed in reality (cf. Chapter 2). A comparison between the ice shapes obtained from the experimental measurements and model simulations reveals that the model over-predicts the ice mass located beneath the cylindrical object. This may be explained by the fact that the ice shape is not uniform along the longitudinal span of the cylinder contributing to the formation of icicles on the lower half. In the

proposed ice model, however, the mechanism of icicle formation has not yet been taken into account, consequently the ice shape used for the comparison is only a single cross-section of the ice shape extracted from an interval between two successive icicles. A further difficulty in predicting the exact ice shape on the lower half of the cylinder arises from the water flow along the span. As a result, the simulated ice shapes on the left-hand side of Figure 6.13 display less mass on the lower half when compared to the experimental ice shapes, even though they coincide in a satisfactory manner at all other points.

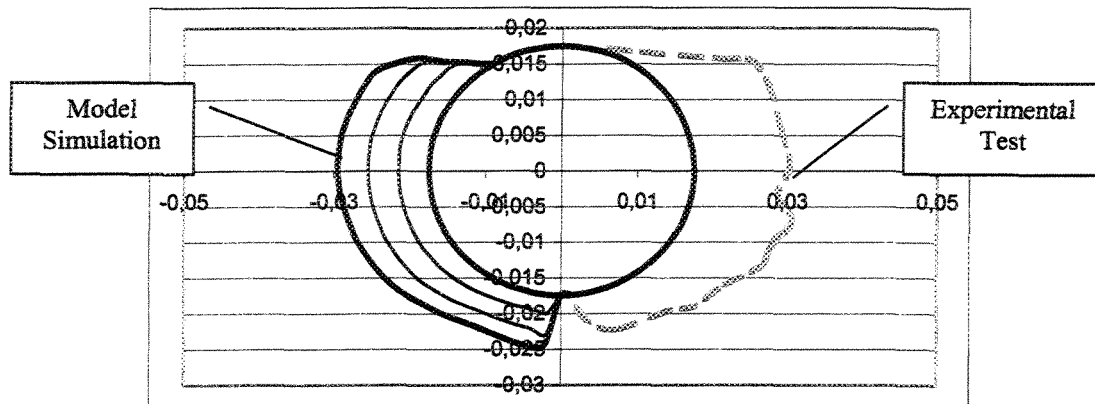


Figure 6.13 Comparison of ice shapes - Case 4

Conditions: Air Speed 5 m/s, Air Temperature  $-5^{\circ}\text{C}$ ,  
MVD  $26\text{ }\mu\text{m}$ , Diameter 34.9 cm.

The same conclusion may be reached for Case 5, which is also a wet-ice accumulation. The simulated cylinder was specified to be 19.05 mm in diameter, while the simulated ice shapes and the one obtained from the experimental test are shown on the left- and right-hand sides of Figure 6.14, respectively. The major difference between simulated and experimental ice shapes may be observed at the bottom of the ice accretion, where the new ice model predicts a slightly heavier ice mass beneath the cylinder, than the mass occurring in the same position for experimentally measured ice shapes.

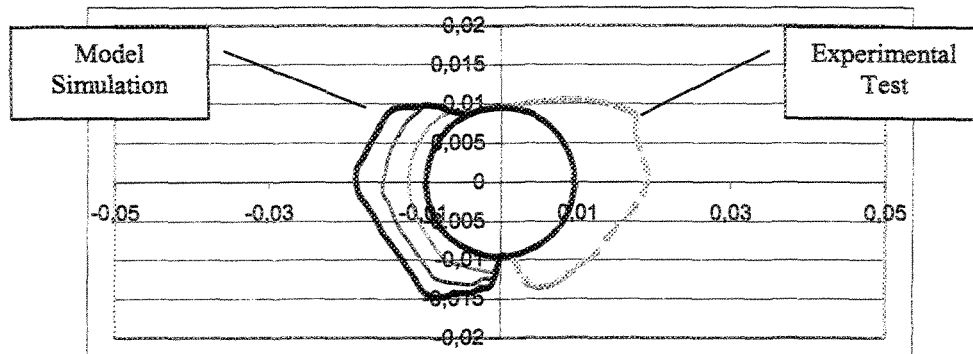


Figure 6.14 Comparison of ice shapes - Case 5  
 Conditions: Air Speed 5 m/s, Air Temperature  $-5^{\circ}\text{C}$ ,  
 MVD  $33\text{ }\mu\text{m}$ , Diameter 19.05 cm.

## 6.5 Conclusion

This chapter provided a description of the experimental set-up and procedures involved in the current test program. The ice shapes obtained from these tests were then compared with those obtained by simulating the ice model under discussion. It may be concluded that, on the whole, the proposed ice model displays good performance capacity for simulating and predicting ice-growth shapes under dry- and wet- icing conditions.

## CHAPTER 7

### MODEL SIMULATION

The basic components of the proposed icing model have been introduced in the preceding chapters. In this chapter, a discussion of the model will be provided as an overview; it will include the way in which the components work together to simulate the ice accretion process on a cylindrical object which may be either current-carrying or not. The techniques used to implement the proposed ice model into a computer code will also be described briefly. Lastly, the new ice model will be used as a tool for examining the effects of several factors on the ice load and shape as they occur on transmission line cables. These factors include Joule heating, the Median Volume Diameter (MVD), and cable size, among others.

#### ***7.1 Structure of Ice Model***

Figure 7.1 is used to demonstrate the general structure of the icing model under discussion, and the parameters transferred from one to another. The role of airflow computation is pivotal in the model, since the output of this calculation provides the basic parameters for subsequent components. Thus, the calculation for airflow past the iced body should be carried out at the outset of the model calculation. Then, it becomes possible to track the trajectories for an array of water droplets according to the velocity distribution so obtained, and thereby to determine the Local Collision Efficiency (LCE). Subsequently, the local Heat Transfer Coefficient (HTC) may be evaluated according to

the regularly updated velocity distribution on the boundary, and based on the same velocity distribution, the thermal-balance equation may be solved so as to estimate the icing fraction of the water collected on each surface element. This stage is followed by a simulation of surface water-film flow to determine the water-film thickness and water flow speed. Lastly, after each simulation step, the ice shape, ice density distribution, ice load and rotational angle may be obtained.

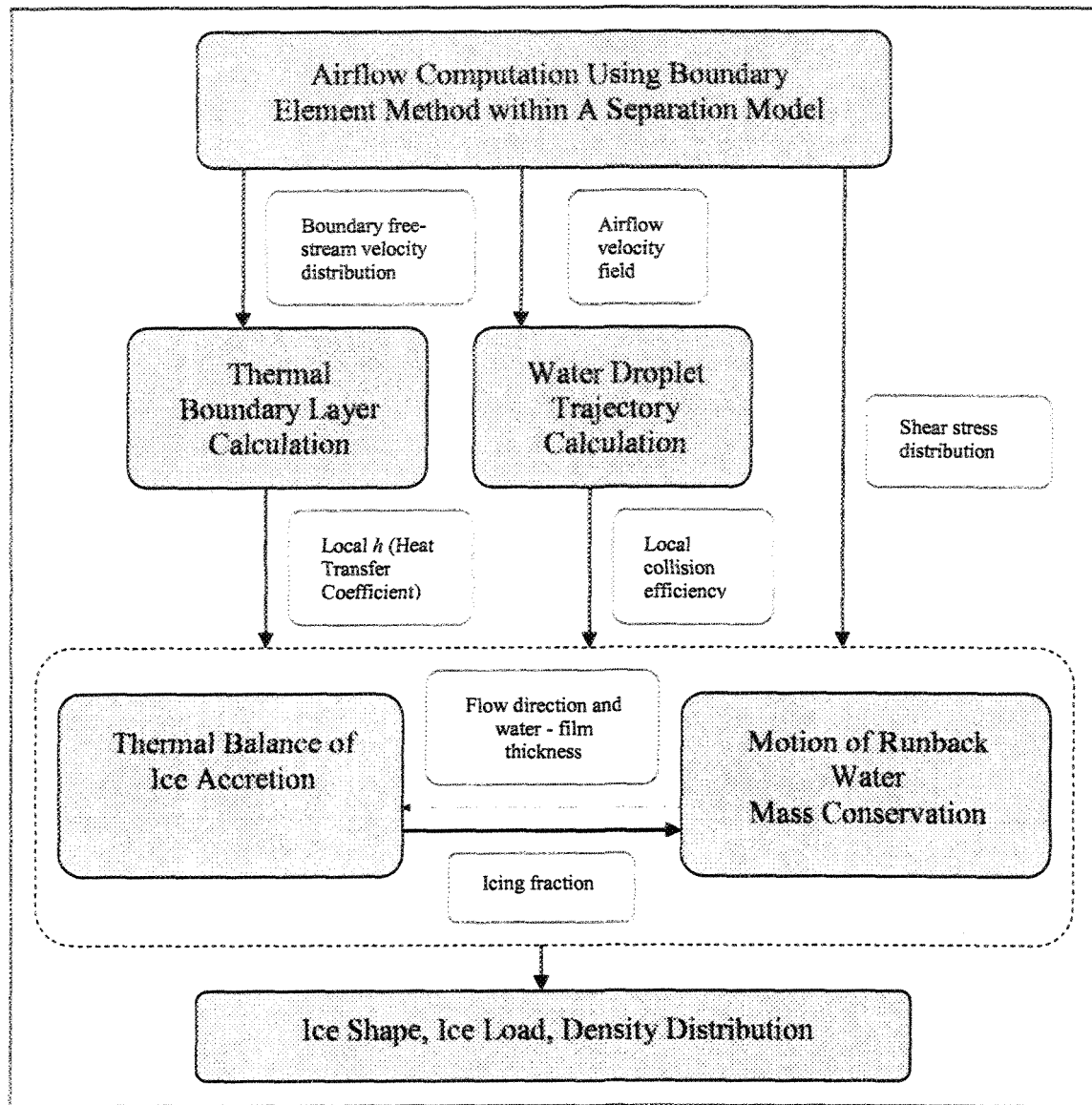


Figure 7.1 General structure of the proposed ice model

## 7.2 Model Input Parameters

A number of model input parameters need to be defined in advance so as to initiate a new simulation process. These parameters may be classified into two types according to

their nature: atmospheric or meteorological conditions and simulation parameters, as listed in Table 7.1.

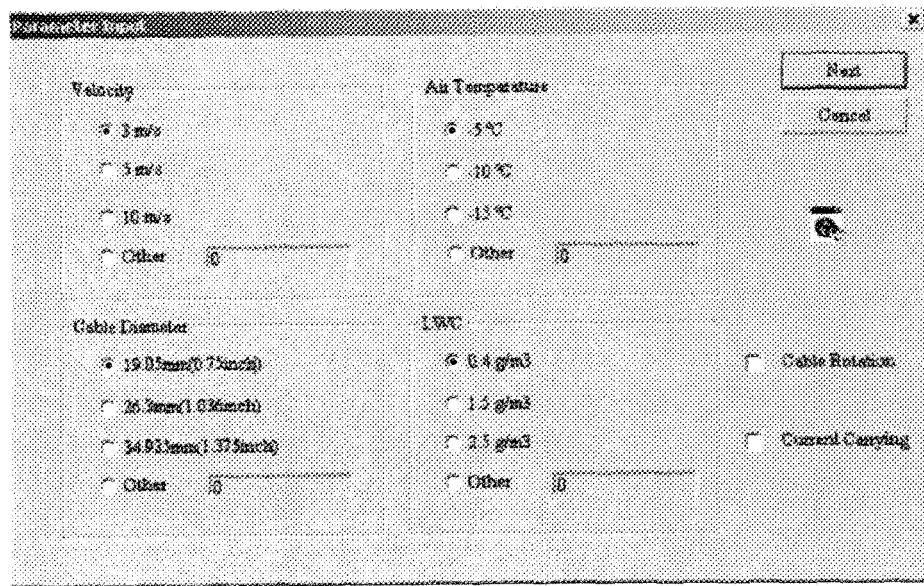
Type	Simulation Conditions
Icing Conditions	Air Speed, Air Temperature, Droplet-Size Distribution, Liquid Water Content (LWC), Relative Humidity
Simulation Parameters	Icing Event Duration, Simulation Time, Cylinder Diameter

Table 7.1 Model Input Parameters

Certain other parameters may be evaluated on the basis of the above-mentioned simulation conditions, including the air density, air viscosity and thermal conductivity, among others.

The corresponding graphic interfaces for these parameters in the ice code are shown in Figure 7.2. Apart from the parameters mentioned above, users are also provided with the option of determining whether the cylindrical object is current-carrying, and whether it is flexible or rigid. It should be noted that hardly any restrictions are imposed on choosing values for these parameters, even though the commonly-used values for each of them are listed in the parameter-input interfaces. Figure 7.2 (b) illustrates the duration in minutes of the icing event, that is to say, the time that any icing event under study lasts. The simulation time corresponds to the time consumed by the computer in order to simulate the ice accretion process.

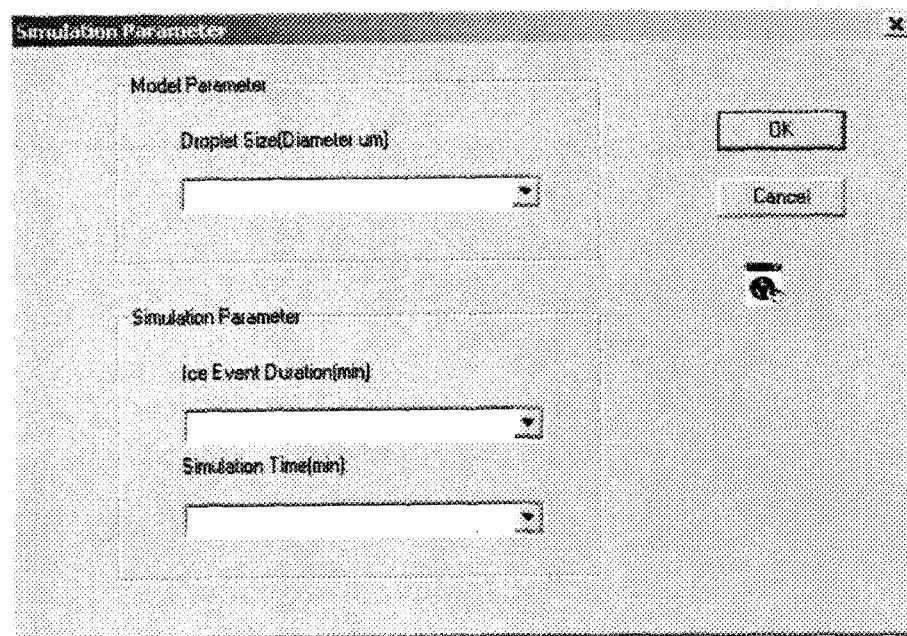




Parameter Input

<b>Velocity</b> <input checked="" type="radio"/> 3 m/s <input type="radio"/> 5 m/s <input type="radio"/> 10 m/s <input type="radio"/> Other: <input type="text"/>	<b>Air Temperature</b> <input checked="" type="radio"/> -5 °C <input type="radio"/> -10 °C <input type="radio"/> -15 °C <input type="radio"/> Other: <input type="text"/>	<input type="button" value="Next"/> <input type="button" value="Cancel"/> <input type="button" value="Help"/>
<b>Cable Diameter</b> <input checked="" type="radio"/> 19.05mm(0.75inch) <input type="radio"/> 26.3mm(1.03inch) <input type="radio"/> 34.93mm(1.375inch) <input type="radio"/> Other: <input type="text"/>	<b>Ice Density</b> <input checked="" type="radio"/> 0.4 g/m <sup>3</sup> <input type="radio"/> 1.5 g/m <sup>3</sup> <input type="radio"/> 2.5 g/m <sup>3</sup> <input type="radio"/> Other: <input type="text"/>	<input type="checkbox"/> Cable Rotation <input type="checkbox"/> Current Carrying

( a ) Parameter input, Interface 1



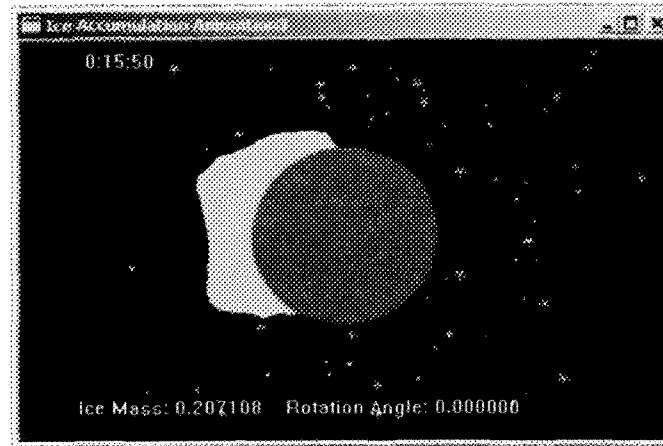
Simulation Parameters

<b>Model Parameter</b> Droplet Size(Diameter um) <input type="text"/>	<input type="button" value="OK"/> <input type="button" value="Cancel"/> <input type="button" value="Help"/>
<b>Simulation Parameter</b> Ice Event Duration(min) <input type="text"/> Simulation Time(min) <input type="text"/>	

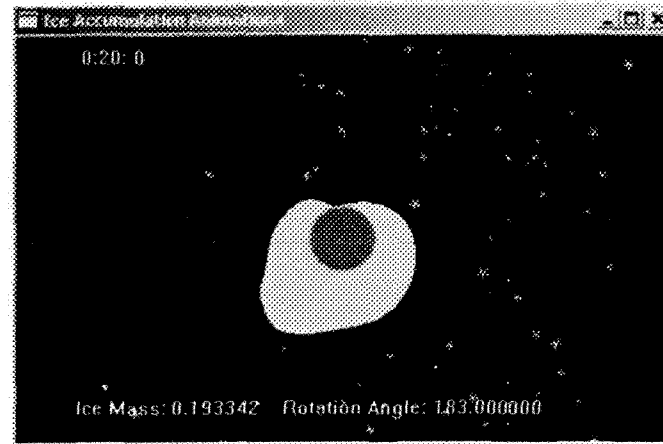
( b ) Parameter input, Interface 2

Figure 7.2 Parameter input interfaces in ice code

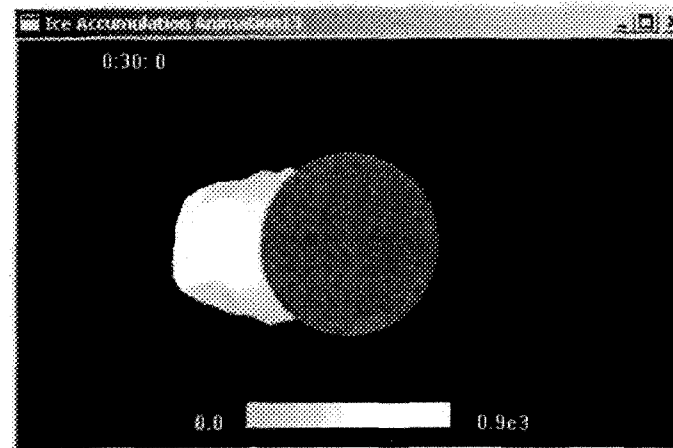
### 7.3 Model Output



( a )Simulation for a non-rotating ice-covered object



( b )Simulation for a rotating ice-covered object



( c )Density distribution in ice mass

Figure 7.3 Visual display for ice accretion processes

Running the current ice model will yield the ice shape, ice load, and density distribution of the ice accretion, which are all the most relevant outputs for any ice model. These output parameters are displayed on a computer screen, as shown in Figure 7.3. A number of related parameters from model simulations, not directly related to the properties of ice accretion, may be of similar importance as the preceding parameters to researchers and even to the average layman, since they may contribute to further understanding this particular phenomenon. These parameters include the distribution of airflow velocity, LCE, HTC, and water-film thickness. All these parameters are updated time-dependently during each time step in the ice model or code.

#### ***7.4 Computer Techniques for Implementing the Proposed Ice Model***

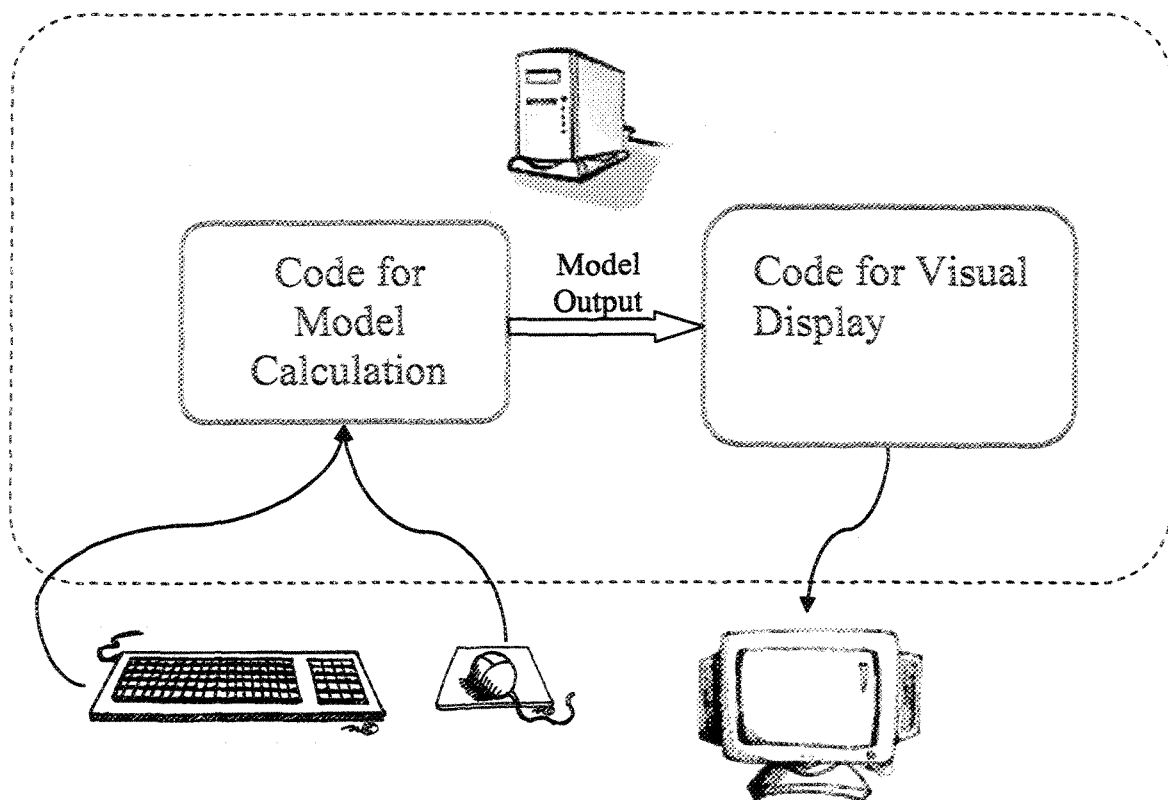


Figure 7.4 Conceptual representation of the ice code under discussion

As shown in Figure 7.4, the programs for model calculation and for the visual display of the icing process were mutually independent in terms of their functions and coding phases even though they co-exist within the same code. As a result, any modification to the ice model or code will not affect the program for the visual display. It should be noted that the computer language used to implement model calculations need not necessarily be C++, as was used here. The language could also be Fortran, as preferred by a large majority of researchers. If the developing process of an ice code is divided into two phases: code-developing and code-linking, then no major change will be observed in the code-developing phase during which the model calculation code may be developed and debugged independently. The code for model calculations will be linked to the visual display code in the code-running phase, so that the calculation results can be animated by the same display code presented earlier.

The computer code initiates model calculations upon receiving the model simulation parameters designated by the user. At each simulation step, the subroutine for model calculations sends a new set of calculation results to the visualization subroutine so as to update the ice image on the screen in real time. The user may control and intervene in the simulation process either by changing computer simulation time or by modifying the display mode. The user also has the option of observing the time evolution of a number of parameters such as the airflow past the iced cylinder or the local LCE, all of which present great interest for research.

As mentioned earlier, the computer code under discussion was written in C++ based on Object Oriented Programming technology. By using this technology, a voluminous coding task may be managed with high efficiency, and the code itself becomes very flexible and may be expanded to a larger scale with relatively greater ease than with conventional programming methods.

A hierarchical diagram showing the classes of the ice code under discussion may be seen in Figure 7.5. It will be observed that the classes of the ice code were divided into three levels according to the degree of generality or abstractness. The classes on the top level of the hierarchy are those essential to the ones beneath them. For example, the class referring to the geometry of an iced cylinder and the class referring to the key parameters, are both indispensable to the airflow and thermal boundary calculations shown on the next level. The classes on the middle level are used to carry out certain specific calculations, such as those for droplet trajectory and thermal balance calculations. These calculations are in turn controlled and manipulated by a single class called the CControlSession. Shown at the bottom of the hierarchical diagram is the class Cview, which is more straightforward for the user, since it provides subroutines for user-code interaction and for visualizing model calculation results .

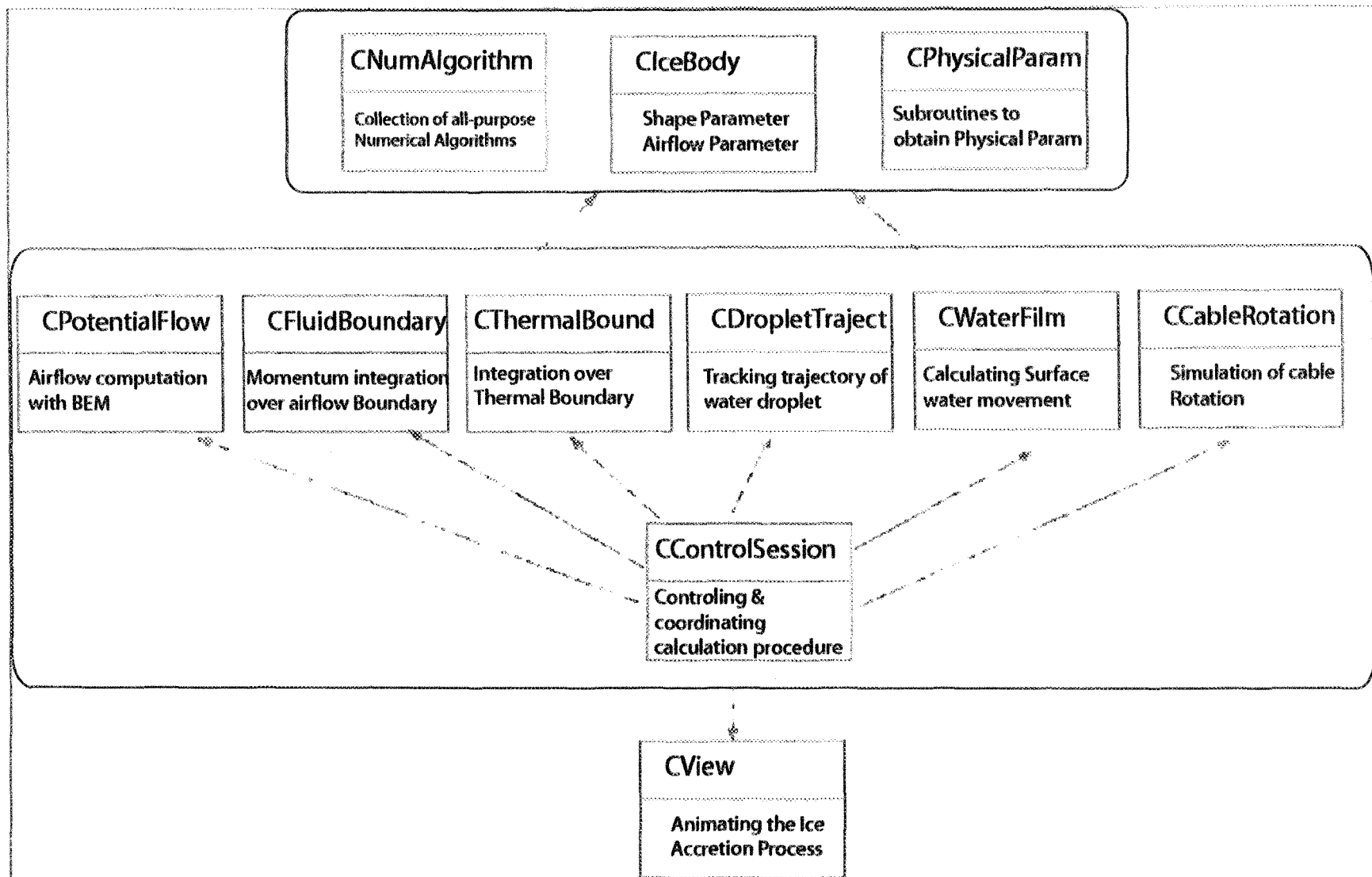


Figure 7.5 Hierarchical diagram for classes of ice code

## 7.5 Model Simulations

Three simulations were carried out so as to demonstrate the influence of the proposed calculation procedure. The results of these were then compared with those from the simplified classical method which assumes a constant Langmuir distribution for the LCE, commonly applied so far in existing icing models. The simulation conditions are as listed in Table 7.2

Group No.	Model Input Parameters				
	Air Speed (m/s)	Temp. (°C)	MVD ( $\mu\text{m}$ )	Diameter (mm)	LWC ( $\text{g/m}^3$ )
1	10	-12	20	34.9	1.0
2	10	-12	30	34.9	1.0
3	5	-12	30	34.9	1.0

Table 7.2 Model parameters for comparisons between classical and new LCE methods

The ice accretion shapes shown in Figures 7.6 (a), (b) and (c), were generated by model simulations for both the classical and newly proposed methods. The ice shapes using the proposed method are shown in the upper part of the figure, while shapes in the lower part correspond to the classical method. It will be observed that the ice thickness is roughly the same at the leading edge for both methods, even though it displays a greater difference elsewhere on the cylinder. Moreover, ice in the classical method tends to grow outward axially, and thus in the direction normal to the wind vector its shape is broader than the one predicted using the new method, as shown in Figure 7.6 (a).

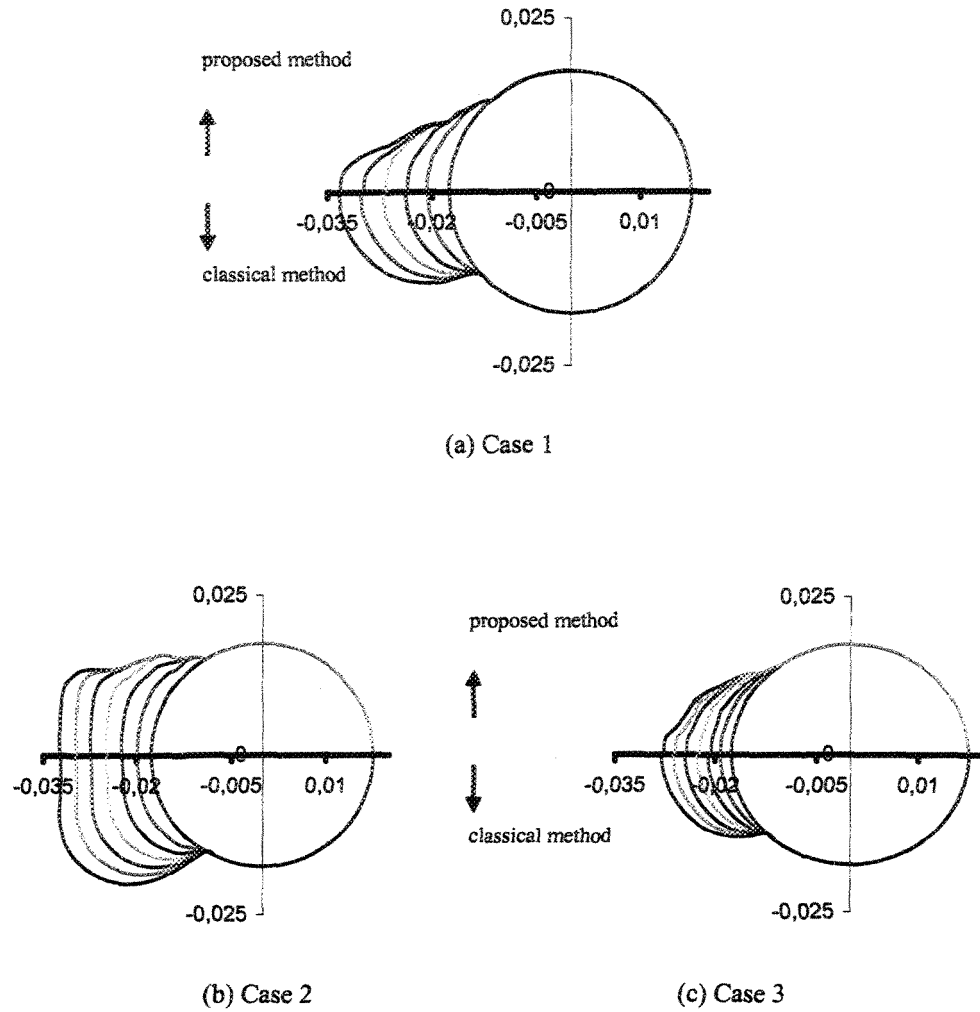


Figure 7.6 Comparison of ice accretion shapes predicted by classical and new methods(time step: 5min)

Figure 7.7 shows three sets of curves representing the time evolution of the ice load for the previous three cases. Each set of curves includes one solid and one dotted curve. The solid line represents the ice load predicted by the method described herein, and the dotted line represents the ice load for the classical method. Only Case 2, represented by the upper curves in red, will be discussed here for the sake of simplicity. During the first 10 minutes of simulation, the two ice-load curves coincide with each other so well that the difference is hardly perceivable. As the simulation proceeds, these two curves begin to



diverge. Finally, at the end of the simulation, ice loads predicted using the classical method were 20 percent heavier than those predicted by the present method.

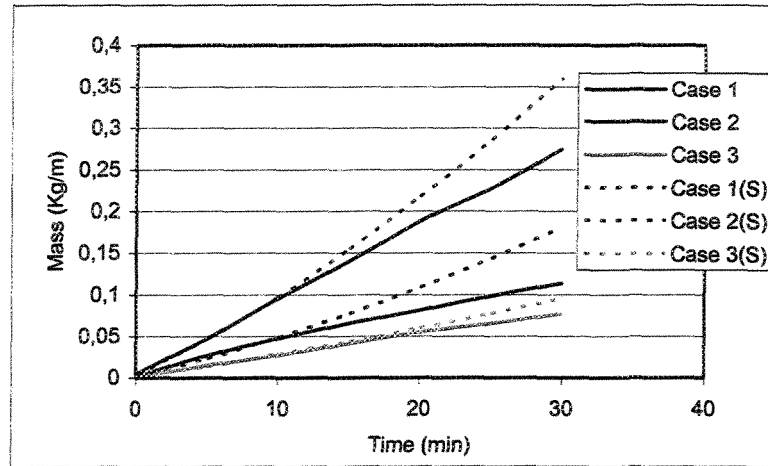


Figure 7.7 Time evolution of ice load predicted by both methods.

### • Joule Heating

Under icing conditions, the electric current carried by a cable may contribute to heat flux for the heat balance processes occurring on the ice surface. The method applied in the model calculation with regard to this heat flux was discussed in detail in Chapter 4. The proposed ice model will be used as a tool to study three individual cases representing dry, semi-wet or wet icing conditions, so as to demonstrate the effects of the above-mentioned resistive heating, or Joule heating, on ice accretion processes. In each case, the ice code will carry out two independent model simulations, the first for an energized cylinder and the second for a cylinder without current.

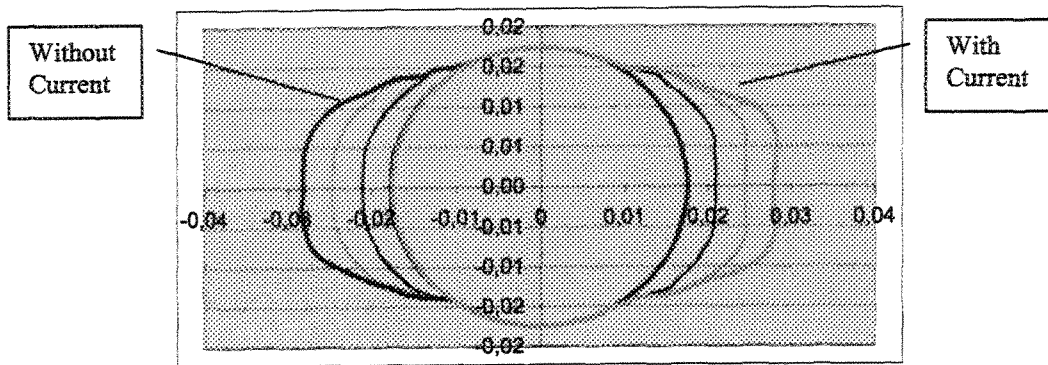
As shown in Table 7.3, the cylinders under consideration for these three cases are all 34.9 mm in diameter. The rated current for cables of this size is  $I = 860 \text{ amp}$ , and the electric resistance is  $R_c = 0.0625 \text{ ohms/mile}$ . The details of the calculation procedure may be found in Chapter 4.

Case No.	Model Input Parameters				
	Air Speed(m/s)	Temperature(°C)	MVD( $\mu\text{m}$ )	Diameter(mm)	LWC( $\text{g/m}^3$ )
1	5	-15	35	34.9	1.0
2	10	-12	26	34.9	1.8
3	10	-5	26	34.9	1.8

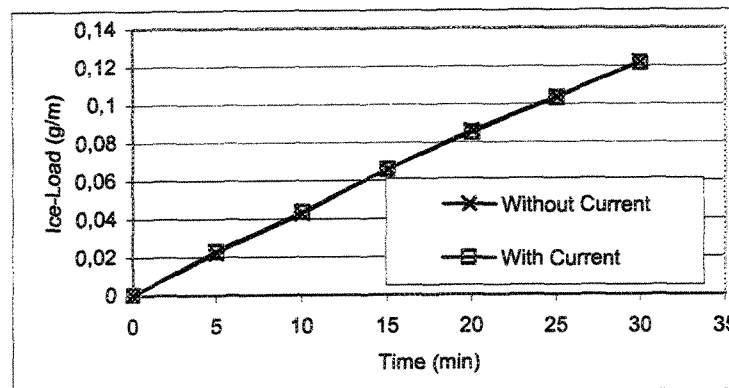
Table 7.3 Model parameters for simulating Joule effects under three distinct icing conditions

The first case was intended to demonstrate the Joule effect on the icing process under dry icing conditions, and the ice shapes and ice-load curves obtained by model simulation are illustrated in Figure 7.8. In Figure 7.8(a), the ice shapes on the left-hand side correspond to a non-energized cable while those on the right-hand side correspond to an energized cable. In the same figure, it will be observed that there is a slight difference in ice shape on the upstream side. A concave curve at the leading edge will be perceived on the right-hand side of the cylinder while no such curve is to be seen on the left-hand side. This may be viewed as proof that the additional heating flux due to Joule heating caused an originally dry accumulation at the leading edge to reduce to a semi-wet accumulation. This reduction is most likely to occur at the leading edge where the cylinder collects the major portion of water impingements, and thus unfrozen impinging water is liable to appear in this location first. This unfrozen water tends to flow downwards, and freezes

while on its downward path. Consequently, a cavity forms at the leading edge from which the unfrozen impinging water is removed through the migration of unfrozen water. It should be noted that in such a case, however, the Joule effect exerts only a moderate influence. Figure 7.8 (b) shows that the two ice-load curves overlap throughout the simulation process, while no variation in ice mass can be detected.

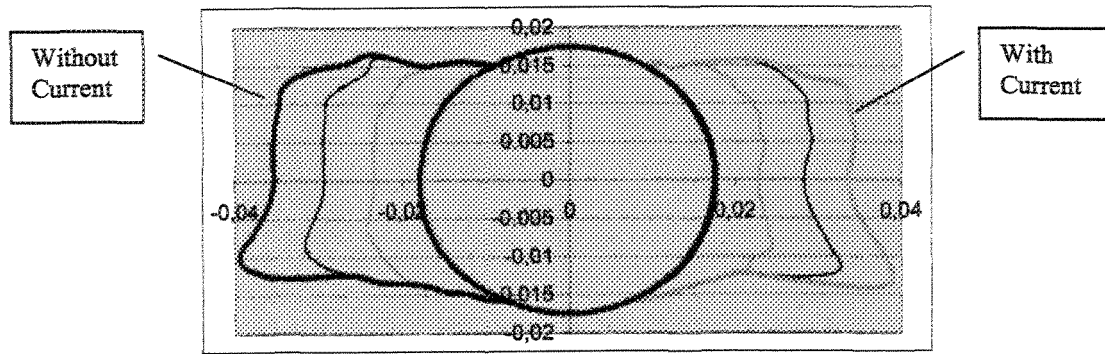


(a) Time evolution of ice shape

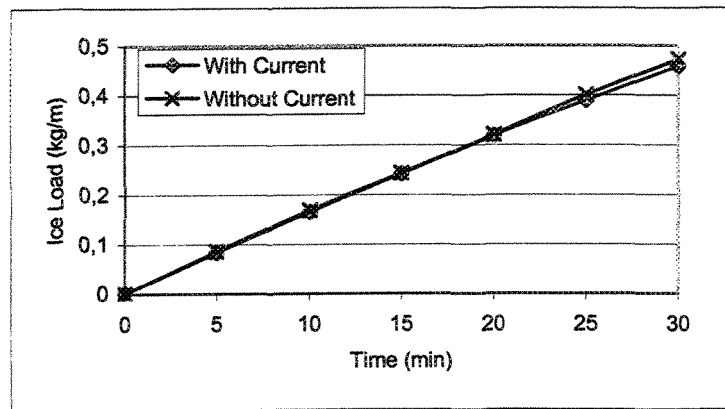


(b) Time evolution of ice load

Figure 7.8 Comparison of ice shapes with and without current for a dry accumulation



( a ) Time evolution of ice shape

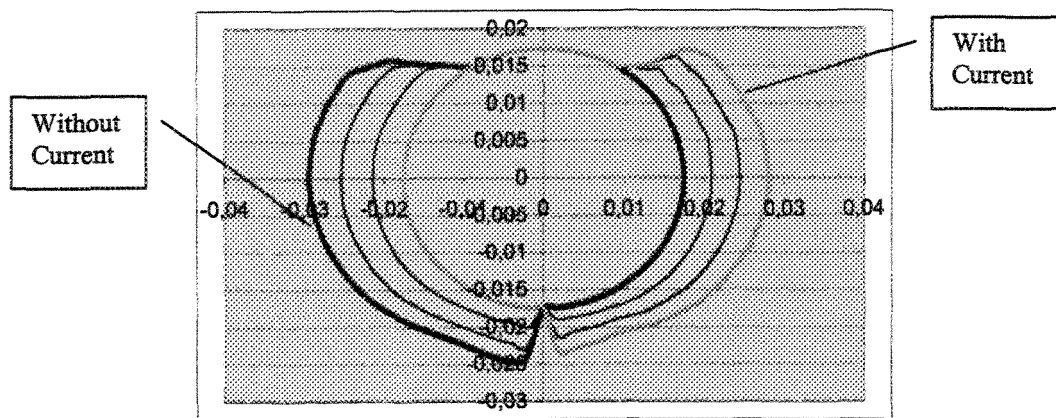


( b ) Time evolution of ice load

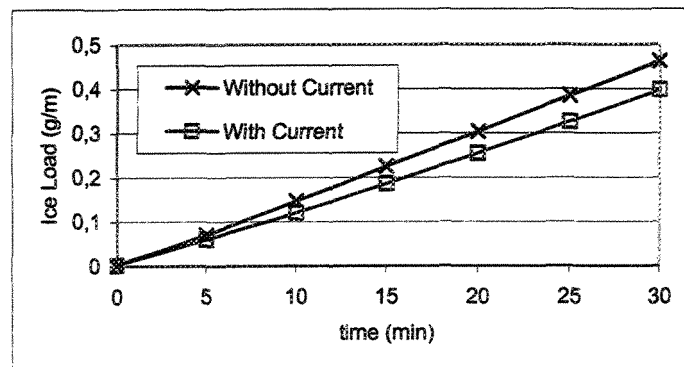
Figure 7.9 Comparison of ice shapes with and without current for a semi-wet accumulation

The second case was designed for semi-wet conditions, and its simulation results are plotted in Figures 7.9 (a) and (b) which show that, on the whole, no major difference in ice shape may be observed between these two sets of ice shapes. The simulation for an energized cylinder still yields a semi-wet ice accretion, while even more ice is predicted at the bottom of the ice accretion, as shown on the right-hand side of the same figure. This may be explained by the fact that the extra heat flux from the electric current, in the case of the energized cylinder, contributes to the formation of more unfrozen water which

then tends to flow downwards along the ice accretion surface. Further data from Figure 7.9 (b) shows that the current-carrying cylinder tends to collect less ice load than its non-energized counterpart, as is revealed by the slow divergence between the two ice-load curves over time. The simulations register a total ice-load loss of five percent for the energized cylinder during a 30-minute simulation period compared to the ice load on the non-energized cylinder.



(a) Time evolution of ice shape



(b) Time evolution of ice load

Figure 7.10 Comparison of ice shapes with and without current for a wet accumulation

Figure 7.10 shows the ice shapes and loads obtained from the model simulations for Case 3 which was designed to demonstrate the Joule effect on a wet-icing process. Figure

7.10 (a) reveals only a slight difference in ice shape, in spite of a pronounced discrepancy in the volume of ice mass predicted by the energized cylinder simulation as opposed to the non-energized one. It may further be observed that the two curves in Figure 7.10 (b) diverge to a marked degree as the simulation proceeds, and consequently a 16% loss in ice-load due to the Joule heating is recorded during a 30-minute simulation for the energized cylinder.

It may be concluded from the above simulations that, under wet-icing conditions, the Joule heating removes a higher portion of ice load compared to the cases under dry or semi-dry icing conditions, although it contributes little to the change in ice accretion shapes.

- **Influence of Cable Size on the Icing Process**

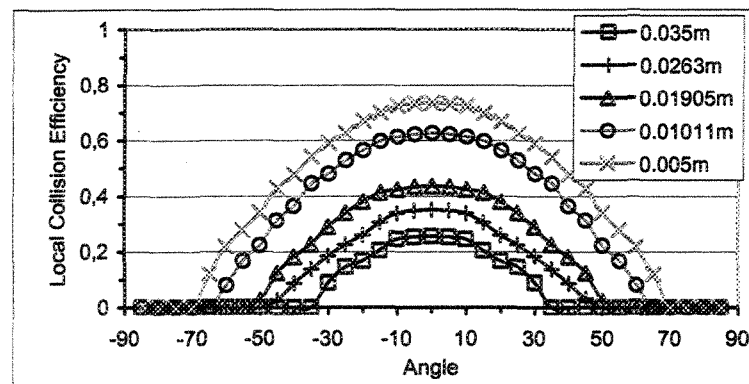


Figure 7.11 Local Collision Efficiency for cylinders of different diameters

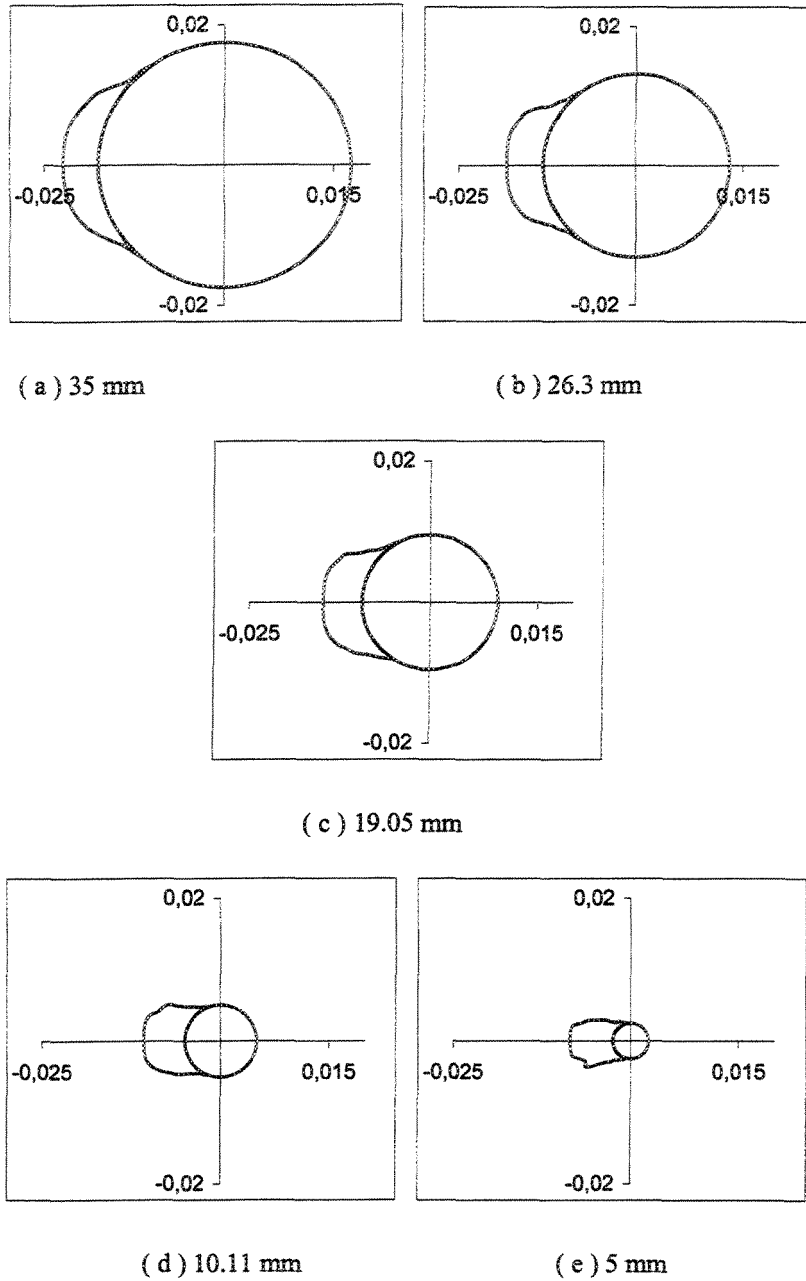


Figure 7.12 Ice Shapes for cables of different diameters

Five cylinders of different diameters were chosen for model simulations with the intention of demonstrating the influence of the diameter factor on both the LCE and the ice shape, as shown in Figures 7.11 and 7.12, respectively. The diameters of these cylinders range from 5 mm to 35 mm. The outermost curve in Figure 7.11 corresponds to

the simulation results for the 5 mm cylinder, while the innermost curve represents those for the 35 mm cylinder. It will be observed that, as the diameter of a cable increases, the value of the LCE rises correspondingly, as does the maximum impingement angle. With regard to the ice shape, it may be seen that a small cable tends to collect a more substantial ice deposit in terms of its size under the same icing conditions, as shown in Figure 7.12. This implies that a higher icing intensity prevails on a smaller cable during the same ice event.

- **Distribution of Ice Density**

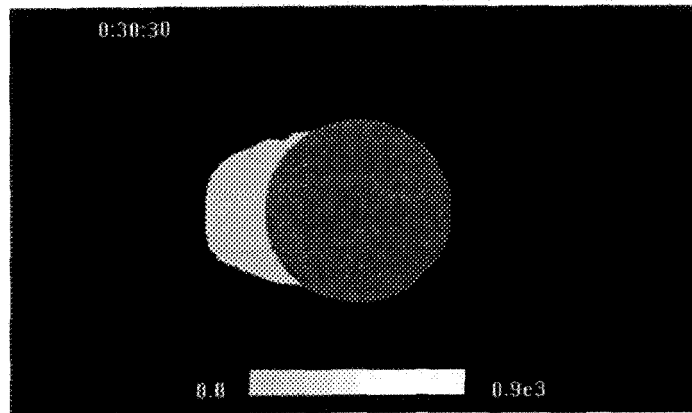
Simulation conditions are provided in Table 7.4 for the three cases simulated using the newly-developed ice code. The corresponding density distributions are shown in Figures 7.13 (a), (b) and (c).

Case No.	Model Input Parameters				
	Air Speed(m/s)	Temperature(°C)	MVD( $\mu\text{m}$ )	Diameter(mm)	LWC( $\text{g/m}^3$ )
1	5	-15	35	34.9	1.0
2	10	-13	22	34.9	1.8
3	10	-5	26	34.9	1.8

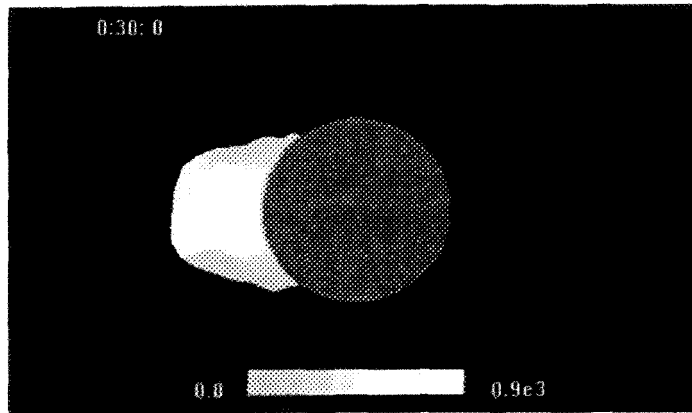
Table 7.4 Model parameters for predicting ice density distributions under three distinct icing conditions

In each of the computer-generated images in Figure 7.13, an iced object is shown in the centre, and the density of the ice deposits is provided in the color-index bar at the bottom of each illustration. The lighter color represents a higher ice density, as is consistent with reality in which glaze displays higher density and a greater degree of transparency.

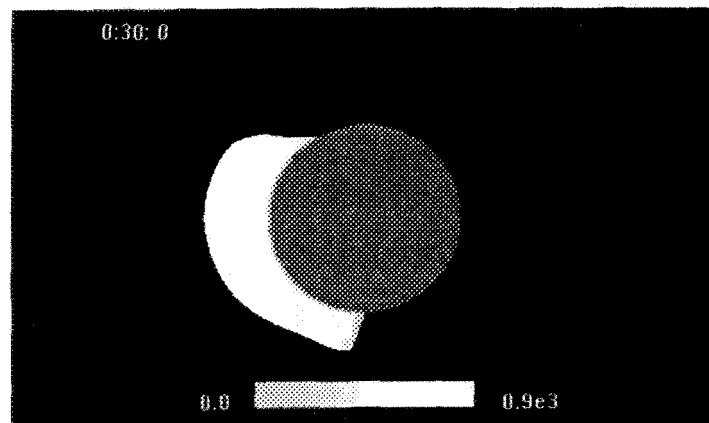




( a ) Case 1: Dry ice accumulation



( b ) Case 2: Semi-wet ice accumulation



( c ) Case 3: Wet ice accumulation

Figure 7.13 Ice-density distribution

Since Case 1 represents a typical dry accumulation at  $-15^{\circ}\text{C}$ , its density is less than  $400\text{kg/m}^3$ , and thus the ice shape was rendered with a darker color.

Case 2 represents a semi-wet ice accumulation. In the centre, a high-density wet regime may be seen, and thus a light color was used to render the shape in this position. On each of the upper and lower edges of the ice mass, dry ice of a low density accumulates, and is thus represented by a darker color. Also, Figure 7.13 (b) reveals a tendency of the ice to be drier at the initial stage, becoming wetter as the icing process advances.

Case 3 represents a wet accumulation where it is clear that the wet regime prevails throughout, thus a light color was used to render the ice shape.

- **Influence of Droplet Size on the Icing Process**

A convenient feature of this newly-developed icing model is that it accepts user-defined MVD values yet it imposes no particular restrictions. This new feature makes it possible to investigate the influence of droplet size on icing processes. Different MVDs are used in the present study as model input parameters for three separate cases, while all other parameters are kept unchanged. A detailed list of the simulation conditions are provided in Table 7.5. It should be noted that these MVDs are intended to represent three separate batches of small-, intermediate- and large-sized droplets.

Case No.	Model Input Parameters				
	Air Speed(m/s)	Temperature(°C)	MVD( $\mu\text{m}$ )	Diameter(mm)	LWC( $\text{g}/\text{m}^3$ )
1	5	-5	50	34.9	2.5
2	5	-5	100	34.9	2.5
3	5	-5	500	34.9	2.5

Table 7.5 Model parameters for investigating the influence of droplet size

Figure 7.14 shows the time evolution of the ice mass in Case 1, where the MVD of the droplets is set at 500  $\mu\text{m}$ . A wet regime prevails on the surface of the ice mass, since this surface is smooth with a low surface icing rate. The ice mass is found not only on the windward side, but also on the leeward side, which may be explained by the fact that the rear surface receives direct water impingement from the incoming water flux which precipitates obliquely rather than horizontally in relation to the icing object. Also, part of the unfrozen water will flow in a clockwise direction, pushing its own pathway even further back. Then, under adverse cooling conditions, ice freezes somewhere on its way downwards on the rear surface. As a result, it may be predicted that the ice mass will cover an increasingly greater part of the rear surface of a cylindrical object with a corresponding increase in the MVD.

When reducing the MVD of droplets to 100  $\mu\text{m}$ , an apparent drop in ice mass is observed on the leeward side of the icing object, as shown in Figure 7.15. Further decreasing the size of water droplets implies that the trajectories of these droplets become horizontal to a greater extent, as in Case 3. Under such conditions water impingement collides solely with the windward-side surface, and also air drag is not strong enough to

carry water film to reach the leeward side of the icing object, as a result, it will be observed in Figure 7.16 that no ice mass presents on the rear surface of the cylinder.

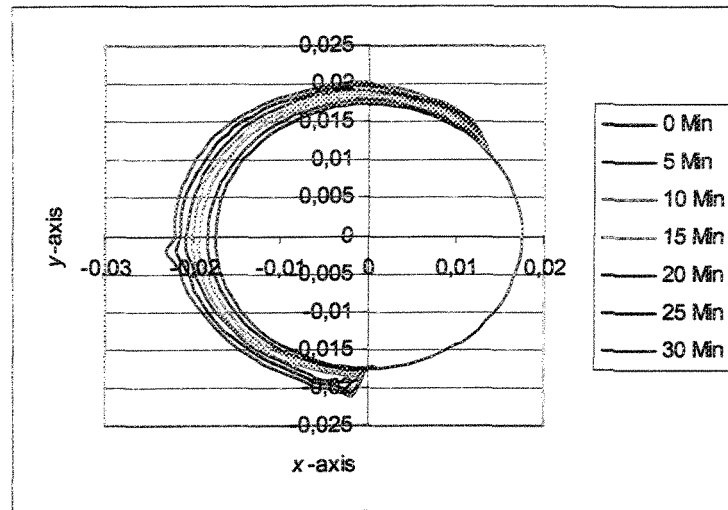


Figure 7.14 Ice accretion for droplets of 500  $\mu\text{m}$ -diameter

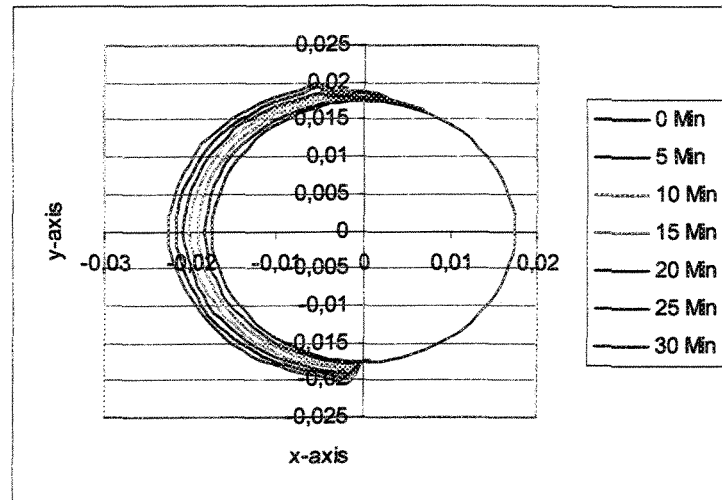


Figure 7.15 Ice accretion for droplets of 100  $\mu\text{m}$ -diameter

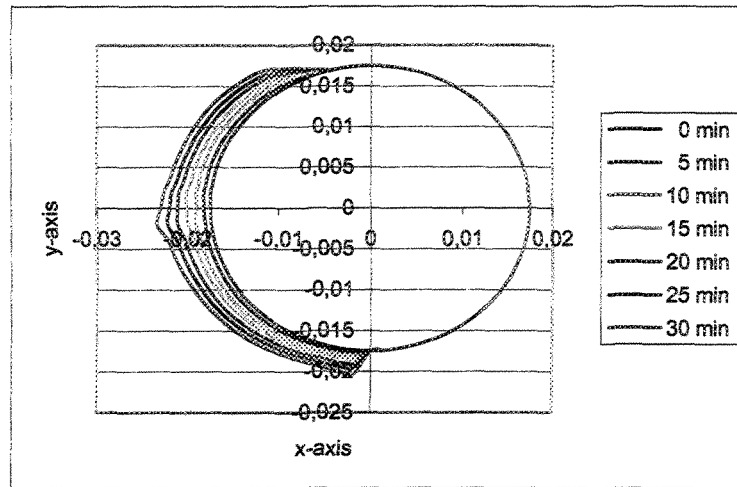


Figure 7.16 Ice accretion for droplets of 50  $\mu\text{m}$ -diameter

Figure 7.17 shows the time evolution of ice mass for three cases. It appears that the case with the largest MVD has a record of the greatest increase in ice load.

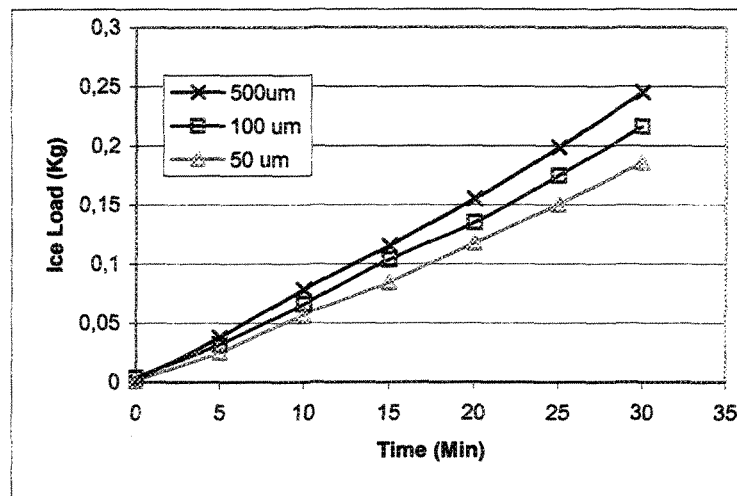


Figure 7.17 Time evolution of ice mass

## 7.5 Conclusions

In this chapter, an overview of the new icing model has been provided, including the general structure with input and output parameters of the model. The techniques used to implement the proposed model into a computer code were then described briefly. Finally,

the new ice model was used as a tool to examine the effects of several factors on the ice load and shape as they occur on transmission line cables.

## CHAPTER 8

### SIMULATION OF CABLE ROTATION

#### *8.1 Introduction*

Transmission cable lines are of great flexibility and tend to rotate over time when ice builds up asymmetrically on the surface. Due to such rotation, the ice mass is liable to be evenly distributed on the surface of the cables. This may serve to explain why the ice shape observed on the transmission line is predominantly circular. The method described in the preceding chapters, however, was originally designed for simulating the ice accretion process on a fixed object. When this method is applied to cable icing, it may undergo certain modifications.

As early as 1983, McComber proposed a model for simulating cable rotation under ice conditions. During the rotation-angle calculation in this model, the wind effect was disregarded and the ice load was assumed to be the only factor leading to cable rotating. The ice mass was evaluated numerically using the Finite Element Method(FEM).

Based on earlier studies, Egelhofer et al. (1984) put forward a new model to simulate cable rotation. In order to evaluate the parameters numerically, the surface was divided into 16 segments on the windward side and the Local Collision Efficiency(LCE) was obtained by solving the droplet velocity field using the FEM. Both gravitational and aerodynamic drag forces were taken into account in the procedure used to acquire the

rotating angle on the iced object. From a theoretical point of view, their model was rendered more satisfactory than previously with the inclusion of these supplementary characteristics.

Further work is necessary, however, to make it possible for an ice model to perform simulations over a more extended period of time, since both the aforementioned models were designed only for simulations at the preliminary stages of cable rotation. Also, these models assumed that the ice deposit would retain an initial simple shape throughout the entire accretion process, making it practically impossible for the simulation of an icing event of long-duration. The method, which will be described below, evaluates the airflow velocity field and thus the LCE on a real-time basis using the potential flow calculation in the context of the boundary-layer separation theory. Such a procedure then makes it possible to carry out precise and reliable model simulations over a long period. By using this model, the ice shapes will be obtained at rotational angles of  $90^\circ$ ,  $180^\circ$ ,  $270^\circ$  or greater.

Unfortunately, the existing body of experimental studies pertaining to this problem is so far limited due in part to the difficulty inherent in designing a viable experimental setup to simulate cable twisting. It is, nevertheless, encouraging to find a published experimental study concerning the formation of ice on test wires in an instrumented wind tunnel, as performed under natural conditions by Personne and Gayet (1988). The torsional rotation resulting from gravitational and aerodynamic torques under natural conditions was simulated by wires set in conical bearings and attached to a helical



spring. The data from these tests will contribute to validating the theoretical study presented herein.

It is worth mentioning that the influence of cable rotation on transmission facilities is not necessarily a negative one. The rotation causes the ice to be more evenly distributed on the cable surface in a roughly circular shape. From the point of view of mechanical analysis, such a change will improve the performance of transmission lines by lessening the potential for galloping, which is one of the adverse effects of ice accretion. Meanwhile, it will also minimize the cross-sectional area for a given mass.

## ***8.2 Basic Principles***

In view of the complexity of this problem, a number of assumptions were made as follows:

- the torques from aerodynamic forces and ice load were assumed to be evenly distributed over the length of the transmission line as shown in Figure 8.1.
  - the ice deposit over the cable surface creates no resistance to cable rotation.
  - the cable rotates at so low a speed that its inertial effect may be disregarded.
- Hence, at any given position, the cable may be seen as being at rest, and the net external torque is balanced by that of the internal resistance.

Figure 8.1 shows one section of the transmission line where both ends, A and B, are fixed. Its length is 60.97 meters. A plane cut, o-o, is applied at point C where the

maximum rotation angle is to be found, then its cross sectional profile may be obtained as shown in Figure 8.2.

Normally, an iced cable exposed under natural conditions is subjected to both gravitational and aerodynamic forces as indicated in Figure 8.2. The aerodynamic forces, including air pressure and air shear forces, are associated with wind speed and the geometry of the iced cable. The rotational angle of the iced cable depends upon the amount of internal torque needed to balance the overall external torque.

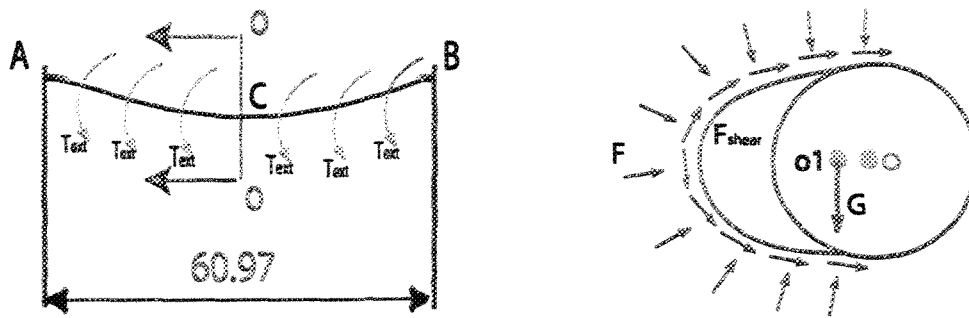


Figure 8.1 One section of cable between two towers    Figure 8.2 Forces experienced by an iced cable

The icing rate over the cable surface was determined on the basis of the calculation procedure introduced in the preceding chapters. The airflow is solved on the basis of the boundary layer theory, in which the airflow about an obstacle may be divided into two regions, namely, the inviscid free stream (potential flow) and the viscous flow boundary layer in the vicinity of the object. Accordingly, flow calculation is divided into two steps, namely potential flow calculation and boundary layer calculation in which the steps are

repeated and are mutually correlative. At the end of each calculation step, the surface air drag, the LCE, and the heat transfer coefficient (local Nusselt number) were recalculated to account for the shape change of the iced cable.

### 8.3 Description of Calculation Procedure

The procedure for determining the rotation angle is based on the resolution of the torque balance equation. The rotation process is assumed to be a static-equilibrium problem and hence the external torque is balanced by the internal resistance torque so developed.

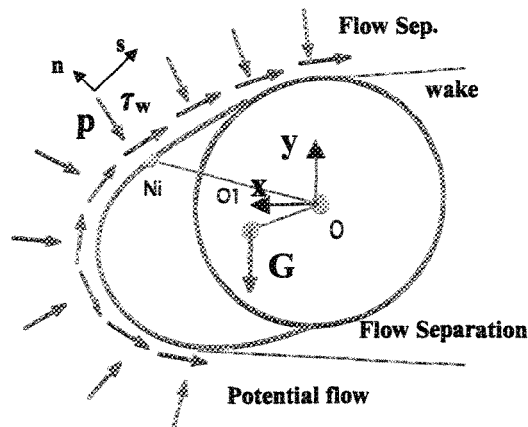


Figure 8.3 Schematic diagram of forces experienced by a rotated cable

#### 8.3.1 Governing Equation

Over the cross-sectional profile, as shown in Figure 8.3, the sum of external torques should be balanced by the internal resisting torque so developed, formulated as follows:

$$T_{External} = T_{Internal} \quad (E 8-1)$$

In formulaic presentation,  $T_{External}$  denotes the sum of external torques, which includes the torque from air pressure,  $T_p$ , air shear force,  $T_f$ , and gravity,  $T_g$ , as follows

$$T_{External} = T_p + T_f + T_g \quad (E 8-2)$$

where:

$$T_p + T_f = \oint (\vec{p} \times \vec{L}_p + \vec{\tau}_w \times \vec{L}_f) ds \quad (E 8-3)$$

in which  $p = p_0 + \frac{1}{2} C_p \rho V_0^2$ , where  $C_p$  is derived from the potential flow calculation defined by  $C_p = 1 - (V_\infty / V_0)^2$ , in which  $V_0$  and  $V_\infty$  represent the onset free-stream speed and free-stream speed on the outer edge of the flow boundary layer, respectively; and  $\tau_w = \frac{1}{2} C_f \rho V_0^2$ , where  $C_f$  is obtained from the momentum calculation of the boundary layer.

$$\text{Also,} \quad T_g = \vec{G} \times \vec{ool} \quad (E 8-4)$$

where  $G = L/2 \times w$ , in which  $L$  is the cable span between two transmission towers; the definition of  $ool$  may be found in Fig. 8.3; and

$$T_{Internal} = \phi \times K \quad (E 8-5)$$

denoting the internal resisting torque, where  $K$  is the rigidity constant numerically equal to  $\frac{I_p \times G}{L/2}$ , in which  $I_p$  is the polar moment of inertia,  $G$  is the shear modulus, and  $L$  is the length of the cable.

### 8.3.2 Evaluating the Mass Center

The position of the mass center  $o_1$  may be obtained by using the following equations:

$$X_{o_1} = M_x / M \quad (\text{E 8-6})$$

$$Y_{o_1} = M_y / M \quad (\text{E 8-7})$$

where

$$M = \int \rho dx dy \quad M_x = \int \rho x dx dy \quad M_y = \int \rho y dx dy$$

Since the iced cable surface has been discretized into a number of discrete elements, the integral equations Eq. 8-6 and Eq. 8-7 may be replaced by the finite summation of the values for each element, in the formulation, as follows:

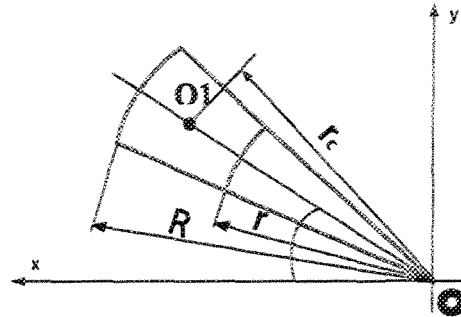


Figure 8.4 Parameters for an arbitrary element of ice deposit

$$M = \rho \sum_{i=1}^n (R_i^2 - r^2) \delta\phi / 2 + m_c \quad (\text{E 8-8})$$

$$M_x = \rho \sum_{i=1}^n (R_i^2 - r^2) \delta\phi / 2 \times r_{ci} \times \cos \phi \quad (\text{E 8-9})$$

$$M_y = \rho \sum_{i=1}^n (R_i^2 - r^2) \delta\phi / 2 \times r_{ci} \times \sin \phi \quad (\text{E 8-10})$$

where  $r_{ci} = \frac{2 \sin \delta\phi}{3 \delta\phi} \frac{(R^2 + Rr + r^2)}{R + r}$ ; definitions of these symbols may be found in

Figure 8.4 which shows the parameters for any given element, i.

### 8.3.3 Position Change of Stagnation Point

The stagnation point is defined as the position where the airflow comes to rest. In calculating the airflow boundary layer, the fluid momentum integration used for determining the separation points always starts from the stagnation point, therefore this calculation should be carried out meticulously in order to diminish the possibility of any inaccuracies arising.

When the cable starts to rotate, a distinct location change of the stagnation point may be observed, as shown in Figure 8.5, where the stagnation point shifts from s1 to s2, and an obvious shift in the distribution of shear stress also occurs. Within the newly-developed ice code, an algorithm was specifically designed for detecting the new position of the stagnation point at each time step, thus ensuring a constantly updated position for subsequent calculations.

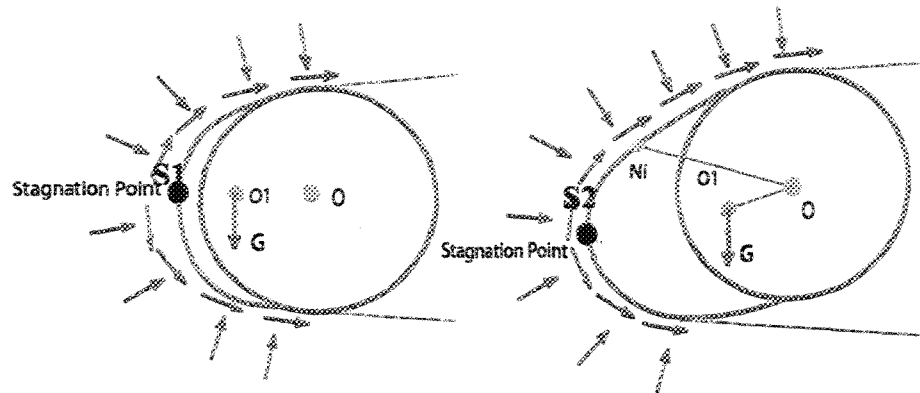


Figure 8.5 Position change of stagnation point as ice accumulates

#### 8.3.4 Solution

Since  $\phi$  appears on both left- and right-hand sides, Equation 8-3 may conveniently be solved in an iterative manner.

#### ***8.4 Simulations and Interpretation of Results***

	Experimental Conditions	Simulation Conditions
Temperature	-12 °C~-18 °C	-15 °C
Diameter	15.7mm	15.7mm
Wind speed	9m/s~12m/s	10m/s
LWC	0.1g/m <sup>3</sup> ~0.6g/m <sup>3</sup>	0.35g/m <sup>3</sup>
MVD	11 μm ~18 μm	15 μm

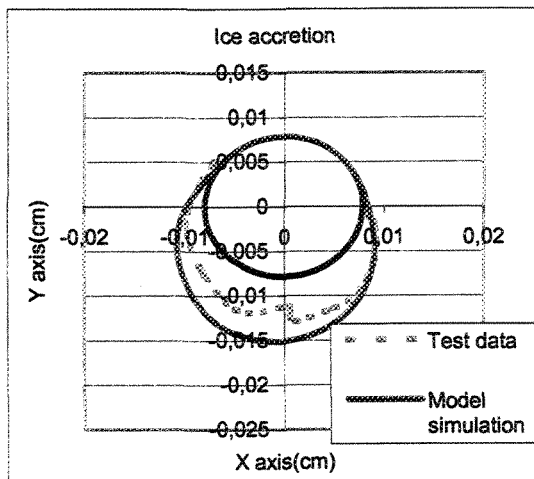
Table 8.1 Conditions for experimental test and model simulation of cable rotation

The simulated ice shapes were compared with the shapes obtained from the experiments carried out by Gayet et al. (1988) so as to validate the theoretical work discussed above. It should be noted that these experimental tests were performed in a natural icing wind tunnel where the test conditions are time-variable, oscillating within a particular range. The mean values of test conditions were used as parameters in model simulation, as shown in Table 8.1. These parameters remain constant throughout.

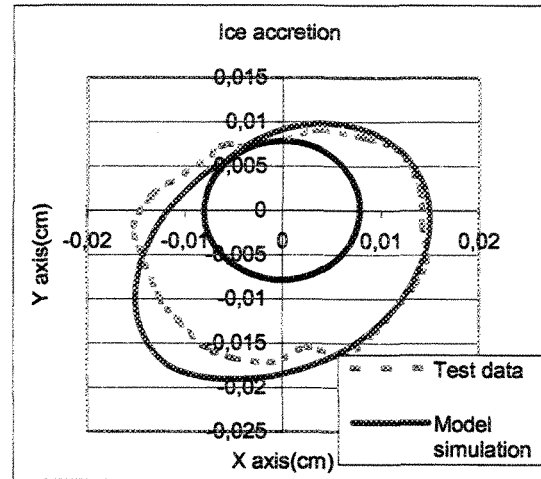
The ice shapes obtained from both studies are shown and compared in Figure 8.6. In general, the simulation agrees satisfactorily with the experimental results except at an early stage, as seen in Figure 8.6(a), where a visible shape difference may be discerned. This may result from an underestimation of the aerodynamic torques, leading to a slower rotation in model simulations, as proved by the appearance of a greater simulated ice



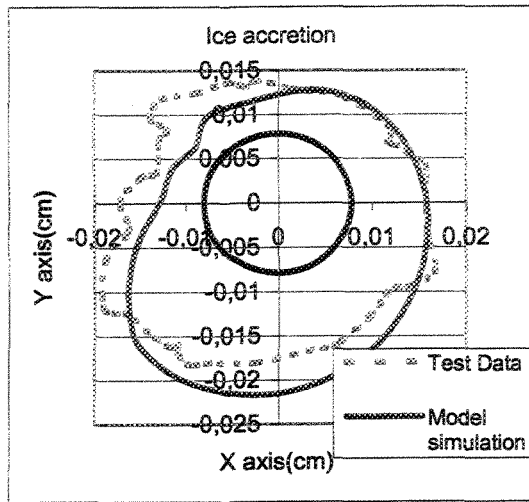
mass in the same figure. Compared to the ice shapes in experimental tests, those in model simulations display an impressive spiral ice accretion, while the surfaces of these shapes present fewer asperities or protuberances. This may be explained, to some extent, by the fact that the tests involved were carried out under natural condition, while the parameters varied over time within a specific range instead of remaining constant, as was the case in the simulation. The discrepancy in ice shape between these two groups tends to diminish as the icing process proceeds. The reason for this paradox may be deduced from the conclusions which will be provided at the end of this chapter.



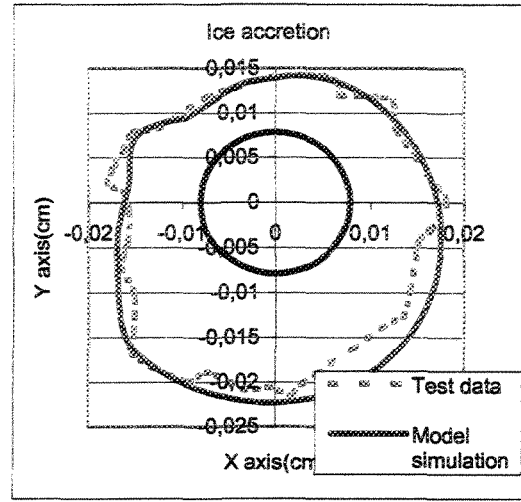
( a ) Rotation angle,  $140^\circ$



( b ) Rotation angle,  $223^\circ$



( c ) Rotation angle, 263°



( d ) Rotation angle, 291°

Figure 8.6 Comparison between ice shapes obtained from experimental and theoretical studies

As one application of the model, two cases were considered and both of them were designed to share all of the simulation conditions except for the torsional stiffness, as shown in Table 8.2. Case 1 was designed to simulate the rigid Bersimis cable, while Case 2 simulated a soft cable of the same diameter as the previous one. The output of the simulation is data capable of generating ice shapes at the mid-span position, as shown in Table 8.3.

The graphs in Table 8.4 show pairs of ice shapes for both rigid and soft cables for simulation durations of 30, 50, 80, 120, and 180 minutes. The ice shapes shown in left column correspond to the simulated icing process on the rigid cable, while those in the right column represent the simulated icing process on the soft cable. It will be observed that ice tends to grow spirally in both cases during the simulation. After 180 minutes of simulation time, a total rotation of 164° was found for the rigid cable and 280° for the soft one. The ice accretion on the soft cable exhibits a perceivably circular shape while

the one on the rigid cable is still asymmetrically distributed underneath. From intuitive deduction one may conclude that ice in Case 1 tends to drop down from the lower surface of the cable due to aerodynamic and gravitational forces.

	Case 1	Case 2
Polar Moment of Inertia	351Nm/rad	100Nm/rad
Temperature	-15 °C	
Diameter	35mm (Bersimis cable)	
Wind Speed	8m/s	
LWC	1.5g/m <sup>3</sup>	
MVD	30µm	

Tab. 8.2 Simulation conditions for both rigid and soft cables

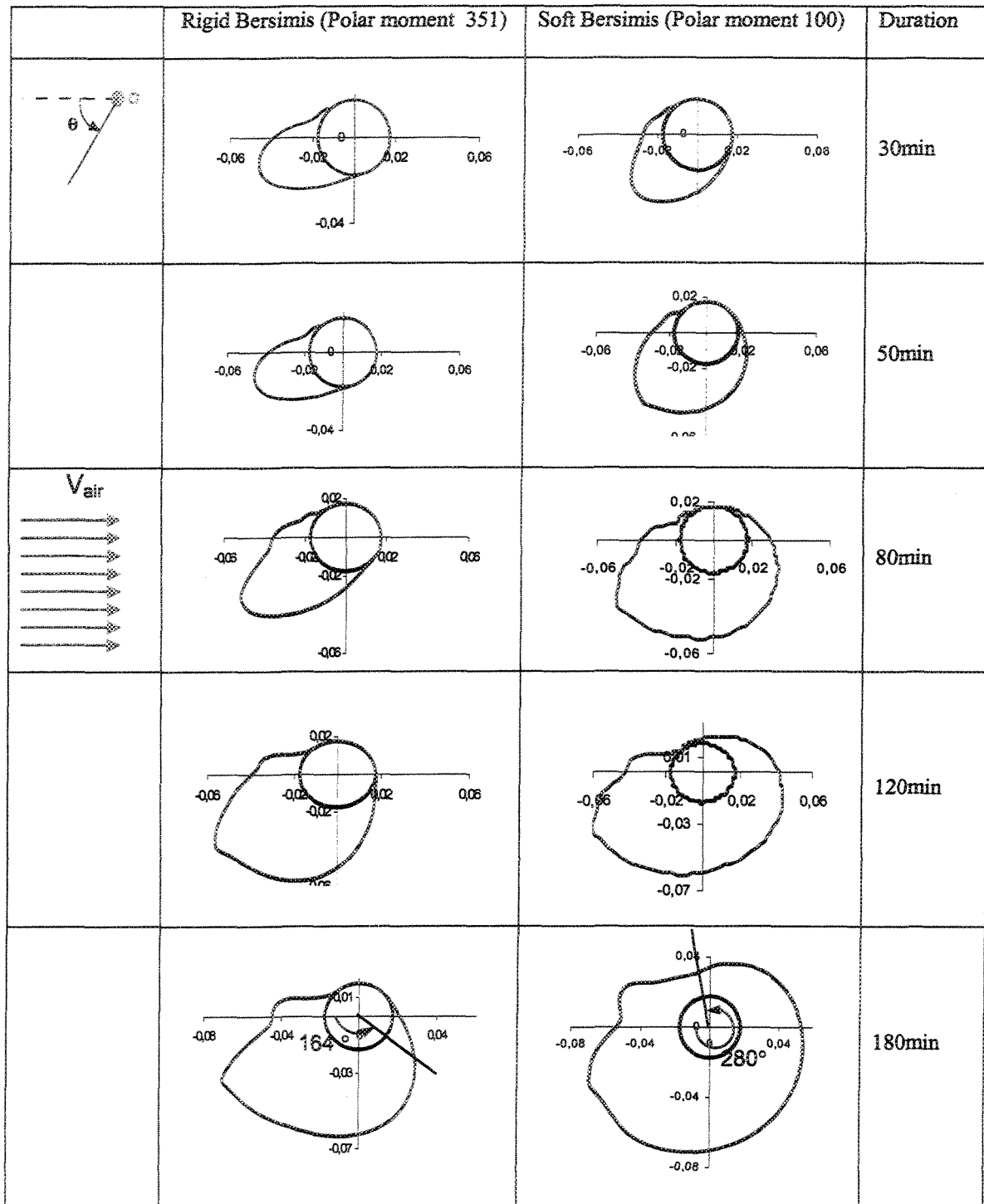
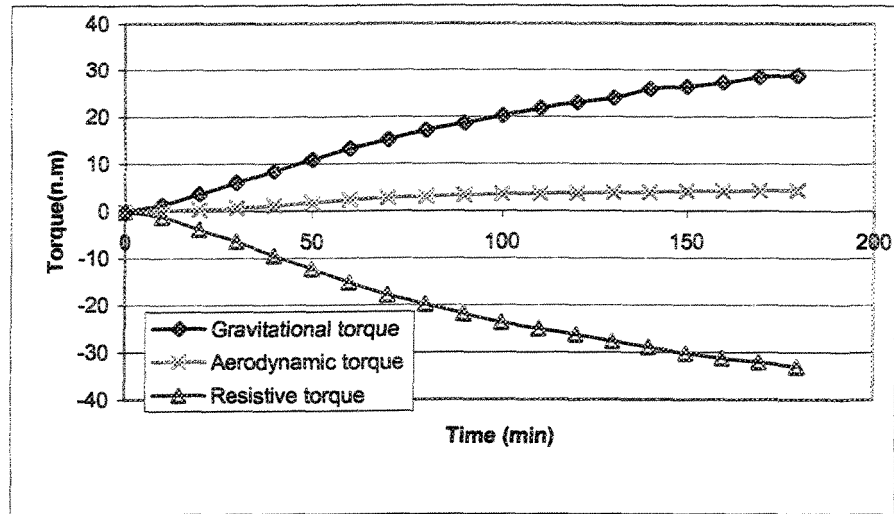
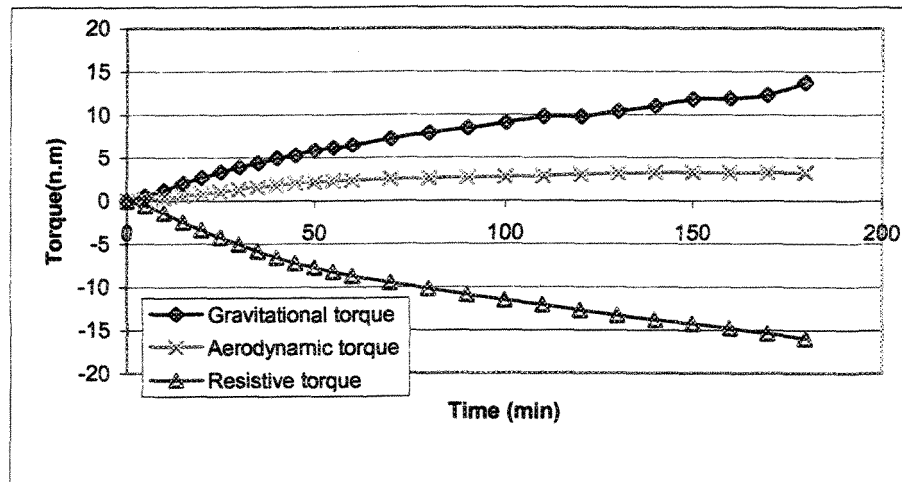


Table 8.3 Predicted ice shapes for both rigid and soft cables



(a) Rigid Cable



(b) Soft Cable

Figure 8.7 Time evolution of external and internal torque

Figure 8.7 shows the history of the external and internal moments for rigid and soft cables. In each case, the gravitational torque first experienced a rapid increase, then a sluggish one, as may be concluded from the slope of the curves. With regard to aerodynamic torque, its value tends to become constant after a certain period of time.

Figure 8.8 shows the time evolution of the cable rotation angle where the upper curve corresponds to the soft cable and the lower curve to the rigid one. It appears that both curves show a similar trend, that is to say, under icing conditions the cable first rotates at a faster pace then it slows down, and eventually rotates at a slower pace, as can be deduced from the slopes of the curves.

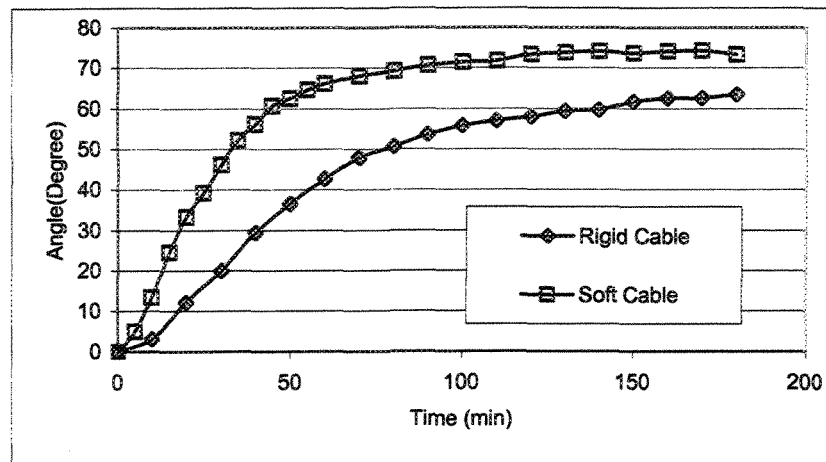


Figure 8.8 Time evolution of cable rotation angle

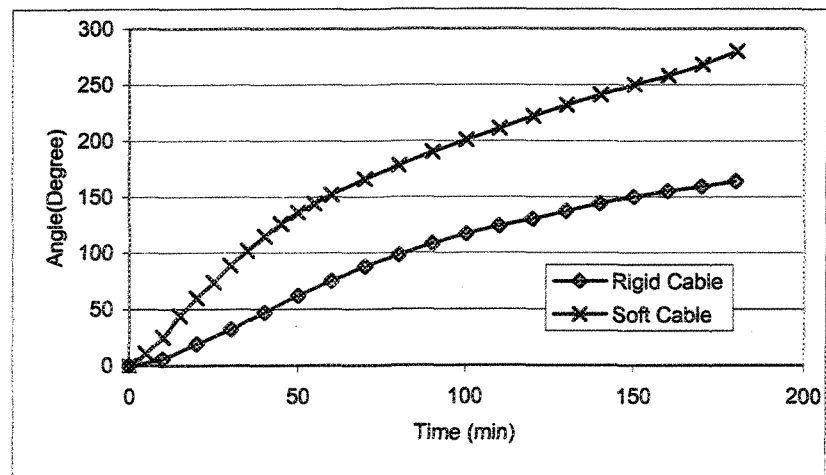


Figure 8.9 Time evolution of weight center angle

Figure 8.9 shows the time history of the weight center angle for both cases. The upper curve corresponds to the soft cable and the lower curve to the rigid one. Once again, both curves show the same trend, implying that during the initial 50 minutes of simulation the weight center shifts at a higher speed. This shift is characterized by a steep slope on each curve, then with the passage of time, the angle of the weight center tends to become constant. The equilibrium angle for the soft cable is approximately  $75^\circ$  while the angle for the rigid cable is approximately  $65^\circ$ .

The history of the ice-mass accumulation is shown in Figure 8.10, in which the mass curve for the soft cable is found at the top. This signifies that a soft cable tends to collect more ice than a rigid cable of the same diameter during the same icing event. It will also be observed in Figure 8.10 that two curves diverge gradually as the simulations proceed, and eventually by the end of the simulation, a 20% greater ice load was predicted for the soft cable.

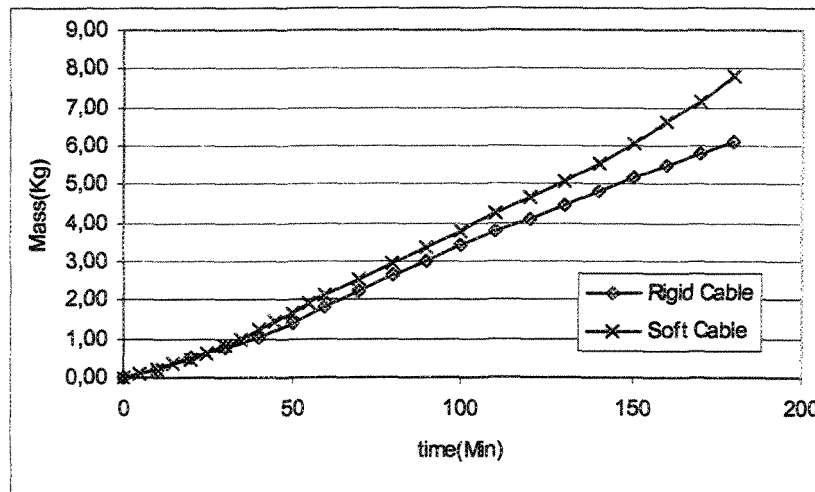
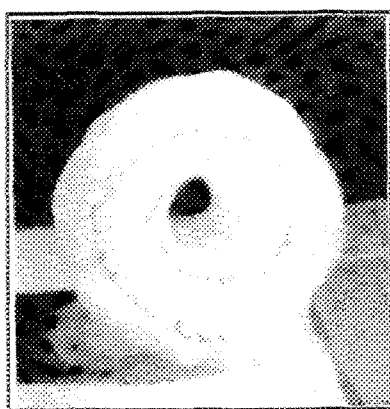
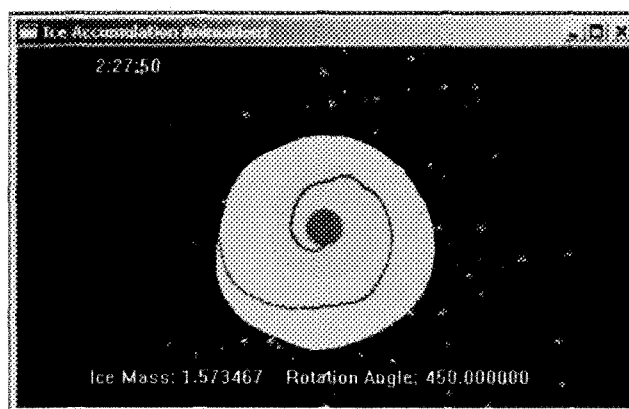


Figure 8.10 Time evolution of ice mass

It is of great interest to employ the proposed method for explaining and reconstructing the evolution process for the ice sample collected under natural conditions. Figure 8.11(a) shows a natural ice mass found on an electric wire at the end of a single ice storm event by people in 1998. In order to reconstruct the ice accumulation process on a computer, a similar ground wire was used as the simulation object in the ice model; the parameters of this ground wire are listed in Table 8.4. The ice shape obtained from such a model simulation is shown in Figure 8.11(b). It will be observed that the rotation angles in both cases are very similar. The ice sample shows a rotation of approximately 1.25 turns, as indicated by the black streak over the cross-sectional plane while its theoretical counterpart exhibits a rotation of 450 degrees. Also, the simulated ice shape displays a pronounced similarity to the shape of the original ice sample. This comparison may serve as further proof that the proposed calculation procedure for cable rotation may be used as a tool for investigating the mechanism of ice accretion as it occurs in a wide range of icing conditions. It is worthwhile mentioning that with the new ice model presented here, it becomes possible to estimate, among other things, aerodynamic and gravitational torques, as well as the total ice load on transmission lines.



(a) Ice sample in nature



(b) Ice shape predicted by numerical model

Figure 8.11 Time evolution of ice deposit



Cable Parameters			Model Input Parameters			
	Diameter (mm)	Torsional stiffness (N.M <sup>2</sup> /Radian)	Air Speed (m/s)	Temperature (°C)	MVD (μm)	LWC (g/m <sup>3</sup> )
	7.94	2.1	10	-5	40	2.5

Table 8.4 Model parameters for reconstructing natural icing process

It would be useful here to provide a description of the test procedure used for measuring the torsional stiffness of the ground wire under consideration. During the torque-rupture test, a 20 cm-long electric wire was used as a test model mounted on a specific test machine. In order to examine the effect caused by the winding direction of a ground wire, two tests were carried out independently. The wire was set to rotate in coincidence with the winding direction in the first test, while it was set to rotate conversely in the second test. At the end of these tests, the curves for the torque vs. rotational angle were obtained, as shown in Figure 8.12. In general, both curves demonstrate a noticeable similarity except for a slight discrepancy in the middle section of these two curves. This discrepancy may, however, cause little difference in the calculation results; therefore it is possible to estimate the torsional stiffness by using either one of these curves. It should be noted that the rotational angle is negligible in relation to the dimension of the cable span. The relationship between the torque and rotational angle, under icing conditions, will thus be found in the elastic zone. Accordingly, the torsional stiffness should be constant throughout the simulation.

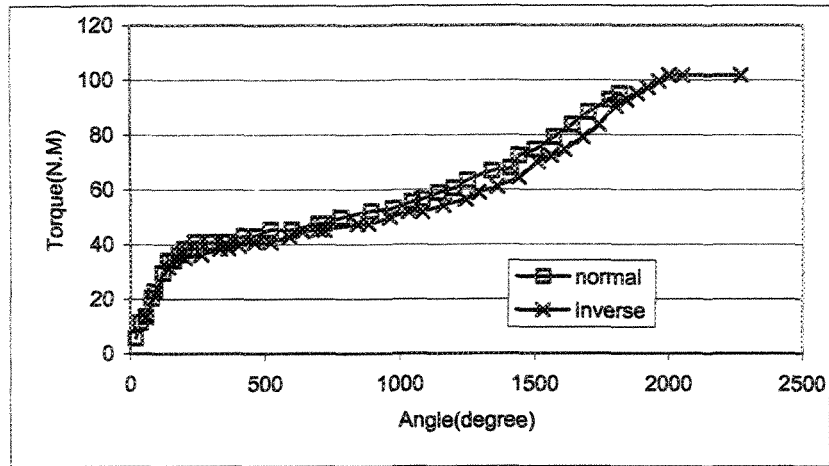


Figure 8.12 Torque-angle curves for wire sample

## 8.5 Conclusions

- The rigidity of a cylinder has a direct influence on the rate of any icing process occurring on its surface. Given two cylinders of similar diameter, the soft one tends to collect more ice deposit while rotating at a relatively higher speed during a particular ice event. It may further be concluded that, in the case of cable icing, a small-sized cable is more likely to undergo a higher icing rate than the larger-sized cable under similar icing conditions, since a small cable is commonly of lesser stiffness while displaying a greater LCE.
- Cable rotation speed is not constant during the period of ice build-up. The cable first experiences an increase in its rotation speed due to a rapid growth in aerodynamic torque occurring at this stage. As the simulation proceeds, the

rotation speed begins to decrease, and gradually the torque from the ice load becomes the main drive for maintaining cable rotation.

- The contribution of aerodynamic torque to the cable-rotation process varies over time under icing conditions. In general, aerodynamic torque exerts a significant influence at an early stage, which diminishes over time, however, as opposed to the influence of gravitational torque.

## CHAPTER 9

### CONCLUSIONS AND RECOMMENDATIONS

A new numerical ice model and code designed specifically for simulating the ice accretion process on transmission line cables has been successfully developed. The research involved in the design of this model is the first attempt of its kind using real-time airflow computation to account for the relationships between the airflow field and its related aspects in the same accretion process. These aspects include the movement of a droplet in the vicinity of an ice-covered cylinder, convective heat transfer in the thermal boundary layer, flow of a water film on the icing surface, and rotation of an ice-covered cable. Although an electric wire was treated as a cylindrical object in the ice model, it is possible, nevertheless, to apply the same model to simulate the icing process on an object of an arbitrary cross-sectional shape, since a cylindrical ice shape is not specifically assumed during the modelling. The validity and reliability of this code has been confirmed by comparing the simulation results to those obtained from experimental measurements. This is further supported by the fact that the simulated ice shape on a flexible wire shows a striking similarity to an ice sample collected during one major ice event which occurred in Québec in 1998.

#### *9.1 Conclusions*

1. Time-dependent field calculations, such as airflow computation and droplet trajectory calculations, have been incorporated into the model described above. It

may be concluded that these efforts are well worth while since the proposed procedure displays a greater capacity for predicting complex ice shapes than the commonly-used procedure based on the Langmuir curve-fitting formulae. The new calculation procedure alone may be applied in the simulation of the icing process on either a cylindrical or an object of arbitrary shape.

2. The Boundary Element Method (BEM) combined with the Finite Volume Method (FVM) was used to compute the free-stream field. It was found that this calculation procedure is easy to implement on a computer, that only moderate calculation time is required, and that calculation results display satisfactory accuracy. However, since a large quantity of finite volume elements are required to store field velocity information, a minimum of 256 MB RAM may be needed to run the proposed ice code.
3. The Runge-Kutta method is an appropriate numerical algorithm chosen for tracking and simulating water droplet trajectories in the vicinity of an ice-covered object since, when using this method, a convergent solution to a set of differential equations may be achieved with a moderate number of time steps.
4. Surface runback water is assumed to exist in the form of a water film in the proposed ice model. This assumption holds true for wet accumulations characterized by abundant unfrozen water on an icing surface. Surface runback water can also exist on the ice surface in the form of drops or rivulets, which tend

to promote elements of surface roughness. By disregarding such a factor, the proposed ice model may predict an overly smooth ice shape.

5. The proposed model may be used to simulate ice accretion processes for both dry and wet accumulations, and the cylindrical object used for model calculations may be either a rigid or flexible cable. It should be noted that icicles may form suspended beneath the iced object when a wet regime is dominant on the icing surface. In such a case, this model may underestimate the ice-load to a high degree due to the neglect of such icicle formation.
6. When compared to its non-energized counterpart, an energized cylinder under icing conditions may present a wetter ice surface, consequently collecting less ice deposit on its surface. However, no apparent change in ice shape is to observed in the same comparison.
7. As the diameter of a cable decreases, the value of the LCE rises correspondingly, as does the maximum impingement angle. It may be further observed that a small cable tends to collect a more substantial ice deposit in terms of its size under the same icing conditions. This implies that a higher icing intensity prevails on a smaller cable during the same ice event.

8. For an ice accretion under semi-wet icing conditions, ice is found to be drier initially while becoming wetter as the icing process advances. Meanwhile, dry ice of low density is observed on each of the upper and lower edges of the ice mass.
9. Ice mass will be found more on the rear surface of a cylindrical object with a increase in the MVD alone. In wet-icing conditions, a heavier ice load will be observed on an icing cylinder when larger-sized droplets are involved.
10. The rigidity of a cylinder has a direct influence on the rate of the icing process occurring on its surface. For two cylinders of similar diameter, the softer one tends to collect more ice deposit while rotating at a relatively higher speed during a particular icing event. It may further be concluded that, in the case of cable icing, a cable of smaller size is more likely to undergo a higher icing rate than the cable of larger size under the same icing conditions, since a small cable is commonly less rigid while at the same time displaying a greater LCE.
11. The cable rotation speed is not constant. The cable first experiences an increase in its rotation speed due to a rapid growth in aerodynamic torque at this stage. With time elapsing, the rotation speed then begins to decrease, and eventually it is the torque from the ice load which maintains cable rotation.
12. Under icing conditions, the contribution of the aerodynamic torque to the cable-rotation process varies with time. In general, the aerodynamic torque exerts a

significant effect at an early stage, although, this effect diminishes over time compared to the gravitational torque.

A 2-D icing model assumes that model parameters such as the LCE, HTC, and so forth, are evenly distributed along the span of a cylindrical object, and thus a uniform ice distribution along this span may be taken for granted. As a result, the cross-sectional cut for the purpose of study may be applied at any position along the span. This assumption, however, fails to take into account such factors as the velocity components of airflow and water flow along the same span, among others. Therefore, extending the proposed ice model to 3-D appears to be of particular significance so as to account adequately for the above-mentioned factors.

## ***9.2 Recommendations for Future Research Directions***

### **9.2.1 Extend the 2-D ice model proposed herein to a 3-D ice model**

A study on a new 3-D model should be assigned priority among all other necessary updating projects, since it may serve to overcome the main drawbacks of a 2-D icing model based on the reasons provided earlier. It is recommended that the 3-D model under consideration be developed on the basis of knowledge acquired thus far, and also that it should be an extension of the present 2-D ice model.

A single icicle comes into being in icing conditions due to the flow of unfrozen water under the combined action of gravity, air drag and water surface tension. Makkonen's icicle model (1995) takes into account gravity and surface tension involved in the process



of icicle formation. Air drag should further be incorporated in the future study so as to obtain a realistic ice-shape prediction. It should be noted that beneath the iced cylinder there is not just a single icicle but a whole icicle curtain. The icicles in the curtain, however, are not evenly distributed, as shown in Figure 9.1. Probability may play a role during the formation of such a distribution, and accordingly, a specific method should be applied in future research in order to take this particular process into account.

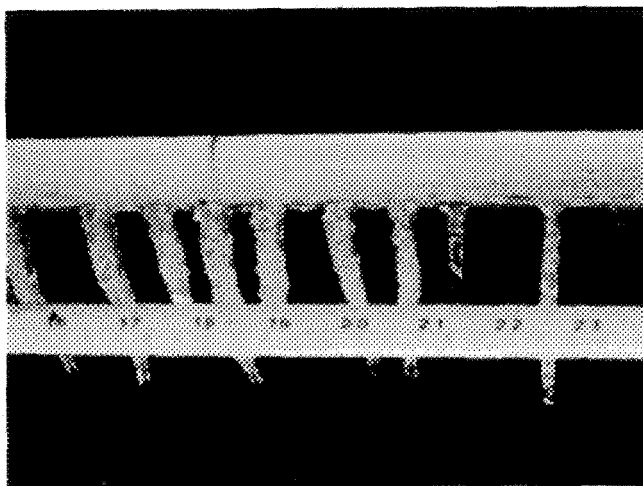


Figure 9.1 Icicle curtain beneath an iced cylinder

In parallel, experiments should be carried out for the purpose of validating the future 3-D ice model. Ice shape together with ice load should be recorded during these tests. In view of the fact that parameters along the span of a test model in the CAIRWT test section are not perfectly uniform, specific considerations are necessary to eliminate the non-uniform effect, enabling the comparison of these data with simulation results.

### **9.2.2 Mechanical Analysis of Iced Cable Using the New Ice Model**

One possible application of an ice model may be its contribution to estimating the overall external load borne by cable lines under icing conditions. The overall load sustained by the supports of cable lines consists of aerodynamic and gravitational forces.

Both forces are known parameters in the new ice model. In order to evaluate the aerodynamic force, it is necessary to solve the 3-D airflow field numerically and thereby obtain the air shear and pressure distribution on the ice surface. Commercial computational software may play an important role in carrying out the field calculations. From the outset, this commercial software must be able to access geometric data produced by model calculations after running icing code. The load thus obtained may serve as a reference for design engineers to determine the ultimate ice load for design purposes.

## REFERENCES

- [1] Achenbach, E., "Heat transfer from smooth and rough surfaced circular cylinders in a cross flow", Proceedings of the 5<sup>th</sup> International Heat Transfer Conference, Tokyo, pp. 229-233, 1974.
- [2] Ackley, S. F. and Templeton, M. K., "Numerical simulation of atmospheric ice accretion ", The 2nd International Symposium on Snow Removal and Ice Control Research, Hanover, N. H., USA, pp. 27 , 1978.
- [3] Bazeos, N. and Beskos, D. E., "Numerical Determination of Wind Pressures on 2-D Structures," Boundary Elements in Mechanical and Electrical Engineering, Computational Mechanics Publications, Springer-Verlag, 1990.
- [4] Best, A.C., "The size distribution of raindrops," Quart. J. Roy. Met. Soc., Vol. 76, pp. 418-428, 1950.
- [5] Bouamoul, A., Farzaneh, M., and G. McClure, "Boundary Element Method Application to Ice Shedding from Overhead Power Line Conductors by Melting Process", The Proceedings of the 10<sup>th</sup> International Workshop on Atmospheric Icing of Structures, IWAIS 2002, BRNO, Czech Republic, June 17-20, 2002, 8-7.
- [6] Bouamoul, A., "Processus de délestage naturel des câbles et conducteurs de transport d'énergie électrique", Ph.D. in Engineering, UQAC, 2002.
- [7] Brebbia, C. A., Telles, J. C. F., and Wrobel, L. C., "Boundary Element Techniques", Springer-Verlag, 1984.
- [8] Bukowska, B. B., and Kreja, I., "Fixed Finite Element Model of Heat Transfer with Phase Change- Part I: Theoretical Formulation and Numerical Algorithm", International Journal of Offshore and Polar Engineering, Vol. 7, No. 2, June 1997.
- [9] Castellano, N. E., Nasello, O. B., and Levi, L., "Study of hail density parameterisations", Proceedings of the 13<sup>th</sup> Int. Conf. on Clouds and

Precipitation, Reno, Nevada, USA, Vol. 2, pp. 1081-1084, August 2000.

- [10] Cebeci, T., and Smith A. M. O., "Analysis of turbulent boundary layers", Academic Press, New York, 1974.
- [11] Chaîné, P. M. and Castonguay, G., "New Approach to Radial Ice Thickness Concept Applied to Bundle-Like Conductors", Industrial Meteorology-Study, Environment Canada, Toronto, pp. 11, 1974.
- [12] Chen, H. C. and Ettema, R., "Atmospheric-ice loading of power transmission cables: laboratory experiments ", Proceedings of the 6<sup>th</sup> International Workshop on Atmospheric Icing of Structures, pp. 12, 1993.
- [13] Chen, Y., Farzaneh, M., Lozowski, E.P., and Szilder, K., "Modeling of Ice Accretion on Transmission Line Conductors", Proceedings of the 9<sup>th</sup> International Workshop on Atmospheric Icing of Structures, Chester, United Kingdom, June 2000, Session 7a.
- [14] Chen, Y., "A 2-D Random Walk Model for Predicting Ice Accretion on a Cylindrical Conductor", Master's Degree Thesis, UQAC, 2001.
- [15] Druez, J., Louchez, S., and McComber, P., "Ice shedding from cables", Cold Regions Science and Technology, Vol. 23, pp. 377-388, 1995.
- [16] Druez, J., McComber, P., and Farzaneh, M., "Atmospheric Icing on a Test Power Line", Transactions of the Canadian Society for Mechanical Engineering, C.S.M.E., Vol. 24, No. 2, pp. 359-374, 2000.
- [17] Duncan, W. J., Thom A. S., and Young. A. D., "Mechanics of Fluids". Edward Arnold Ltd., London, 1970.
- [18] Du N.-D., "Études des méthodes par impact et à l'huile utilisées pour déterminer le diamètre des gouttelettes dans les brouillards naturels et artificiels" , M. Sc. Thesis, Université du Québec à Chicoutimi, Canada, 1987.
- [19] Engene L. Lecomte, Alan W. Pang and James W. Russell, "ICE STORM' 98", Institut for Catastrophic Loss Reduction, Canada, 1998

- [20] Egelhofer, K. Z., Ackley, S. F., and Lynch, D. R., "Computer modeling of atmospheric Ice accretion and aerodynamic loading of transmission lines", *Proceedings of the 2nd International Workshop on Atmospheric Icing of Structures*, pp. 103, 1984.
- [21] FAA Technical Center, "Aircraft Icing handbook," Federal Aviation Administration, Vol. 1 of 3, March 1991.
- [22] FARZANEH, M., "Ice Accretion on H.V. Conductors and Insulators and Related Phenomena," Invited article, *Philosophical Transactions, The Royal Society*, London, No. 358, pp. 1-35, 2000.
- [23] Farzaneh, M., Kiernicki, J., and Drapeau, J.-F., "Ice Accretion on Energized Line Insulators," *International Journal of Offshore and Polar Engineering (IJOPE)*, Vol. 2, No. 3, Sept. 1992.
- [24] Fikiin, K. A., "Generalized numerical modeling of unsteady heat transfer during cooling and freezing using an improved enthalpy method and quasi-one-dimensional formulation", *Int. J. Refrig.* Vol. 19, No. 2, pp. 132-140, 1996.
- [25] Fraser, D., Rush, C. K. and Baxter, D., "Thermodynamic limitations of ice accretion instruments", NRC NAE Laboratory Report LR-32, 1952.
- [26] Fu, P., Bouchard, G., and Farzaneh, M., "Simulation of Ice Accumulation on Transmission Line Cables Based on Time-Dependent Airflow and Water Droplet Trajectory Calculations", *Proceedings of the 23<sup>rd</sup> International Conference on Offshore Mechanics and Arctic Engineering*, Vancouver, Canada, 2004.
- [27] Gates E. M., Lozowski E. P., Finstad K. J., "An approximate method for time-dependent modelling of rime ice accretion", *Proceedings of the 2nd International Workshop on Atmospheric Icing of Structures*, pp 111, 1984.
- [28] Gent, R.W., "TRAJICE2 - A Combined Water Droplet Trajectory and Ice Accretion Prediction Program for Aerofoil," DRA Technical Report TR90054, Nov. 1990.
- [29] Gent, R.W., "Ice Accretion Prediction on Aerofoils," *Proceedings of the First Bombardier International Workshop on Aircraft Icing and Boundary-Layer Stability and Transition*, Montréal, Canada, Sept. 20-21, 1993, pp. 113-138.

- [30] Gerhart P. M., Gross R. J., and Hochstein J. I., "Fundamentals of Fluid Mechanics", Addison-Wesley Publishing Company, 1992.
- [31] Godard, S., " Mesure des gouttelettes de nuage avec un film de collargol", Bulletin de l'Observatoire du Puy de Dome, No.2, 41-45, 1960.
- [32] Goodwin, E. J. et al. "Predicting ice and snow loads for transmission line design", Proceedings of the 1st International Workshop on Atmospheric Icing of Structures, N. H., USA, PP. 267-273, 1983.
- [33] Grenier, J. C., Admirat, P., and Maccagnan, M., "Theoretical Study of the Heat Balance During the Growth of Wet Snow Sleeves on Electrical Conductor", Proceedings of the 3rd International Workshop on Atmospheric Icing of Structures, May 1986.
- [34] Hedde, T., "Modélisation tridimensionnelle des dépôts de givre sur les voilures d'aéronefs," Thèse/doctorat, Université Blaise Pascal, Clermont-Ferrand II, France, No. D.U. 462, Dec. 1992.
- [35] Hedde, T. and Guffond, D., "Improvement of the ONERA 3D Icing Code, Comparison with 3D Experimental Shapes," AIAA Paper 93-0169, 1993.
- [36] Hedde, T. and Guffond, D., "ONERA Three-Dimensional Icing Model", AIAA Journal, Vol. 33, No. 6, June 1995.
- [37] Hess, J.L., and Smith, A.M.O., "Calculation of Potential Flow About Arbitrary Bodies," Progress in Aeronautics Sciences, Vol. 8, pp. 1-138, 1967.
- [38] Hess, J.L., Review of integral-equation techniques for solving potential flow problems with emphasis on the surface-source method, Computer Methods in Applied Mechanics and Engineering, 5, 145, 1975.
- [39] Ide, R. F., "Liquid water content and droplet size calibration of the NASA LEWIS Icing Research Tunnel", NASA, USA, TM-102447, 1990.
- [40] Imai, I., "Studies on Ice Accretion", Research on Snow and Ice, No. 1, pp. 34-44, 1953.

- [41] Jones, K. F., "A Simple Model for Freezing Rain Ice Loads", Proceedings of the 7th International Workshop on Atmospheric Icing of Structures, Chicoutimi, QC, Canada, pp. 412-416, 1996
- [42] Jones, K. F., "The Density of natural ice accretions", Fourth international conference on atmospheric icing of Structures, E. D. F., Volume 77, #1, pp. 114-118, Paris, September 1988.
- [43] Karev, A. R. and Farzaneh, M., "Evolution of Droplet Size Distribution in an Icing Wind Tunnel", Proceedings of the 10th International Workshop on Atmospheric Icing of Structures, BRNO, Czech Republic, 2002.
- [44] Karev, A.R., Farzaneh, M., and Mousavi, M., "Influence of non-uniformity of droplet size distribution on an ice accretion ", Proceedings of the 10th International Workshop on Atmospheric Icing of Structures, BRNO, Czech Republic, 2002.
- [45] Karev, A.R., Farzaneh, M., Kollar, L. & Vaslon, S., "Freezing Water in an Open Channel Flow with a Constant Bottom Temperature under Supercooled Ambient Conditions ", 17<sup>th</sup> Annual Symposium on Ice, St. Petersburg, Russia, june 2004, pp. 379-384
- [46] Kays, W. M., and Crawford, M. E., "Convective Heat and Mass Transfer". McGraw-Hill, pp. 601, 1993.
- [47] Kuroiwa, D., "Icing and Snow Accretion on Electric Wires", U. S. Army Materiel Command, January 1965.
- [48] Langmuir, I. P. and Blodgett, K. B., "Mathematical Investigation of Water Droplet Trajectories", Program Press 196, Vol. 10, Report No. RL-224, 1945.
- [49] Langmuir, I. P. and Blodgett, K. B., " A mathematical investigation of water drop trajectories", AAF Technical Report No. 5418, pp. 47 , 1946.
- [50] Larouche, E., Bouchard, G., Rouat, J., and Farzaneh, M., "Exploration of Standard and Time Dependent Neural Network Techniques for the Prediction of Ice Accretion on Overhead Line Conductors", Proceedings of the 9<sup>th</sup> International Workshop on Atmospheric Icing of Structures, Chester, United

Kingdom, June 2000, Session 2.

- [51] Lesnic, D., Elliott, L. & Ingham, D.B., "Effect of sharp corners on Potential fluid flows past blunt bodies", BE Applications in Fluid Mechanics, 1-29, 1995.
- [52] List, R., 1963: General heat and mass exchange of spherical hailstones. *J. Atmos. Sci.* 20, 189-197.
- [53] List, R., "Ice Accretion on Structures", *J. Glaciol.*, 19, 451-465, 1977.
- [54] Llinca, A., Llinca, F., and Ignat, L., "Numerical Study of Iced Conductors Aerodynamics", Proceedings of the 7th International Workshop on Atmospheric Icing of Structures. 3-7 June, 1996.
- [55] Lock, G. S. H. "The growth and decay of ice", Cambridge University Press, New York, 1990.
- [56] Lozowski, E. P. et al. , "The icing of an unheated, non-rotating cylinder in liquid Water droplet-ice crystal clouds", National Research Council of Canada Report LTR-LT-96, 61 pp., 1979.
- [57] Lozowski, E. P., Stallabrass, J. R., and Hearty, P. F., "The Icing of an Unheated, Non-rotating Cylinder, Part I: A Simulation Model", *Journal of Climate and Applied Meteorology*, Vol. 22, pp. 2053-2062, 1983.
- [58] Ludlam, F. H., "The heat economy of a rimed cylinder", *Q. Jl R. Met. Soc.* 77, 663-666, 1951.
- [59] Macklin W.C., "The density and structure of ice formed by accretion," *Quarterly Journal of the Royal Meteorological Society*, pp. 30-50, 1962.
- [60] Macklin, W.C, and Payne, G. S., " A theoretical study of the ice accretion process ", *Quarterly Journal of the Royal Meteorological Society*, pp. 195-213, 1967.
- [61] Makkonen, L., Stallabrass, J. R., "ICE ACCRETION ON CYLINDERS AND WIRES," National Research Council of Canada, Low Temperature Laboratory,



Report TR-LT-005, 1984.

- [62] Makkonen, L., "Modelling of Ice Accretion on Wires," *Journal of Climate and Applied Meteorology*, Vol. 23, No. 6, pp. 929-939, 1984.
- [63] Makkonen, L., "Heat transfer and icing of a rough cylinder", *Cold Regions Science and Technology*, Vol. 10, pp. 105-116, 1984.
- [64] Makkonen L., "Atmospheric Accretion of Ice Loads", Department of Meteorology University of Helsinki, Report No. 25, 1985.
- [65] Makkonen, L., "The effect of conductor diameter on ice load as determined by a numerical model," *Proceedings of the 3<sup>rd</sup> International Workshop on Atmospheric Icing of Structures*, pp. 81-89, 1986.
- [66] Makkonen, L., and Fujii, Y., "Spacing of icicles", *Cold Regions Sciences and Technology*, Vol. 21, pp. 317-322, 1993.
- [67] Makkonen, L., "Modelling Power Line Icing in Freezing Precipitation", *Proceedings of the 7th International Workshop on Atmospheric Icing of Structures*, Chicoutimi, QC, pp. 195-200, 1996.
- [68] Makkonen, L., "Models for the growth of rime, glaze, icicles and wet snow on structures", *Philosophical transactions: mathematical, physical & engineering sciences*, 2000.
- [69] McComber, P. and Touzot, G., "Calculation of the Impingement of Cloud Droplets in a Cylinder by the Finite-Element Method", *Journal of the Atmospheric Sciences*, Vol. 38, May 1981.
- [70] McComber, P., "Numerical Simulation of Cable Twisting Due to Icing", *Cold Regions Science and Technology*, pp. 253-259, 1984.
- [71] McComber, P. and Bouchard, G., "The Numerical Calculation of the Wind Force Coefficients on Two Dimensional Iced Structures", *Proceedings of the 3rd International Workshop on Atmospheric Icing of Structures*, May 1986.

- [72] Mousavi, M., "Experimental and Theoretical Verification of Two Icing Codes", Master's Degree thesis, UQAC, 2003.
- [73] Messinger, B. L., "Equilibrium temperature of an unheated icing surface as a function of airspeed", *Journal of the Aeronautical Sciences*, Vol. 20, pp. 195-200, 1953.
- [74] Mulherin, N. D., "Atmospheric Icing and Tower Collapse in the United States", *Proceedings of the 7<sup>th</sup> International Workshop on Atmospheric Icing of Structures*, June 1996.
- [75] Paraschivoiu, I., Tran, P., and Brahimi, M.T., "Prediction of Ice Accretion with Viscous Effects on Aircraft Wings," *AIAA Journal of Aircraft*, Vol. 31, No. 4, pp. 855-861, July-Aug. 1994, (also AIAA Paper 93-0027).
- [76] Paraschivoiu, I., Gouttebroze, S., and Saeed, F., "CANICE—Capabilities and Current Status," *NATO/RTO Workshop, Assessment of Icing Code Prediction Capabilities*, at CIRA in Capua, Italy, Dec. 6–7, 2000.
- [77] Pellet, J. L. and Dennis A. S., "Effects of heat storage in hailstones", *Preprints of the Conference on Cloud Physics*, Tucson, pp. 63-66, 1974.
- [78] Personne, P. and Gayet J.-F., "Ice Accretion on Wires and Anti-Icing Induced by Joule Effect", *Journal of Applied Meteorology*, V.27, pp.101-115, 1988.
- [79] Poots, G., "Ice and Snow Accretion on Structures," *Research Studies Press LTD*, 1996.
- [80] Porcu, F., Smargiassi, E., and Prodi, F., "2D and 3D Modelling of Ice Accretion on Wires", *Proceedings of the 6<sup>th</sup> International Workshop on Atmospheric Icing of Structures*, PP: 53-55, 1993.
- [81] Rae, W. H. and Pope, A., "Low-speed tunnel testing", *J. Wiley and Sons*, 2<sup>nd</sup> edition, New York, N.Y., USA, pp. 534, 1984.
- [82] Rudzinski, W.J., Lozowski, E. P., and Farzaneh, M., "2-D Numerical Modeling of the Icing of a Non-Energized Station Post Insulator Under Freezing Rain Conditions", *Proceedings of the 10<sup>th</sup> International Workshop on Atmospheric*

Icing of Structures, IW AIS 2002, BRNO, Czech Republic, June 17-20, 2002, 6-2.

- [83] Savadjiev, K., and Farzaneh, M., " Study of icing and related meteorological parameter distributions during atmosphere icing events ", Proceedings of the 11th International and Polar Engineering Conference, Stavanger, Norway, Vol. 1, pp. 52-54, 2001.
- [84] Semyonov Yu, V., and Smoroding, A. Z., "Characteristic Features of Convective Heat Transfer at a Liquid-Solid Body Phase Interface", Journal of Engineering Physics and Thermophysics, Vol. 64, No. 5, 1993.
- [85] Skelton, P. L. I., and Poots, G., "Approximate predictions of ice accretion on an overhead transmission line which rotates with constant angular velocity". IMA Journal of Applied Mathematics, Vol. 40, pp. 23-45, 1998.
- [86] Stallabrass, J. R., "An appraisal of the single rotating cylinder method of liquid water content measurement", National Research Council of Canada, Division of Mechanical Engineering, Report LTR-LT-92, Nov., 1978.
- [87] Szilder, K., Lozowski, E. P., and Gates, E. M., "Modelling Ice Accretion on Non-Rotating Cylinders –The Incorporation of Time Dependence and Internal Heat Conduction ", Cold Regions Science and Technology, Vol. 13, pp. 177-191, 1987.
- [88] Szilder, K., Lozowski, E. P., and Gates, E. M., "Some Applications of a New Time-Dependent Cylinder Ice Accretion Model", Atmospheric Research, V.22, pp. 41-59, 1988.
- [89] Szilder, K., and Lozowski, E. P., "Simulation of Icicle Growth Using a Three-Dimensional Random Walk Model," Atmospheric Research, Vol. 36, No. 1, pp. 243-249, 1995.
- [90] Szilder, K., and Lozowski, E. P., "Three-Dimensional Modelling of Ice Accretion Micro Structure", Proceedings of the 7<sup>th</sup> International Workshop on Atmospheric Icing of Structures, June 1996.
- [91] Szilder, K., and Lozowski, EP., "Morphogenetic Modelling of Wet Ice Accretions on Transmission Lines as a Result of Freezing Rain", Proceedings of the 11th International and Polar Engineering Conference, ISOPE, Brest, Vol. 2,

pp. 616-621, 1999.

- [92] Szilder, K., Farzaneh, M., and Lozowski, EP., "Analysis of Water Film Flow on an Icing Surface", Proceedings of the 9<sup>th</sup> International Workshop on Atmospheric Icing of Structures, Chester, United Kingdom, June 2000, session 4b.
- [93] Szilder, K., Lozowski, EP., and Farzaneh, M., "Morphogenetic Modeling of Wet Ice Accretions on Transmission Lines as a Result of Freezing Rain", International Journal of Offshore and Polar Engineering, Vol. 11, No. 1, pp. 16-22, March 2001.
- [94] Taylor, G.I., "Notes on Possible Equipment and Technique for Experiments on Icing on Aircraft," British Aeronautical Research Council, R&G, No. 2024, Jan. 1940.
- [95] Thwaites, B., "Approximate Calculation of the Laminar Boundary Layer," Aeronautical Quarterly, 1, 1949.
- [96] Vick, D. and Nelson, D. J., "The Boundary Element Method Applied to Freezing and Melting Problems," Numerical Heat Transfer, part B, Vol. 24, pp. 263-277, 1993.
- [97] Wright, W.B., "Advancement in the LEWICE Ice Accretion Model," AIAA Paper 93-0171, 1993.
- [98] Zukauskas, A., "Heat Transfer from tubes in cross-flow", Advances in Heat Transfer, Vol. 8, pp. 93-160, 1972.

## Appendix: Runge-Kutta Algorithm

The Runge-Kutta algorithm makes it possible to solve a differential equation numerically (i.e. approximately). Consider the single variable problem

$$x' = f(t, x)$$

with initial condition  $x(0)=x_0$ . Suppose that  $x_n$  is the value of the variable at time  $t_n$ . The Runge-Kutta formula takes  $x_n$  and  $t_n$  and calculates an approximation for  $x_n$  at a brief time later,  $t_n+h$ . It uses a weighted average of approximated values of  $f(t, x)$  at several time points within the interval  $(t_n, t_n+h)$ . The formula is given by

$$x_{n+1} = x_n + (h/6)(k_1 + 2k_2 + 2k_3 + k_4)$$

where

$$k_1 = f(t_n, x_n)$$

$$k_2 = f(t_n + h/2, x_n + (h/2)k_1)$$

$$k_3 = f(t_n + h/2, x_n + (h/2)k_2)$$

$$k_4 = f(t_n + h, x_n + h k_3)$$

To run the simulation, we simply start with  $x_0$  and find  $x_1$  using the formula above. Then we plug in  $x_1$  to find  $x_2$  and so on.

The Runge-Kutta algorithm is known to be very accurate and fulfills the requirements for a wide range of problems. For further information on why this is such a satisfactory method, or where it can be expected to fail, consult pertinent references in the field.

## Two-variable Runge-Kutta Algorithm

The Runge-Kutta algorithm can be easily extended to a set of first order differential equations. One winds up with essentially the same formulas as shown above, but all the variables are vectors except for time.

To give an idea of how it works, here is an example where the vector notation is expanded. That is, instead of using the highly compact vector notation, one writes out all the components of the vector.

Suppose there are only two variables,  $x, y$  and two differential equations

$$x' = f(t, x, y)$$

$$y' = g(t, x, y)$$

Again we let  $x_n$  be the value of  $x$  at time  $t_n$ , and similarly for  $y_n$ . Then the formulae for the Runge-Kutta algorithm are

$$x_{n+1} = x_n + (h/6)(k_1 + 2k_2 + 2k_3 + k_4)$$

$$y_{n+1} = y_n + (h/6)(j_1 + 2j_2 + 2j_3 + j_4)$$

where

$$k_1 = f(t_n, x_n, y_n)$$

$$j_1 = g(t_n, x_n, y_n)$$

$$k_2 = f(t_n + h/2, x_n + (h/2)k_1, y_n + (h/2)j_1)$$

$$j_2 = g(t_n + h/2, x_n + (h/2)k_1, y_n + (h/2)j_1)$$

$$k_3 = f(t_n + h/2, x_n + (h/2)k_2, y_n + (h/2)j_2)$$

$$j_3 = g(t_n + h/2, x_n + (h/2)k_2, y_n + (h/2)j_2)$$

$$k_4 = f(t_n + h, x_n + h k_3, y_n + h j_3)$$

$$j_4 = g(t_n + h, x_n + h k_3, y_n + h j_3)$$

Given starting values  $x_0, y_0$  we can plug them into the formula to find  $x_1, y_1$ . Then we can plug in  $x_1, y_1$  to find  $x_2, y_2$  and so on.

### **Multi-variable Runge-Kutta Algorithm...**

Suppose we have more than two variables which are  $x, y, z, \dots$ . We then need to convert the differential equations into a system of first order equations, as follows:

$$x' = f(t, x, y, z, \dots)$$

$$y' = g(t, x, y, z, \dots)$$

$$z' = h(t, x, y, z, \dots)$$